



UNIVERSIDAD NACIONAL AUTÓNOMA DE MÉXICO
POSGRADO EN CIENCIAS FÍSICAS
INSTITUTO DE CIENCIAS NUCLEARES

Monte Carlo and reconstruction analysis of baryon and meson production in heavy-ion collisions at MPD-NICA

Tesis

Que para optar por el grado de:
Maestro en Ciencias (Física)

Presenta:

Rodrigo Guzmán Castro

Tutores principales

Eleazar Cuautle Flores
Instituto de Ciencias Nucleares, UNAM
Wolfgang Peter Bietenholz
Instituto de Ciencias Nucleares, UNAM

Miembros del comité tutor

Jaime Besprosvany Fridzon
Instituto de Física, UNAM
Roelof Bijker
Instituto de Ciencias Nucleares, UNAM

Ciudad de México, Junio, 2024



Universidad Nacional
Autónoma de México

Dirección General de Bibliotecas de la UNAM

Biblioteca Central



UNAM – Dirección General de Bibliotecas
Tesis Digitales
Restricciones de uso

DERECHOS RESERVADOS ©
PROHIBIDA SU REPRODUCCIÓN TOTAL O PARCIAL

Todo el material contenido en esta tesis esta protegido por la Ley Federal del Derecho de Autor (LFDA) de los Estados Unidos Mexicanos (México).

El uso de imágenes, fragmentos de videos, y demás material que sea objeto de protección de los derechos de autor, será exclusivamente para fines educativos e informativos y deberá citar la fuente donde la obtuvo mencionando el autor o autores. Cualquier uso distinto como el lucro, reproducción, edición o modificación, será perseguido y sancionado por el respectivo titular de los Derechos de Autor.

Agradecimientos

Este trabajo ha sido posible gracias a la contribución y apoyo de un considerable número de personas, quienes han formado parte de mi vida en mayor o menor medida, pero sin quienes no habría logrado llegar hasta aquí.

Quisiera expresar primeramente mi agradecimiento a mi madre *Maria Elena*, cuyo amor y apoyo incondicional siempre me ha permitido seguir adelante, por haberme enseñado perseverancia y dedicación, sin duda gran parte de mis mejores cualidades son gracias a ella. A mis hermanos, *Jacqueline* y *Daniel*, creo que con el tiempo nos hemos conocido cada vez menos de lo que nos gustaría admitir, pero siempre me han brindado apoyo, de una u otra forma. Al resto de mi familia, a quienes siempre que los veo, me brindan su cariño y una cálida sonrisa.

Al Dr. *Eleazar Cuautle*, por su guía, sus enseñanzas y las largas charlas en general, este trabajo habría sido imposible de no ser por su apoyo, tanto intelectual como humano. Al Dr. *Wolfgang Bietenholz*, también por sus enseñanzas, las charlas y sobre todo las correcciones, mi trabajo no tendría algo de fluidéz y elocuencia de no ser por sus comentarios. Al Dr. *Alejandro Ayala*, con quien también tuve el placer de trabajar y aprender durante la realización de este trabajo, sus comentarios me han sido de mucha ayuda. Al Dr. *Ángel Sánchez*, quien amablemente me brindó comentarios y ayuda para preparar mi defensa. Al Dr. *Genaro Toledo* y al Dr. *Mario Rodríguez*, cuyas observaciones me han permitido mejorar mi trabajo. A los miembros de mi comité tutor: el Dr. *Jaime Besprosvany* y el Dr. *Roelof Bijker*, por dar seguimiento y apoyo a lo largo de mi paso por el posgrado.

A mis amigos más veteranos: *Gustavo*, *Enrique*, *Aaron* y *Luis*, por la incontable cantidad de anécdotas que hemos compartido. Contar con su amistad me ha llenado de momentos (sobre todo, pero no exclusivamente) divertidos. No olviden llevar una toalla.

También agradezco a mis amigos de la facultad, a todos “los del prome”. Particularmente a *Jovany*, *memo*, *luisin*, *paco* y *lalo*, a quienes ya no tuve el placer de tener de compañeros en el posgrado, pero siempre me continuaron apoyando y dándome ánimos.

A mis amigos del museo, especialmente a *Montse*, por siempre estar ahí para escucharme y alegrarse por mí, yo sé que nunca me libraré de su apoyo. También a *Ximena*, por las largas e interesantes charlas intelectuales, siempre me inspiran y enseñan bastante.

Al JINR y su programa START, así como todas las personas involucradas en el mismo. La oportunidad de colaborar y pasar unos meses en Rusia fue una de las experiencias intelectuales y culturales más enriquecedoras de mi vida. A todas las extraordinarias y brillantes personas que conocí durante mi estancia, en particular a la Dra. *Ivonne Maldonado*, de quien aprendí muchísimo durante mi estancia, y quien continúa brindándome su apoyo y enseñanzas.

Por último, a la *Universidad Nacional Autónoma de México*, al programa de posgrado en ciencias (física) y al *Instituto de Ciencias Nucleares*, así como a todo el personal administrativo y docente, los cuales siempre están ahí para brindar ayuda, y sin quienes no sería posible mantener la excelencia educativa y competencia a nivel internacional. Así mismo, agradezco al CONAHCYT y DGAPA, particularmente los programas PAPIIT-IG100322 y CONAHCYT A1-S16215, por el apoyo económico que me han brindado durante mis estudios.

Me es imposible agradecer a todos y cada uno de manera explícita y personal, me disculpo si alguien se ha sentido excluído, no fue mi intención. De cualquier manera, hayan sido nombrados o no, espero poder devolver un poco a sus vidas de lo que han brindado a la mía, ¡gracias!.

Contents

1	Introduction	11
1.1	Heavy-ion collisions	11
1.2	QCD phase diagram	13
1.3	Prospects of this work	16
2	Nuclotron-based Ion Collider fAcility	21
2.1	Injection complex	21
2.2	Booster, Nuclotron and Collider	23
2.3	BM@N and SPD detectors	25
2.4	The Multi-Purpose Detector (MPD)	29
2.4.1	MPD Collaboration and MexNICA	29
2.4.2	Detector layout configuration	29
3	Event generators	32
3.1	UrQMD event generator	33
3.2	PHSD event generator	35
4	Monte Carlo and reconstructed data	38
4.1	Monte Carlo data sample (from UrQMD)	38
4.2	Monte Carlo data sample (from PHSD)	40
4.3	Transport process	41
4.4	Kinematic relativistic in heavy-ions	42
4.5	Event selection	42
4.6	Track selection	44
4.7	Tracks efficiency and contamination	45
4.7.1	Repeated tracks	46
4.7.2	Primary and secondary tracks	47
4.8	Particle identification	48
4.9	Identification efficiency and contamination	53
5	Results and discussion of the Monte Carlo data	56
5.1	Event and track selection analysis	56
5.2	Transverse momentum distributions	63
5.3	Uncorrected reconstructed distributions	68
5.4	Bi+Bi collisions at 9.2 GeV	71
5.5	Particle integrated ratios	73

5.6	Crossing point	78
5.7	Future development	81
6	Conclusions	83

Resumen

En este trabajo, se realizó un estudio sistemático de colisiones de iones pesados relativistas a nivel simulación Monte Carlo, en especial, colisiones de Au+Au a energías en el rango del experimento MPD-NICA: $\sqrt{s_{NN}} = 4.5, 7.7, 9.2$ y 11.5 GeV. El estudio también fue realizado para colisiones de Bi+Bi a $\sqrt{s_{NN}} = 9.2$ GeV. Además, se realizaron simulaciones del paso de las partículas a través del detector MPD. La intención es que dichos resultados puedan ser considerados como referencia para los primeros datos experimentales que producirá el MPD en 2025.

A nivel Monte Carlo se estudiaron tres modelos: HSD, PHSD y UrQMD, con los cuales se simularon los mecanismos de producción de mesones y bariones en colisiones de iones pesados. En especial, se obtuvieron las distribuciones de momento transversal de π^\pm , K^\pm y p^\pm , con lo cual se calcularon las razones K^\pm/π^\pm como función de la energía de colisión y compararon con datos experimentales, observándose un desacuerdo en general. En dichos datos experimentales, se ha observado que la razón K^+/π^+ crece con la energía de la colisión, alcanzando un máximo alrededor de 8.2 GeV, y al continuar incrementando dicha energía, decrece. El resultado es de interés, puesto que inicialmente este comportamiento fue propuesto como una de las posibles señales de la existencia del plasma de quarks y gluones. También, al estudiar los mecanismos que producen kaones y piones en cada modelo, podemos entender mejor (hasta cierto punto) los aciertos y fallas de cada modelo.

Con los datos simulados, se identificaron los valores de momento para los cuales ocurre una transición de dominancia de producción de bariones a mesones. Esto podría explicar el comportamiento de la razón K^+/π^+ de manera estadística, pero no parece dar cuenta de los resultados obtenidos con los modelos utilizados. Las razones partícula-antipartícula y la producción de hiperones como Λ^0 y Σ^0 también se calcularon y compararon con datos experimentales. Estas presentan un buen acuerdo para el caso de los piones, pero un desacuerdo para el resto. En general, estos resultados mostraron que los modelos de producción de hadrones empleados predicen razonablemente las propiedades cualitativas observadas en los experimentos tales como AGS, STAR, etc., pero requieren mejoras para dar una descripción más cercana.

Por otro lado, se realizó un estudio con el software del experimento MPD-NICA. Aspectos como el algoritmo de reconstrucción de trazas, así como la eficiencia en la reconstrucción e identificación de partículas se estudiaron con cierto detalle. La finalidad es lograr mejor calidad de trazas reconstruidas y consecuentemente una mejor identificación de partículas.

Una vez entendidas y calculadas las eficiencias para cada especie de partícula, se obtuvo una primera estimación de las distribuciones de momento transversal de mesones y bariones. Se construyeron diferentes ecuaciones paramétricas (como función de la energía de colisión), las cuales predicen el valor del momento en el cual las distribuciones de piones y protones

se cruzan unas a otras. Los resultados indican que, aunque los modelos parten de un marco microscópico de transporte, parecen seguir un comportamiento global sistemático, el cual indica una zona de transición de mayor producción de bariones a mesones dentro del rango del MPD. Si bien estos resultados pueden mejorarse con una mayor estadística, también se espera un mejor algoritmo de reconstrucción y eficiencias más precisas en futuras versiones del software empleado.

Los temas abordados aquí tienen relevancia, tanto teórica como experimental, debido a que estos pueden contribuir a un mejor entendimiento de una porción del diagrama de fase de la Cromodinámica Cuántica, objetivo principal del experimento MPD.

En el Capítulo 1 se explican brevemente los conceptos relacionados con la física de colisiones de iones pesados relativistas. Además se revisa con cierto detalle la estructura del diagrama de fase. Todo esto es complementado con los resultados experimentales que nos han llevado a dichas conclusiones, así como los modelos teóricos que las acompañan. Por último, se discuten las motivaciones del trabajo, así como lo que se espera obtener del mismo.

El Capítulo 2 está dedicado a describir el complejo NICA, en el cual se encuentra actualmente en construcción el MPD. Se da un bosquejo general del proyecto NICA, las metas y limitaciones de cada uno de los detectores en construcción, con un especial énfasis en el MPD.

Respecto al Capítulo 3, se discuten los modelos empleados para llevar a cabo las simulaciones de las colisiones. Se da un panorama general de como es que el problema, desde el punto de vista teórico, es abordado.

El Capítulo 4 trata sobre todo lo relacionado con las simulaciones, reconstrucción e identificación, desde un punto de vista un tanto más técnico. En primer lugar, se establecen las condiciones en que las muestras de datos fueron generados y de qué consisten. Después se discute brevemente el proceso de transporte, que simula la interacción de las partículas producidas en la colisión con los materiales del detector. A continuación se discute la selección de eventos y trazas, los cuales sirven para optimizar la calidad de los datos obtenidos, reducir la contaminación, etc. Finalmente se discute el proceso de identificación de partículas, así como la eficiencia de este proceso.

Por último, en el Capítulo 5 se presentan los resultados del trabajo. Esto incluye el análisis sobre la selección de eventos en todas las distribuciones de momento transversal, tanto a nivel simulación como a nivel reconstrucción. Se hace hincapié en los resultados obtenidos a partir de las simulaciones realizadas por la colaboración MPD. Esto es debido a que cuando el MPD sea puesto en funcionamiento (en 2025), los primeros resultados experimentales contarán con las características que se han impuesto a dichas simulaciones. A partir de las distribuciones obtenidas, se calculan las razones de partículas, las cuales son comparadas con los datos experimentales. Finalmente, se estudia la producción de mesones y bariones, pues está ligada al máximo observado en la razón K^+/π^+ .

Abstract

In this work, a systematic study of heavy-ion collisions was carried out at the Monte Carlo simulation level, particularly for Au+Au collisions at MPD-NICA energies: $\sqrt{s_{NN}} = 4.5, 7.7, 9.2$ and 11.5 GeV. The study was also implemented for Bi+Bi collisions at $\sqrt{s_{NN}} = 9.2$ GeV. In addition, simulations of the transport of particles through the MPD detector were carried out. The intention is that these results can be considered as a reference for the first experimental data that the MPD will produce in 2025.

At the Monte Carlo level, three models were studied: HSD, PHSD and UrQMD, with which different production mechanisms of mesons and baryons in a collision process were simulated. In particular, the transverse momentum distributions of π^\pm , K^\pm and p^\pm were obtained, from which the particle ratios K^\pm/π^\pm were calculated as a function of collision energy and compared to experimental data, showing a general discrepancy. From these experimental data, it has been observed that the K^+/π^+ ratio increases its value with the collision energy, reaching a maximum at around 8.2 GeV, and as the energy further increases, the ratio decreases. This is of particular interest for heavy-ion physics, because this behavior was proposed as one of the signatures for the existence of the quark-gluon plasma. Also, by studying the production mechanisms involved in the production of kaons and pions in each model, we can better understand (to some extent) the successes and failures of each model.

With the simulated data, we can identify the momentum values for which a transition of a baryon- to a meson-dominance of particle production occurs. This might explain the K^+/π^+ behaviour in a statistical manner, but does not account for the results obtained with the current employed models. The particle-to-antiparticle ratios and the production of hyperons such as Λ^0 and Σ^0 were also calculated and compared with experimental data. They present a good agreement for the pions case, but a discrepancy for the rest. Generally speaking, these results showed that these hadron production models employed can predict reasonably well the qualitative properties observed in experimental data of facilities such as AGS, STAR, etc., but some improvements are required to give a closer description.

On the other hand, a study within the MPD-NICA software was realized. Aspects such as the analysis of the reconstruction algorithm for the tracks, as well as the reconstruction and identification efficiency were studied in some detail. The purpose was to achieve better quality of reconstructed tracks, and consequently an improved particle identification.

Once the efficiency was understood and calculated for each particle species, a first estimate of the transverse momentum distributions of mesons and baryons was obtained. Different parametric equations (as a function of the collision energy) were constructed to predict the momentum values where the pion and proton distributions cross each other. These results show that, even though the approach of the models is of a microscopical nature, they seem to follow a global systematic behaviour, indicating the existence of a region where a transition

from a baryon- to a -meson-dominance is taking place within the MPD range. The results can be improved with more statistics, but also better reconstruction algorithms and improved efficiencies are expected in future versions of the software.

The topics addressed in this work are relevant both theoretically and experimentally, because they can contribute to a better understanding of a portion of the Quantum Chromodynamics phase diagram, which is the main objective of the MPD experiment.

Chapter 1

Introduction

It is hard to specify just one particular moment in modern history which could be considered as the birth of the field of particle physics. But undoubtedly the discovery of the atoms and smaller structures has paved the ground for even more striking discoveries and theories over the last ~ 120 years.

Another crucial event was the invention of the cyclotron by Lawrence and Livingston in 1932 [1]. The idea was to accelerate charged particles, embedded inside a constant magnetic field, with a rapidly changing electric field, and thus producing a spiral path of accelerated particles. This very basic concept is essentially how most of the modern accelerators all around the world work, from the very first 11 cm radius cyclotron to the enormous ~ 4243 m radius Large Hadron Collider.

There were many contributions that have led us to current particle physics experiments. The field is quite broad, but we will focus on the particular subject of heavy-ion collisions, which is not entirely within the particle physics realm but includes aspects of nuclear physics as well. As the name implies, the idea is quite straightforward, it consists of producing ion (atomic nuclei) collisions at relativistic energies. Energies are considered relativistic if the kinetic energy is much larger than the rest energy. Typically this takes about 10 GeV/n (per nucleon, i.e. proton or neutron).

In this chapter, a brief summary on heavy-ion collision theory is presented. Also, some of the experimental results and predictions of lattice QCD which have drove part of the collective imaginary of physicists over the last few decades, whose primary goal is to unravel the structure of the so called QCD phase diagram.

1.1 Heavy-ion collisions

The experimental origins of the heavy-ion collision experiments can be traced back to 1986. In that year two experiments were commissioned: the Alternating Gradient Synchrotron (AGS) at the Brookhaven National Laboratory (BNL) and the Super Proton Synchrotron (SPS) at CERN (in French “Conseil Européen pour la Recherche Nucléaire”). Their energies ranged from 14 (AGS) up to 200 (SPS) GeV/n. Subsequently, the focus was devoted to achieving higher energies, which in turn means larger accelerator complexes. Although that is a very interesting and thriving subject, the interest for this work is more in the relatively low energy region (and high baryonic density region, this will be explained later on this chapter). Several

experiments have been investigating this energy range, namely: the Relativistic Heavy Ion Collider (RHIC) at BNL, the already discussed AGS and SPS. But the full coverage of this energy range, at which high baryonic densities are reached is, so far, mostly unknown. Future experiments such as the Compressed Baryonic Matter (CBM) at the Facility for Antiproton and Ion Research (FAIR) and the Multi-Purpose Detector (MPD) at the Nuclotron-based Ion Collider fAcility (NICA) are expected to be commissioned in 2025. The final goal is to complement the data of the already existing facilities in the high baryonic density region, and thus attain a broader picture of this region. But, why is this region so interesting?

Even if the collision process could be theoretically described by Quantum Chromo Dynamics' (QCD) first principles, in practice, analytic calculations become an impossible task. Pure QCD can be applied to study some subprocesses, but more suitable theoretical tools are needed to describe heavy-ion collisions. Different models describe different stages of the collision process, which are based in thermal field theory, relativistic transport theory, relativistic fluid dynamics, etc. Much more extensive and complete reviews can be found in Refs. [2–4]. Figure 1.1 shows schematically the most important stages occurring in a heavy-ion collision process. The effective picture of the whole process is very much model-dependent, but the idea in this section is to give a general picture of the space-time evolution. In the third chapter, the models studied in this work are introduced. Therefore, this section and the third chapter should be considered as complementary.

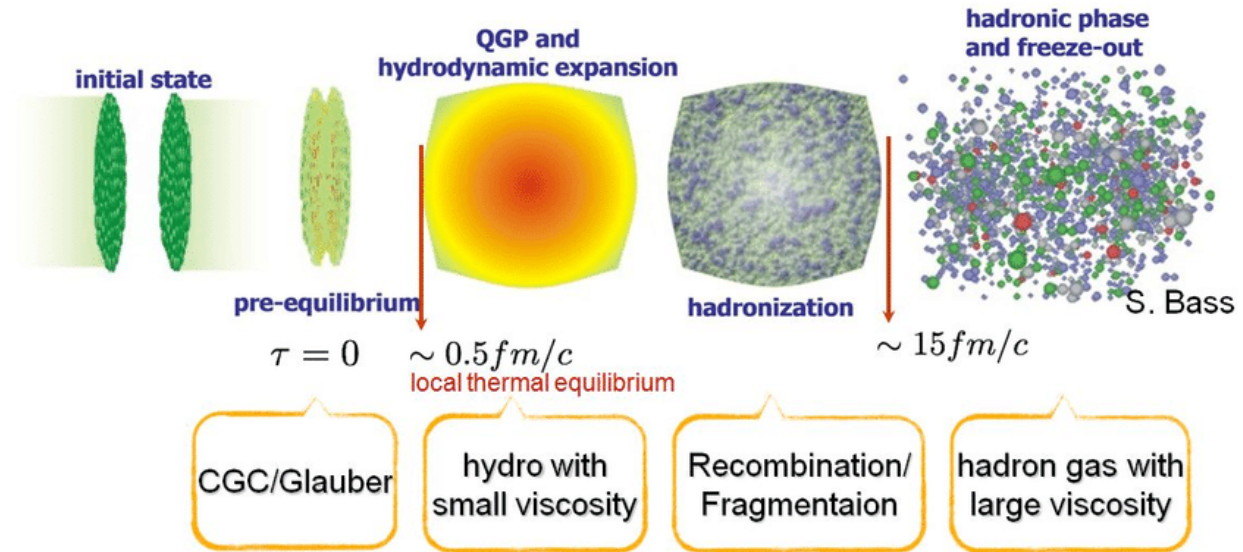


Figure 1.1: Diagram representing the different stages in a heavy-ion collision process. There are essentially five stages: an initial state in which nuclei are about to collide, next is the pre-equilibrium stage where the collision starts to take place, eventually the system enters in the QGP phase and the expansion initiates. As the system cools down, matter starts to hadronize. And finally, as the hadronic gas expands, the system reaches the freeze-out stage. Figure taken from Ref. [5].

The first stage shown in Figure 1.1 is the initial state. This is the stage previous to the collision, when the ions are approaching each other at relativistic speeds, so they look more like plates than spheres in the laboratory frame because of the Lorentz contraction. Instead of perceiving each other as a collection of bounded nucleons, the deep inelastic scattering data

from the ZEUS detector [6] at the Hadron–Electron Ring Accelerator (HERA) experiment from the DESY (in German “Deutsches Elektronen-Synchrotron”) national laboratory suggested that the initial state might be better described by the so-called Color Glass Condensate (CGC). In this state, gluons form a closely packed system, with their density increasing as their momentum fraction decreases. Thus, as the energy increases, smaller and denser packs of gluons appear. This means that their interaction strength becomes weaker and so the system becomes weakly coupled (*asymptotic freedom*). Due to the Lorentz contraction, the colliding nuclei appear as two sheets with a distribution of fast gluons, generating color electric and magnetic fields as they pass through each other. This state is known as *glasma* [7]. Those states will eventually decay and lead to the production of the *Quark-Gluon Plasma* (QGP).

At the third stage of the process, evidence suggests that a thermalization process occurs very quickly, at about 0.5 fm/c after the collision, which means that the system reaches a thermal, local equilibrium phase, the QGP [8]. When the QGP phase is attained, the relevant degrees of freedom shift to the partonic ones. In this situation, quarks and gluons are deconfined from hadrons, and so they are free to be propagated over larger than nucleonic volumes. This process is concentrated in a small volume at the center of the collision. Here, the energy density reaches the critical value of $0.5 - 1 \text{ GeV}/\text{fm}^3$, and this region is denoted as the *fireball* [9]. The fireball has an overall higher temperature than the surrounding region, and thus it undergoes an expansion. As the fireball expands, it cools down and dilutes. The fourth stage of the process begins when matter starts to hadronize.

The newly formed hadrons continue the expansion until two important phenomena occur: the *chemical freeze-out* and the *kinetic* or *thermal freeze-out*. The expansion involves both elastic and inelastic collisions between hadrons. An elastic collision only changes the individual energy and momentum, but inelastic collisions may change the identities. The number of particles of a given particle species is typically referred to as the *abundance*. The chemical freeze-out is defined as the moment when the inelastic collisions cease to exist, meaning that the relative abundances are fixed when this occurs. On the other hand, the thermal freeze-out is defined as the moment when all interactions between hadrons stop. This process occurs when the particles are traveling so fast from each other that the system becomes weakly coupled. These two processes determine the final stage of the collision. Subsequently, particles travel essentially freely until they reach our detectors, but this will be addressed in Chapter 4.

1.2 QCD phase diagram

We can say that heavy-ion collisions are a manner of heating and/or compressing matter over nuclear distances. At normal conditions (of our daily life) both quarks and gluons are confined inside hadrons. But as discussed in the previous section, in heavy-ion collisions, the confinement can be overcome, and consequently new states emerge, such as the QGP. This is analogous as the situation presented in thermodynamics with ordinary matter. The default example is water, which passes through different phases as it is (de)compressed or heated up (cooled down), e.g. from liquid to gas, from liquid to solid, etc. A certain state of a given substance is characterized by its thermodynamical properties, and this characterization can be realized by studying the evolution of a particular thermodynamical parameter (such as temperature, chemical potential, etc.) as a consequence of changes in another parameter(s) value. When the properties of the system change discontinuously by this process, we say that

a *phase transition* has occurred.

There are different ways to classify phase transitions, but for the purposes of this work, the classification introduced by Ehrenfest will suffice [10]. In this context, we can define a first order phase transition as follows: Let us suppose that the chemical potential as a function of the entropy (s) and temperature (T), $\mu = \mu(s, T)$, contains all the thermodynamical information of a given system. If the first derivative of the chemical potential has a discontinuity at some value(s), we say that the system undergoes a first order phase transition¹. Interestingly, we can divide the $\mu = \mu(s, T)$ potential as a piecewise function such that each individual state is determined by a $\mu_i = \mu_i(s, T)$. Thus, the condition for a first order phase transition implies that $\mu_j(s_b, T_b) = \mu_i(s_b, T_b)$ at the boundary values s_b, T_b . This means that, at the boundaries of a first order phase transition, the states coexists.

In the context of QCD, we conjecture the so called *QCD phase diagram* by a finite number of thermodynamic parameters, typically the temperature T and the chemical potentials μ_i [11–14]. Figure 1.2 depicts the key elements of the diagram. On the vertical axis is the temperature, whereas the baryon chemical potential μ_B and the isospin chemical potential μ_I are on the orthogonal axes. The baryon chemical potential represents the baryon density² of the system, a higher baryon chemical potential means higher baryon density. The isospin chemical potential, as the name suggests, represents the isospin (the third component, I_3) of the system. For example, if we consider only the two lightest quarks (u and d) we could define; $\mu_B = (\mu_u + \mu_d)/2$ and $\mu_I = (\mu_u - \mu_d)/2$, where μ_u and μ_d are the chemical potential of each quark type. Most of the predictions concerning the structure of the phase diagram come from calculations of lattice QCD, see e.g. Ref. [15], which can only be realized at vanishing baryon chemical potential because of the *sign problem*³, but some approximations can be made for $\mu_B/T \ll 1$ [16]. Early calculations indicated that the order of the phase transition (or the crossover) is strongly dependent on the number of quark flavors and their masses [17]. For the case of three flavors in the limit of vanishing quark masses, a first order phase transition was predicted. On the other hand, for three quark flavors in the limiting case of infinite quark masses, another first order phase transition was expected. Thus, first calculations indicated the existence of at least two transitions; chiral symmetry restoration (indeed, this symmetry is broken under normal conditions) and the deconfinement phase transition. It was on February 10, 2000 when the CERN announced the discovery of a new state of matter (the QGP) from data of seven different experiments [18]. The announcement may be regarded as controversial, because there is, so far, no unique quantitative way to account for the expected signatures of the QGP [19].

In Figure 1.2, the solid curves in the T vs. μ_B plane indicate the approximately expected form and location of the chiral and deconfinement phase transitions. The dotted lines show what is known as the *crossover* region. The difference is that the thermodynamic parameters do change rapidly but not simultaneously. From the same lattice simulations previously mentioned, in the case of $\mu_B = 0$ and three quark flavours with realistic masses, another

¹We can extend the definition to the n -th order phase transition by the same reasoning, being those whose n -th derivative has a discontinuity.

²It is not exactly the same as the density itself, but they are conjugate parameters in the grand canonical ensemble.

³This is because when a $\mu_B > 0$ is considered, the fermion determinant in the partition function becomes a complex number. Thus, the gluon fields, whose generation probability is related to this determinant, become problematic to interpret.

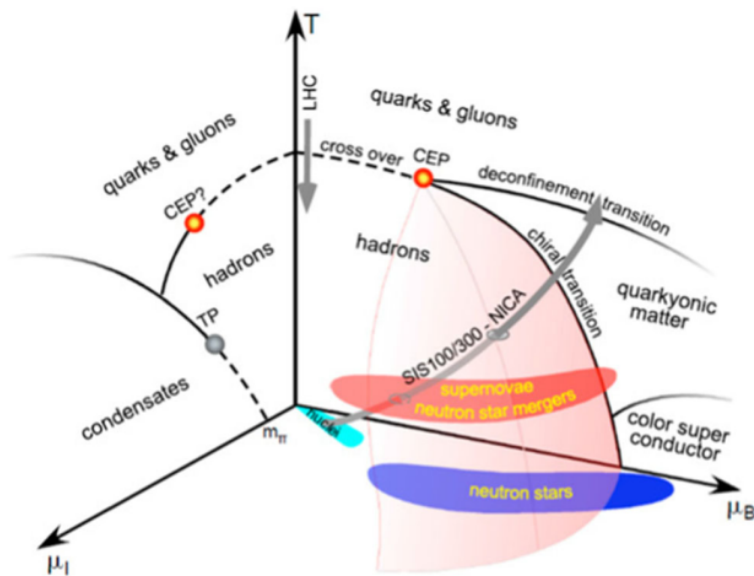


Figure 1.2: QCD phase diagram. The T vs. μ_B plane shows three different types of phase transition: chiral symmetry restoration, deconfinement and color superconductivity. It also shows the crossover region expected from lattice calculations and the Critical End Point. LHC, FAIR and NICA scanning energy regions appear in curved arrows. Figure taken from Ref. [21].

“phase transition” is expected, but not exactly as previously described. It may not even be regarded as a proper phase transition, but rather as a crossover. Calculations estimate that the crossover should occur within the range of $T = 150 - 160$ MeV for vanishing chemical potential [20]. For the case of non-zero μ_B , as stated previously, lattice QCD calculations fail, but the approximations suggest that the crossover line should extend as μ_B increases until it fuses with the line corresponding to the chiral transition at the so-called *Critical End Point* (CEP).

Another two hypothetical states are also plotted on Figure 1.2: the color superconductor (CSC) and the quarkyonic phase transitions. Regarding the CSC, to provide a rough idea, the situation occurs for low temperatures and high baryon chemical potential, at which the system is weakly coupled. As an analogous situation of electrons in a superconductor, it is expected that quarks form Cooper pairs in the QCD ground state. This situation might occur at the cores of massive neutron stars [22].

The quarkyonic state is different and interesting, because chiral and deconfinement phase transitions lines are expected to end at the same point (the CEP). While it remains unclear whether these lines are identical across the entire T, μ_B plane, thereby linking both transitions inseparably, or if the CEP exists at all. The quarkyonic state is expected to occur in the limit of a large number of colors (N_c) [23]. This is known as the ’t Hooft limit, in which $N_c \rightarrow \infty$, with $g_s^2 N_c$ fixed. So, as the number of flavors is fixed, the quark loops are suppressed by a $1/N_c$ factor in comparison with those of gluons. Then, the baryon density increases as the pressure increases with N_c . This is a cold dense matter state called quarkyonic phase. Thus, the existence of this state suggests the separation of the chiral and deconfinement transitions. However, the question remains whether a remnant of this state exists in the $N_c = 3$ QCD phase diagram.

1.3 Prospects of this work

As stated in the previous section, most of the QCD phase diagram is actually unknown, except for the limited predictions from lattice calculations. The diagram may exhibit a more complex or simplified structure compared to that depicted in Figure 1.2. And more importantly, the precise location of the phase transitions, particularly the existence and location of a CEP is speculative. However, recent extrapolations from lattice QCD calculations have shown that the temperature for the chiral symmetry restoration is $T_c^0 = 132_{-6}^{+3}$ MeV in the chiral limit [24], and also provides a constraint for the location of the CEP, such that it cannot be located for values $\mu_B/T \leq 2$ and $145 \leq T \leq 155$ MeV [25].

On the other hand, experimental data from SPS, AGS and SIS⁴ show a systematic behaviour for the freeze-out parameters [26]. The result can be summarized as follows. As the energy of the collision increases, an increase of the freeze-out temperature is observed, and correspondingly, a decrease of the baryon chemical potential. This observation is illustrated in Figure 1.3 by a curve in the T, μ_B plane, representing the values of the thermal parameters at chemical freeze-out. Another interesting observation is that hadron abundances in central heavy-ion collisions should be established close to the phase boundaries [27]. We can link these two observations by recalling that (at chemical freeze-out) the hadronic abundances are fixed, and thus the curve in the T, μ_B plane should be located close to the boundaries of the phase transition.

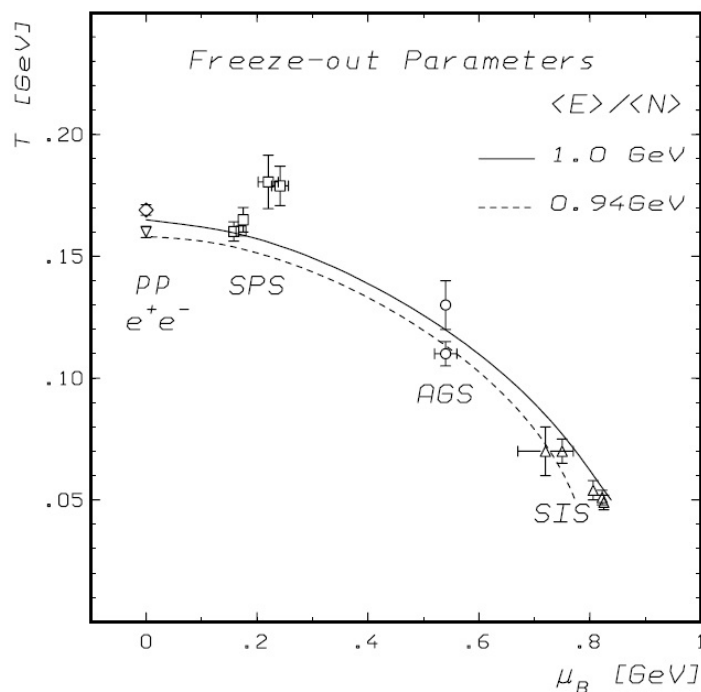


Figure 1.3: A T vs. μ_B plot in the region where the chemical freeze-out occurs. SPS, AGS and SIS data are fitted to a solid line corresponding to an energy of 1 GeV per hadron (and a dotted line of 0.94 GeV per hadron), showing a systematic behaviour at freeze-out. This figure is taken from Ref. [26].

⁴A heavy-ion synchrotron located at the GSI Helmholtz Centre for Heavy Ion Research in Darmstadt, Germany.

Given that the hadron spectrum is determined at freeze-out, we can obtain both the temperature and baryon chemical potential indirectly by measuring the *transverse momentum* distributions in our experiment and then calculating the *particle ratios* from the yields. This idea will be expanded mainly in Chapter 5, to provide a clearer understanding of our approach. Furthermore, one of the main goals of this work is to establish a proper framework for the measurement of these quantities.

Experimental results, such as those from the BES-I, and the expected data of the BES-II, programs from RHIC [28], indicate a promising future in the search for evidence of the phase transitions. These includes the search for the existence (or not) of the CEP at the relatively low and high baryon density regions. Also, future experiments such as FAIR and NICA aim for this goal. As members of the MPD-NICA Collaboration, we are particularly interested in the latter. MPD aims at the energy range of 4-11 GeV/n in the center-of-mass frame. The expected temperature for the CEP (T_{CEP}) is anticipated to be at lower values than the chiral transition found in Ref. [24], which coincides with the constraints in Ref. [25], i.e. $T_{\text{CEP}} < T_c^0$. And by taking the parametrizations of the temperature and baryon chemical potential given in Ref. [29], which present a good fit for the freeze-out parameters in Figure 1.4,

$$T(\mu_B) = a - b\mu_B^2 - c\mu_B^4 \quad , \quad \mu_B(\sqrt{s_{NN}}) = \frac{d}{1 + e\sqrt{s_{NN}}} \quad , \quad (1.1)$$

with $a = 0.166 \pm 0.002$ GeV, $b = 0.139 \pm 0.016$ GeV $^{-1}$, $c = 0.053 \pm 0.021$ GeV $^{-3}$, $d = 1.308 \pm 0.028$ GeV and $e = 0.273 \pm 0.008$ GeV $^{-1}$ fit parameter values.

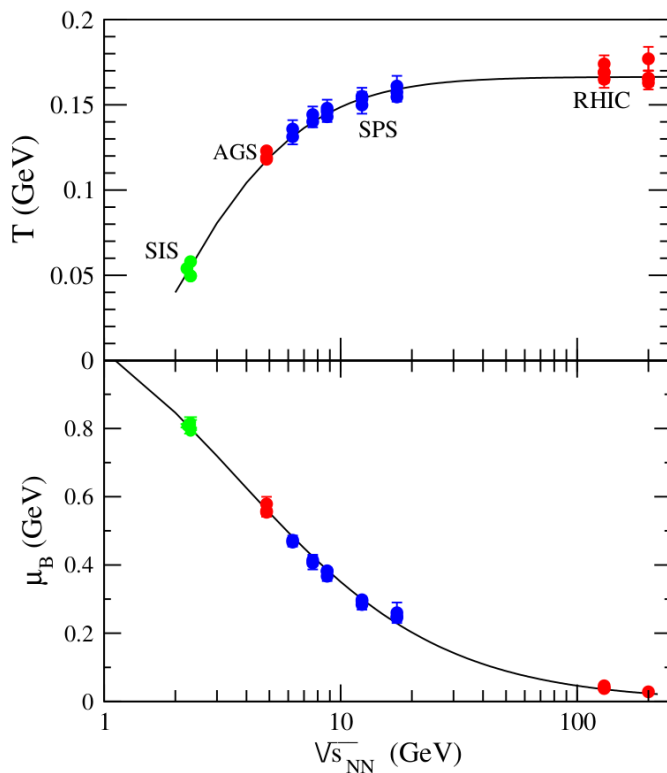


Figure 1.4: Fit for the freeze-out parameters with SIS, AGS, SPS and RHIC data. Nine different energies are considered, 130, 17.3, 12.3, 8.77, 7.62, 6.27, 4.86, 2.32 and 2.24 GeV/n from Au+Au and Pb+Pb collisions. Figure is taken from Ref. [29].

Then we expect to find the CEP at energies $\sqrt{s_{NN}} < 6$ GeV, which is within the energy range covered by the MPD. Enhanced fluctuations near the CEP are also anticipated, which could be measured by using the particle ratios. While not a focus of this work, it remains an intriguing question for future research.

There are some key features of heavy-ion collisions which have been proposed as signatures of the onset of the deconfinement [19]. One feature of particular interest for this work is the enhancement of the strangeness production with respect to $p + p$ collisions. Figure 1.5 is a plot of the ratio of average K^+ to average π^+ production per event vs. collision energy. Experimental data from three different heavy-ion collision experiments (colored symbols) are compared to proton-proton collisions (blank symbols). A striking difference is observed, the ratio in the $p + p$ case rise slowly with the collision energy. For the case of the A+A (nucleus+nucleus) collisions, a sharp rise in the ratio is observed, followed by a decrease around 8 GeV. Assuming the formation of a QGP phase, the explanation is as follows: as the fireball expands, the strangeness content increases until it reaches the equilibrium. The time taken to reach the equilibrium is expected to be < 10 fm, which is within the same range as the time of the collision process. The difference is that when no QGP phase is assumed, the equilibration time is about 10 times longer. This implies lower production rate, leading to a reduced strangeness production.

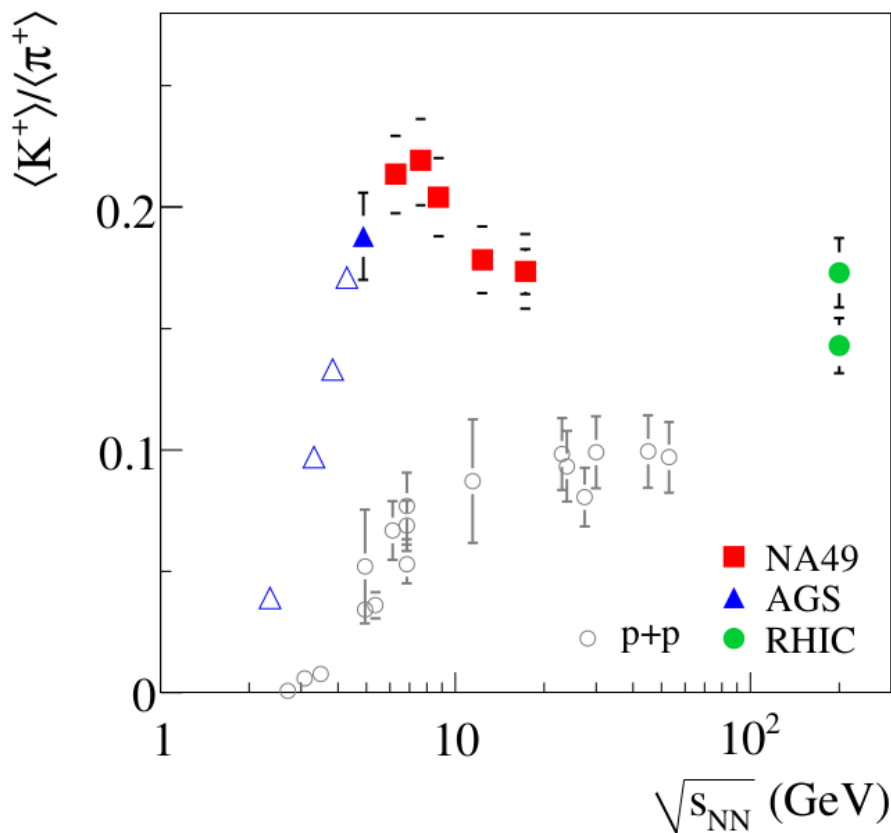


Figure 1.5: Kaon to pion ratio vs. collision energy. Colored symbols represents the experimental data in heavy-ion collision experiments: NA49 (red), AGS (blue) and RHIC (green). White open circles show the experimental data in proton-proton collisions. Figure is taken from Ref. [19].

The statistical models can predict in good agreement (at least at NICA energies) the abundances of mesons and baryons at a given collision energy. These models have already proven capable of predicting the horn structure observed in the K^+/π^+ ratio [30], which has been suggested as a signal of the CEP in the QCD phase diagram [31]. A more detailed description of the different types of models used to study heavy-ion collisions will be given in Chapter 3. In this context the explanation emerges, in a statistical manner, that the maximum of the ratio is not attributed to a phase transition from a confined to a deconfined medium, but instead to a transition from a baryon- to a meson-dominated gas. The model indicates that the hadronic gas undergoes a transition, such that if we look at the total entropy as a function of the collision energy (Figure 1.6 (top)), the contribution is mainly baryonic for values lower than 8.2 GeV, whereas the contribution is mainly mesonic for higher values [32].

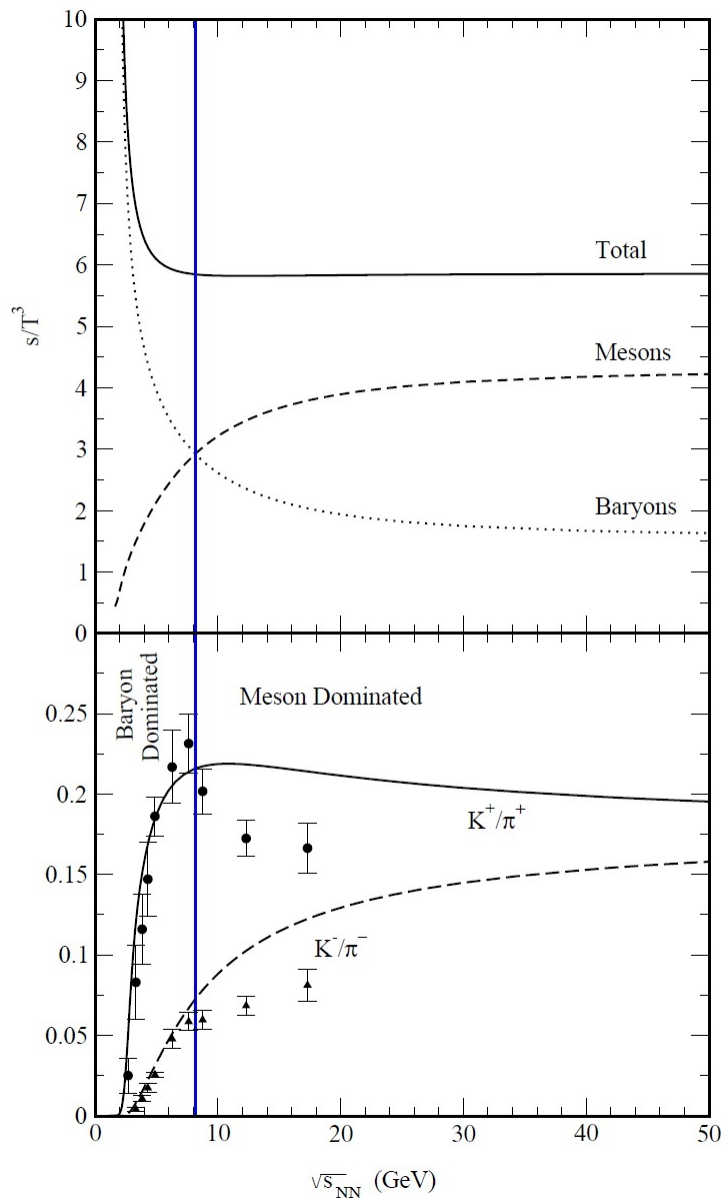


Figure 1.6: Entropy vs. collision energy in the statistical model (top). Experimental data for the K^\pm/π^\pm ratio compared to the value predicted by the model (bottom). Figure adapted from Ref. [32].

In Figure 1.6 (bottom), we observe that the agreement between the data and the statistical model is good up to 8.2 GeV, where the model suggests that the hadronic gas undergoes a transition. For higher collision energies the agreement is quantitatively not good, but qualitatively it shows approximately the same behavior.

There are, of course, specific signals to be expected for different phase transitions, but they will not be discussed in this work. The primary objective of all heavy-ion collision experiments can be simplified by stating that they aim for a complete exploration of the QCD phase diagram.

Another objective of this work is to test three different models: two of them do not include a QGP phase, but their frameworks are quite different. The third model is the same as one of the previous ones, except that it does include a QGP phase. The idea is to compare their predictions to experimental data and propose an explanation of the results. In the following chapter, a review of the NICA project is provided, with an emphasis on the MPD experiment.

Chapter 2

Nuclotron-based Ion Collider fAcility

The Joint Institute for Nuclear Research (JINR) was founded in 1956 by a convention signed by eleven nations. Its headquarters are located in Dubna City, in the Russian Federation. Nowadays JINR consists of 16 member states and comprises seven laboratories employing around 1200 scientists [33].

As part of a mega-science project of JINR, the Nuclotron-based Ion Collider fAcility (or “NICA complex”) is under construction; its commissioning is expected in 2025. The facility will consist of a set of ion sources, two linear accelerators, a Booster, a superconducting heavy-ion synchrotron (the Nuclotron) with an extraction line for the Baryonic Matter at Nuclotron (BM@N) detector, and two superconducting rings serving as a collider with two interaction points; one for the Spin Physics Detector (SPD) and one for the Multi-Purpose Detector (MPD).

The NICA complex is planned as a three stages project [34]. The first stage consisted of the construction of the “new injector” and the Booster-synchrotron, the modernization of the Nuclotron and finally the commissioning of the BM@N detector (this was finished in 2016). The second stage includes the construction of the Collider, the beam transfer line from Nuclotron to Collider, and finishing with the commissioning of the MPD (expected in 2025). And the last stage will consist of the construction of the SPD. A schematic illustration of the expected structure of the whole facility is shown in Figure 2.1.

The aim of this mega-science project is, generally speaking, to study the properties of nuclear matter in the region of high baryonic density. One of the investigation lines is connected to the particle production at NICA energies: experimental data such as the hadron production properties at the CERN-SPS [14] suggest a deconfinement (phase) transition and chiral symmetry restoration approximately at NICA energies. The production mechanisms of mesons and baryons are therefore connected to deeper questions regarding the QCD phase diagram, and the study of their production will be the focus of this work.

2.1 Injection complex

The first stage consists of the production and injection of the ions, and is called the injection complex [35, 36]. Particle production is achieved by using different ion sources. Then the injection process is divided into two main chains: one corresponding to the injection of light ions, and one for the heavy ions.

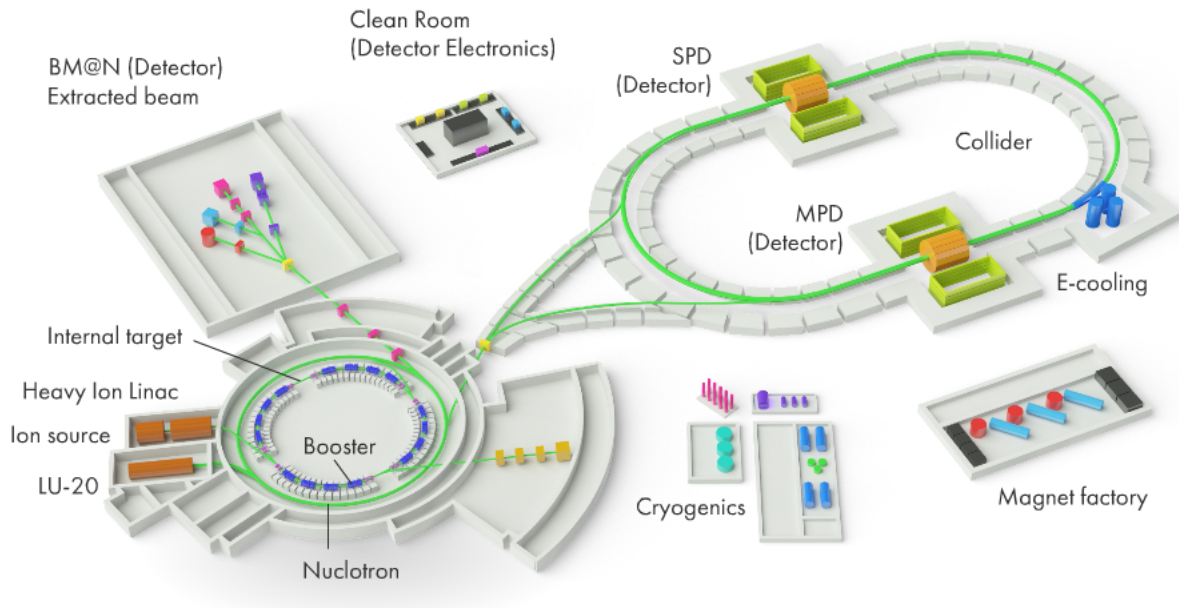


Figure 2.1: Schematics of the planned NICA complex taken from Ref. [35]. The main parts include: the injection complex (ion sources + linear accelerators), Booster, Nuclotron, collider rings and three main detectors (BM@N, SPD and MPD).

For the production of light ions, NICA employs a laser ion source, duoplasmatron¹ sources, and a source of polarized protons and deuterons. The sources are directed to the so called “fore-injector” (see Figure 2.2), based on the Radio-Frequency Quadrupole (RFQ) technology, which provides an output energy of about 156 keV/n.

Then, the fore-injector is connected to a linear accelerator (Alvarez-type linac LU-20), which has been in operation since 1974 and was recently updated [37] to work as an injector for light ions directly to the Nuclotron through a transfer line called LU-20-Nuclotron. At the exit, the ions carry an energy of ~ 5 MeV/n. The replacement of the LU-20 by a Light Ion Linac (LILAc) is expected and currently under development for future research with polarized proton beams [38].

On the other hand, heavy ions are produced by the KRION-6T, a superconducting electron-string heavy-ion source, which generates 5×10^8 $^{197}\text{Au}^{31+}$ and 2×10^8 $^{209}\text{Bi}^{27+}$ ions per pulse [36, 39]. These ions are delivered to the accelerator via a Low Energy Beam Transfer (LEBT) channel.

The Heavy Ion Linear Accelerator (HILAc) was commissioned in 2016 [40, 41], and consist on three accelerating sections; one RFQ and two Interdigital H-type² cavities (IH). At the end, the ions are transported to the Booster with an energy of ~ 3.2 MeV/n through a transfer line consisting of: two dipole magnets, seven quadrupole lenses, six stirrers magnets, a debuncher, a collimator, and vacuum and diagnostic equipment. This setup aims to achieve a beam transportation efficiency of at least $\sim 90\%$ at the exit.

¹A duoplasmatron basically consist of a heated filament emitting electrons directed to a vacuum chamber, in which small amounts of gas are progressively added to form a plasma for later acceleration. This is used for the production of H and He beams.

²H-type cavities are characterized by the direction of the RF magnetic field, which flips to be parallel and antiparallel with respect to the beam axis.

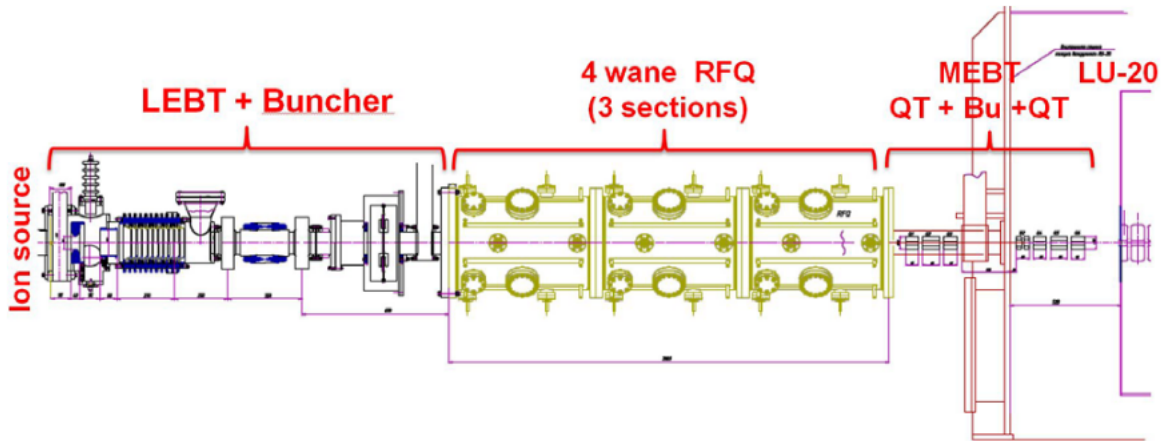


Figure 2.2: Fore-injector for the LU-20. It consists of LEBT+Buncher+RFQ+MEBT designed to transport the ions coming from the ion source (left side) to the LU-20 (right side). Figure taken from Ref. [37].

2.2 Booster, Nuclotron and Collider

The Booster is a superconducting ring with a circumference of 211 m and a maximum magnetic rigidity of $25 \text{ T}\times\text{m}$, mounted inside the yoke of the Synchrotron magnet³. It is designed for the accumulation of $2 \times 10^9 \text{ Au}^{31+}$ ions up to an energy of $\sim 600 \text{ MeV/n}$; this is the energy required for an effective stripping of the ions to the bare nucleus state. Another important task is to form the required beam emittance via the electron cooling system. This is necessary because the Nuclotron ring has no convenient straight sections for the location of the cooling system, therefore the Booster is the only place where beam cooling can be realized.

The ring consists of four symmetric quadrants inside the yoke, see Figure 2.3. Each of the quadrants has ten dipole magnets, six focusing and six defocusing quadrupole lenses, and multipole corrector magnets. The dipole magnets have an effective field length of 2.2 m, with a curvature radius of about 14 m each, while the quadrupoles have an effective field length of 0.4 m each [42]. Additionally, the four large straight sections of the Booster will be used for the injection of the ions, extraction to transfer the beams into the Nuclotron, and the placement of the Radio-Frequency cavities (RF) and Electron Cooler (EC). The RF system provides 10 kV of acceleration voltage, while the EC system decreases the ion beam longitudinal emittance to about 100 MeV/n.

To extract the beam from the Booster for transport to the Nuclotron, a system consisting of a magnetic kicker, two magnetic septa, a stripping station, and a closed orbit bump subsystem are employed. The ions are then transported along a magnetic channel, where they pass through a stripped target. It is expected to achieve a total beam extraction efficiency from the Booster-Nuclotron transfer line of $\sim 70\%$.

The Nuclotron is a superconducting proton synchrotron with a circumference of 251 m and a maximum magnetic rigidity of $45 \text{ T}\times\text{m}$. It was constructed from 1987 to 1992 and has

³The Synchrotron was operative from 1957 to 2002, and accelerated protons and deuterons (later also heavier nuclei) up to 6 GeV/n, with the magnet having a strength of 1.3 T and weighting 36000 tons. After removing the magnetic winding, the iron yoke was left, creating a tunnel with enough space to place the Booster inside.

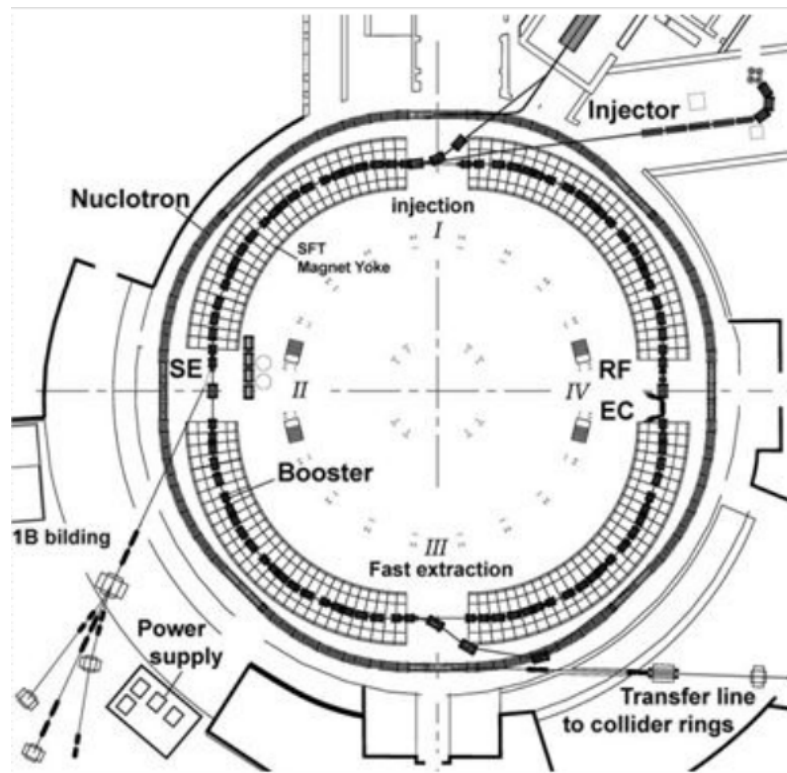


Figure 2.3: Booster and Nuclotron diagrams. The Booster shows explicitly the acceleration and bending components, as well as the transfer lines connecting it to the injection complex and Nuclotron. The Nuclotron includes the transfer lines to the BM@N and collider rings. Image taken from Ref. [42].

been in operation since 1993. However, its main systems were modernized, starting in 2006, when the NICA project was first discussed [43].

Currently the Nuclotron is only employed for fixed target experiments (with slow extraction to the BM@N) or internal target experiments. A fast extraction transfer line will be connecting the Nuclotron to the Collider [44]. Therefore, the Nuclotron has three main operation modes: two of them are focused on injection into the Collider, with one mode accelerating heavy ions from 0.6 to 4.5 GeV/n and the other mode accelerating polarized light ions from 0.05 to 12 GeV/n. The third operation mode pertains to fixed or internal target experiments for both types of ions.

The Collider will consist of two superconducting rings located one above the other, with a vertical separation of 32 cm between their median planes, and having two interaction points where the collision occurs. Each ring will have a racetrack-shaped structure with a circumference of 503 m, featuring two arc cells at both ends and two long straight sections (see Figure 2.4). The design specifications for the Collider include operating at 4.5 GeV/n for heavy ion collisions, 12 GeV/n for proton-proton collisions, and 6 GeV/n for deuteron-deuteron collisions, with a luminosity of $5 \times 10^{27} \text{ cm}^{-2}\text{s}^{-1}$ [45].

In each arc of the Collider, there will be a total of 12 cells arranged in a FODO (F=focusing quadrupole, O=“empty space”, D=defocusing quadrupole, O=“empty space”) geometry. Each cell will have a length of 11.96 m and will include four dipole magnets, three quadrupole magnets, a pick-up (PU) station, and a set of multipole correctors (see Figure 2.5). The long straight sections of the Collider will house three independent RF systems: RF1X, RF2X, and

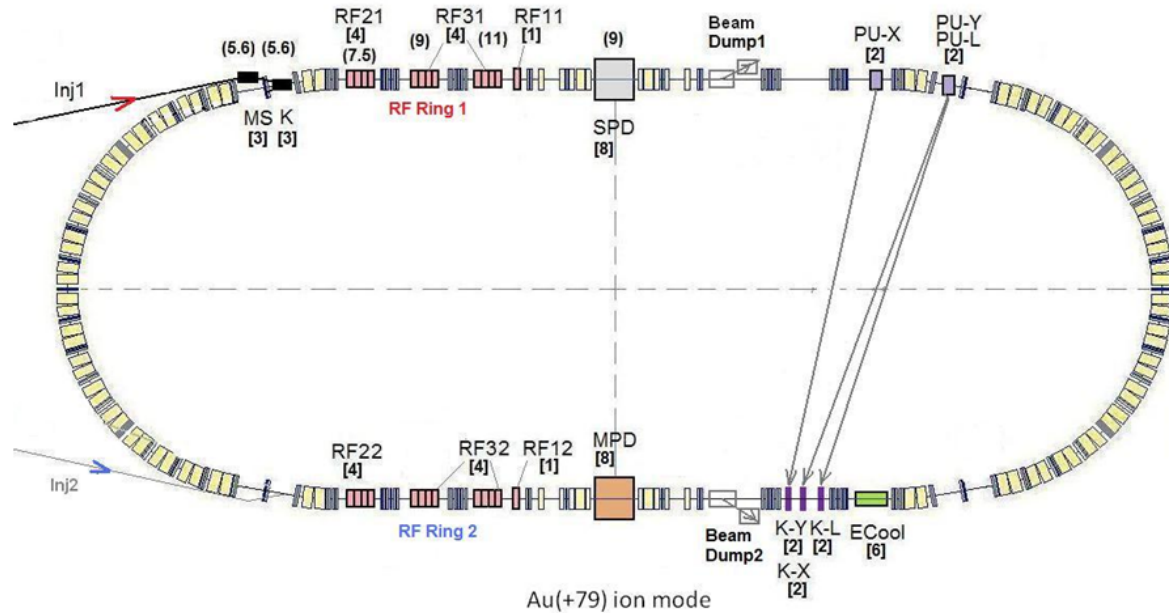


Figure 2.4: Collider design diagram taken from Ref. [35]. The long straight sections include the acceleration components as well as the SPD and MPD detectors. The two arc sections include the bending magnets.

RF3X. These systems serve several purposes, including allowing the storage of the required beam intensity, providing beam bunching and compression, and ensuring the necessary bunch length for collision experiments. Additionally, there will be two “Beam Dump” systems employed for beam reset. For the energy range from 1 to 3 GeV/n, the electron cooling system (Ecool) will be employed. For the energy range of 3 to 4.5 GeV/n, the stochastic cooling system will be utilized. This system consists of pick-up (PU) electrodes in the horizontal, vertical, and longitudinal directions (PU-X, PU-Y, PU-L) and kickers for each of these directions (K-X, K-Y, K-L). The SPD and SPD detectors will be placed on opposite sides at the center of the straight sections.

2.3 BM@N and SPD detectors

The beam transport line, from the exit of the Nuclotron to the target of the BM@N detector, is 160 m long and is composed of 8 dipole magnets and 18 quadrupole magnets. The main purposes of the BM@N are: the exploration of the reaction dynamics and the equation of state (EoS) of nuclear matter, study of in-medium properties of hadrons, production of (multi)strange hyperons in the vicinity of the threshold and searches for hypernuclei [46].

The layout configuration of the detector is presented in Figure 2.6, and consists of the following components [47]:

- Start Diamond Detector (T0): It consists of a diamond pixel or strip detector due to the high radiation hardness, serving as the starting point for measuring particle tracks.
- Target Station (TS): This is where the target is located, and it is where interactions between the beam and the target material take place.

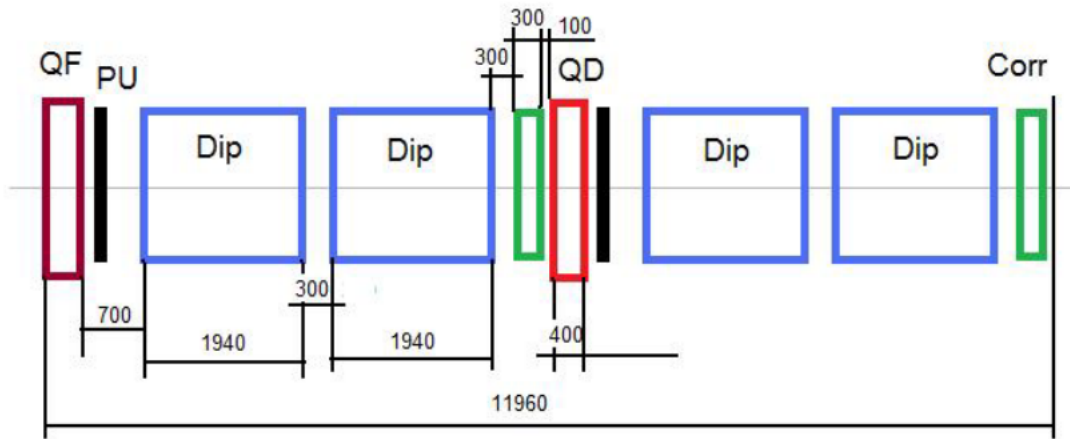


Figure 2.5: The FODO structure for each cell (12 per arc). Each array consists of a focusing quadrupole (QF), 2 sets of dipoles (dip), a defocusing quadrupole (QD) and 2 sets of dipoles (dip) + multipole correctors. Image taken from Ref. [45]

- Silicon Tracker System (STS): The STS comprises eight planar tracking stations, each equipped with silicon microstrip sensors. These stations are placed inside the 2.2 m long dipole magnet SP41.
- Straw Tubes system (ST): The ST system contains three identical octagonal chambers, each consisting of two modules with overlapping straw tubes inserted into a carbon frame.
- Drift Chambers (DC): The DC system consists of two identical octagonal chambers, each containing eight planes of grounded sense wires oriented in four different directions. The chambers use a gas mixture of carbon dioxide and isobutane in the ratio 49:1.
- Resistive Plate Chambers (RPC): The RPC system employs multigap-RPC technology, specifically glass mRPCs. The design consists of modules with ten-gap chambers formed by two identical stacks with read-out strips between them, and each stack is constructed using six glass plates.
- Zero Degree Calorimeter (ZDC): The ZDC consists of 104 modules, each containing scintillators, wave-length-shifters (WLS), rectangular iron containers, and photomultipliers (PMTs).

The functioning of the BM@N detector can be summarized as follows. T0 starts the signal and the collision with the fixed target is produced. Then the particle identification is done by the Time Of Flight system, starting from the T0 signaling and ending by the RPC wall, together with the STS. Particle identification is achieved by means of the m^2 vs. p plots. The ST and DC systems are used for intermediate distance tracking. They provide information on the trajectory and momentum of charged particles. Finally the ZDC provides the centrality measurements, because the centrality is related to the the impact parameter (this two concepts will be explained in the next chapter), but experimentally this is not a measurable quantity. Instead one can refer to the energy carried away by spectators.

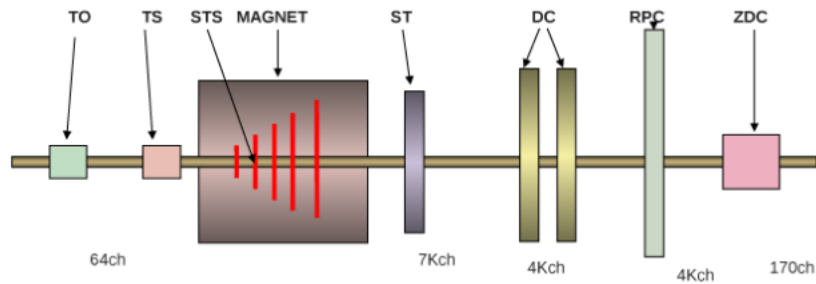


Figure 2.6: Schematic view of the BM@N detector. The subdetectors are, from left to right: start diamond detector, target station, silicon tracker system, magnet, stray tubes, 2 drift chambers, resistive plate chambers and a zero degree calorimeter. Figure taken from Ref. [47].

Given that most of the spectators have a small transverse momentum, they will travel mostly unaffected in the beam direction. So to measure their energy we use a calorimeter positioned at a “zero angle”, the ZDC.

In 2016, the BM@N detector was commissioned for operation, with a deuteron beam serving for a test run. Currently, it is the only functioning detector within the planned NICA complex.

On the other hand, the SPD detector is still in the early stages of construction, and will be the last part of the NICA project to be completed. However, the conceptual design of the detector was approved in 2022 by the Advisory Committee [48].

The SPD experiment aims to obtain valuable information about the gluon Transverse Momentum-Dependent Parton Distribution Functions in the proton and deuteron. Additionally, it intends to study the gluon transversality distribution and tensor PDFs in the deuteron. These investigations will be conducted by measuring specific single and double spin asymmetries, utilizing various probes such as charmonia, open charm, and prompt photon production processes.

In the planned construction of the SPD, there are two stages outlined. The first stage, scheduled to commence in 2026 and to be commissioned by 2028, will focus on establishing the polarized infrastructure. The second stage, planned for 2030 with commissioning targeted for 2032, will involve infrastructure upgrades. It is important to note that the detector’s capabilities for studying heavy-ion collisions will be limited due to the design optimized for high luminosity ($\sim 10^{32} \text{ cm}^{-2}\text{s}^{-1}$) and low track multiplicity. Consequently, while there are expectations to operate in heavy-ion mode during the second stage, the primary focus of the experiment will be on polarized proton-proton ($p+p$) and deuteron-deuteron ($d+d$) collisions.

The layout configuration of the SPD detector for the first stage is depicted in Figure 2.7. A detailed description is given in Ref. [49], which can be summarized as follows:

- Range System (RS): Consists of a octagonal barrel structure with two end-caps. The central barrel is filled with an ArCO_2 gas mixture. The steel elements of the RS serve as a yoke for the magnet, and a superconducting solenoid completes the magnetic system.
- Straw Tracking system (ST): Barrel with two end-caps assembled from approximately 26,000 PolyEthylene Terephthalate (PET) straw tubes.
- Micromegas-based Central Tracker (MCT): Utilizes micromesh gaseous structure technology. It consists of a set of parallel plate counters with dedicated ionization and

amplification gaps, separated by a fine mesh. The detector is organized in three superlayers, each consisting of 2 or 3 layers with different strip orientations and their respective end-caps.

- **Beam-Beam Counters (BBC):** There will be two BBC detectors, each located between the ST and RS end-caps. Each detector is a cylindrical structure consisting of 80 large pads in 5 radial layers. The internal ring is subdivided into 32 sectors, covering the polar angles between 60 and 500 milliradians.
- **Zero Degree Calorimeter (ZDC):** Two ZDC detectors are placed in symmetrical positions at approximately 13 m from the interaction point. Each ZDC is assembled by individual planes, and each plane has a printed circuit board (PCB) with Silicon-Photomultipliers (SiPMs), scintillator tiles, and tungsten absorbent plates.

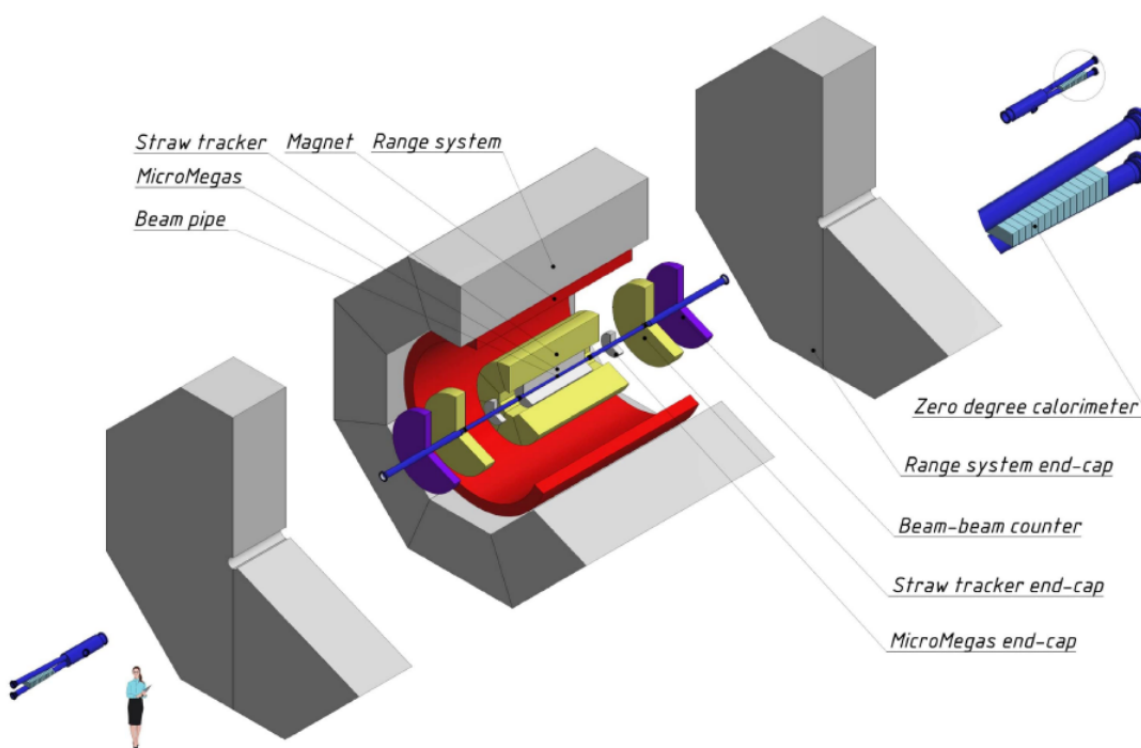


Figure 2.7: Schematic view of the SPD detector. Only the main subdetectors for the first stage of the apparatus are shown. Figure taken from Ref. [49].

A brief and general description of the functioning of the detector is as follows. The RS has two main purposes: the identification of muons in the presence of a significant hadronic background and the estimation of hadronic energy. This means that the RS works both as an absorber for hadrons and a “filter” for muons. The ST system provides the information on the trajectories of the reconstructed tracks of primary and secondary particles based on the track curvature inside the magnetic field. The MCT plays a crucial role in improving the momentum resolution and tracking efficiency. Its positioning at the central position compensates for the absence of a tracker close to the beam pipe. As for the BBC, the main purpose is the permanent monitoring of the beam polarization during data taking to reduce the error coming

from the beam polarization variation, and also providing a luminosity and timing control. Finally, the ZDC has various tasks, including luminosity measurement, spectator neutron tagging, time tagging of events for event selection, local polarimetry with forward neutrons, and providing the necessary measurements for particle identification, such as the energy loss per length dE/dx .

2.4 The Multi-Purpose Detector (MPD)

2.4.1 MPD Collaboration and MexNICA

The second stage of the NICA project, currently under construction, will culminate with the commissioning of the Multi-Purpose Detector (MPD) in 2025. This phase of the project involves an international collaboration among 10 countries: Armenia, Bulgaria, China, Georgia, Mexico, Moldova, Mongolia, Russia, Serbia, and Slovakia. At present, it encompasses 35 participating institutions and involves over 500 active members. Since 2016, a number of students and researchers form the MexNICA group with the objective of contributing to the experimental efforts of MPD-NICA by proposing a BEam-BEam counter detector, and also contributing with theoretical work as well as with simulations and data analysis [50]. The MPD collaboration was established in 2018, with the purpose to construct, commission and operate the detector. However, one year later, in 2019 Mexico officially joined the NICA project.

The primary scientific goal of the MPD is to explore the baryon-rich region of the Quantum Chromodynamics (QCD) phase diagram by colliding heavy nuclei within the energy range of $4 \text{ GeV} \leq \sqrt{s_{NN}} \leq 11 \text{ GeV}$. This energy range represents a narrow region of moderate energy. While previous experiments at various facilities such as SPS, RHIC, SIS, and AGS have partially explored this region, the MPD aims to bridge the gaps and provide a more comprehensive understanding of the physical phenomena occurring in this energy regime.

2.4.2 Detector layout configuration

Similar to the SPD, the construction of the MPD is planned as a two-stage process. In the first stage, all the necessary subsystems will be implemented to enable initial characterization and measurements of particle momentum, tracking, centrality, and collective flow studies. This stage focuses on establishing the core functionality of the detector and conducting fundamental research. The second stage of construction will involve the incorporation of additional detectors to further enhance the capabilities of the MPD. These additional detectors will enable the detection of muons originating from external sources, expanding the range of measurements that can be performed. This stage aims to broaden the scientific scope of the MPD experiment and facilitate more comprehensive studies of the collisions and phenomena occurring in the baryon-rich region of the QCD phase diagram.

The first part of the MPD consists of several components shown in Figure 2.8, which are described in some detail below, following Refs. [51, 52]:

- Time Projection Chamber (TPC): The central barrel of the MPD houses the TPC, a cylindrical structure composed of 12 modules. The TPC is 340 cm long with inner and outer radii of 27 cm and 140 cm, respectively. It is divided into two halves by a

central electrode, creating a uniform electric field of 140 V/cm along the axis. Charged particles passing through this region ionize the gas mixture of 90%Ar plus 10%CH₄, and the ionization charge is collected by the Read-out chambers (ROC), which consist of Multi-Wire Proportional Chambers (MWPC).

- Time Of Flight system (TOF): Surrounding the TPC, the TOF consists of 14 plate sectors, each formed by two modules. The TOF has a total length of 590 cm and employs the Multigap Resistive Plate Chambers technology (280 in total). The gas mixture used in the TOF is 90% C₂H₂F₄, 5% SF₆ and 5% i-C₄H₁₀.
- Electromagnetic calorimeter: The MPD features an electromagnetic calorimeter consisting of 50 isolated half-sectors forming a cylindrical shell with a length of 624 cm. It has inner and outer radii of approximately 168 cm and 230 cm, respectively. Each half-sector contains 48 calorimeters: (8 modules of different types in the longitudinal direction) × (6 modules in the transverse direction). Each module consists of 16 towers of 40 × 40 mm² transverse cross-section with a lead-scintillator sandwich that contains 210 tiles of Pb interleaved with 210 tiles of plastic scintillator.
- Forward Hadron Calorimeters: Includes two identical Forward Hadron Calorimeters placed at 3.2 m upstream and downstream from the center of the MPD. Each calorimeter has 44 modules, and each module consists of 42 lead-scintillator sandwiches enclosed in a stainless steel box. Scintillator tiles are covered with a white reflector to enhance light collection, and compact SiPMs are coupled to the optical connectors at the rear side of the module.
- Fast Forward Detector (FFD): The FFD consists of two modular arrays with 20 Cherenkov modules. Each module comprises a lead converter, a quartz radiator, PMTs, and board circuitry. The FFD has an acceptance range of $2.7 < |\eta| < 4.1$, corresponding to a polar angle range of $1.9^\circ < |\theta| < 7.3^\circ$.

After the collision, a multitude of particles is emitted and interact with the detectors. Each component of the MPD plays a crucial role in the identification process. The FFD is responsible for triggering A+A collisions and providing the start time required for the Time Of Flight (TOF) measurement. The track reconstruction is based on the drift time and $R - \varphi$ cylindrical coordinate measurement of the primary ionization clusters created by the charged particles passing through the TPC. The minimal two-track resolution is ~ 1 cm, then a measurement of the specific ionization energy loss dE/dx can be applied on a track-by-track basis. Momentum reconstruction relies on the curvature of the reconstructed tracks, enabling the identification of charged particles with transverse momenta (p_T) greater than 50 MeV/ c . The TPC alone can discriminate between charged pions and kaons up to momenta of about 0.7 GeV/ c , and between kaons and protons up to approximately 1.1 GeV/ c . The TOF detector provides both time and coordinate measurements with an accuracy of around 80 ps and 0.5 cm, respectively. It employs a matching procedure to associate TPC tracks with hits in the TOF detector. The matching involves extrapolating the TPC track to the TOF surface and finding the nearest TOF hit within a predetermined window (matching window). The size of the matching window is determined to balance the TOF's intrinsic performance (time and coordinate resolutions) with the overall occupancy in heavy-ion collisions. The expected reconstruction efficiency is approximately 80% for particles with momenta up to 1.7 GeV/ c .

Chapter 3

Event generators

There are several software packages available to simulate the collision process. These are generally referred to as *event generators*. Usually, they generate the initial conditions using a Monte Carlo (MC) approach based on a specified model. Each model contains a set of equations to describe the system, which are later dynamically evolved to solve it. A common and relatively simple framework to exemplify this is the Glauber Model [53, 54]. In this model, one treats the whole process as multiple (nucleon-nucleon) collision processes. The distributions of the nucleons in each nucleus is randomly assigned, as well as the *impact parameter*, which determines the distance (in the transverse plane to the beam direction) between the centers of the colliding nuclei. These initial conditions determine the geometry of the system, and the whole dynamics is given by the total inelastic cross section.

As discussed earlier, the collision itself is a very complicated process of many stages. The idea with the event generators is to simplify the calculations, so that the computer can solve the system in a moderate amount of time, while maintaining the physics of collision as close as in the real experiments. Those event generators rely on one particular or a combination of (different) models. Perturbative QCD usually offers theoretical calculations for certain high energy processes, while transport theory handles non-equilibrium processes, and hydrodynamics describes the macroscopic dynamical evolution. Typically, the event generators are designed to cover a limited energy region, where the model is applicable. And even if the model can be extended by applying some major modifications, no model so far is well suited at all energies. Therefore, event generators are usually constructed with a specific energy range in mind, and their corresponding free parameters are adjusted to fit experimental data within that range.

We can divide the models employed by the event generators into three types [55, 56]:

- *Statistical models or Hadron Gas Resonance (HGR)*: These models are typically described by a grand-canonical ensemble. For them to reproduce the spectra, thermal and chemical equilibrium must be attained at freeze-out. Such models are well-suited for accounting for particle abundances. Within this framework, most of the results discussed in Chapter 1 were obtained. Particularly the freeze-out line, which shows that as energy increases, additional energy is used to create more particles rather than increase the system's temperature. The model is constrained by a maximal temperature known as the *Hagedorn temperature* beyond which the hadronic description of the model is not applicable, thus suggesting the existing of a deconfined phase.

- *Hydrodynamic models*: In hydrodynamic approaches, the system is considered as a single fluid (or multiple fluids) whose evolution is governed by an Equation of State (EoS). This approach assumes that the system undergoes thermalization at a certain stage. The determination of this EoS is typically carried out in a phenomenological manner, often constructed from lattice QCD results or by incorporating an EoS with an explicit phase transition. Due to their collective behavior, hydrodynamic approaches are particularly well-suited for analyzing spectra and flow.
- *Microscopic transport models*: In these models, the evolution of the system is given by the dynamics between hadrons, the formation of strings and (if incorporated) partons. The dynamics are determined by the nuclear EoS and cross sections derived from experimental data. The advantage is that these models do not rely on equilibrium assumptions, because they follow from a kinetic theory. In addition to studying spectra and particle abundances, these models allow for correlation and fluctuation analyses.

For this work, two event generators were employed: the Ultra relativistic Quantum Molecular Dynamics (UrQMD) and the Parton-Hadron-String Dynamics (PHSD). These were chosen because they have proved to fit the data reasonably well at NICA energies [56, 57]. A short description of the models will be given in the following section, as well as a description of the parameters considered for the simulation process. For a complete review of the models, or a more complete explanation of the parameters, the references given should be consulted.

3.1 UrQMD event generator

UrQMD is a microscopic transport approach [58, 59]. The system evolves by a given EoS, which basically depends whether or not a nuclear potential is included. If no potential is considered, then the EoS will be in the CASCADE model. If a potential is considered (the only option available for UrQMD being a Skyrme potential), then the EoS will be in the hard Skyrme model [60]. The main difference is that the initial state will be constructed as a collection of point-like “nucleons” if the CASCADE model is chosen, and if the hard Skyrme model is chosen, the nucleons will be described by a superposition of Gaussian-shaped density distributions. Then the collisions are treated by a geometrical approach by means of their cross sections, as well as the decays by their branching ratios. Further interaction between the products is modeled by solving a set of coupled partial differential equations. This yields the time evolution of the phase space densities, restricted by conservation of energy, momentum and some quantum numbers.

Starting from version 3.3, an UrQMD+hydro approach was incorporated [61], in which the initial state is created as described above. This means that all nonequilibrium phases evolve using the usual UrQMD approach. Once a local equilibrium stage is reached, the system changes from a particle-based behaviour to a fluid-dynamical behaviour, in which the fluid is in perfect thermal equilibrium. This evolution continues until freeze-out, and the resulting hadron gas is then again described by the UrQMD approach. While this mode was not utilized in this work, it could be an interesting addition for future studies, as it incorporates a deconfinement phase.

In order to make the simulation work properly, there are a set of minimum parameters to be fixed, their values should be given as indicated in Ref. [62]. They provide information on

what type of collision process is to be simulated. A summary of the key parameters employed for this work is given as follows:

- **pro**: consists of two numbers, the mass number (A) and the number of protons (Z) of the projectile nucleus.
- **tar**: consists of two numbers, the mass number (A) and the number of protons (Z) of the target nucleus.
- **imp**: if the parameter b is positive ($b > 0$), it fixes the impact parameter of the collision at that specific value, in [fm] units. If the number is negative ($b < 0$), each event will choose an impact parameter in the range $(0, |b|)$.
- **ecm**: defines the center-of-mass-energy of the collision $\sqrt{s_{NN}}$, in [GeV] units.
- **nev**: is the total number of events to simulate.
- **tim**: consists of two numbers, *outtime* and *totime*. *Outtime* (ΔT) is an interval of time indicating that the information will be stored in the output files each ΔT , while *totime* indicates the total time at which the simulation stops. Both are given in [fm/c] units.
- **eos**: Defines the Equation of State for the calculation. The default mode (eos=0) is the CASCADE model. The Skyrme model can be activated (eos=1) but is limited to incident beam energies < 4 GeV/n.

Because of the energy range we are working with, only the default EoS (CASCADE mode) was considered. For the *outtime* and *totime* variables, it is unclear what would be the most appropriate values for the model. But it was clear from several tests done for this work that the two variables should have the same value, because if *outtime* was taken lower than *totime* then we would be writing the information of the particles at different time intervals (like taking a picture each ΔT), and thus considering more particles than what we actually expect on the final spectra. The value was fixed at 200 fm/c, just because most of the examples found in literature have this value.

There are, of course, a lot more parameters, but they will not be mentioned in this section as they were not employed. Once the values are given, we can choose what kind of information is to be recorded. UrQMD provides different files depending on what type of analysis is to be done,

- **f13 & f14** (standard output files): contains the information of all particles at a certain time-step.
- **f15** (collision history files): contains the information on all collisions, decays and similar events.
- **f16** (decay files): contains the information of all stable and unstable particles after the final timestep of a given event.

For the purpose of this work, it is only necessary to store the information of all the existing particles when the simulation ends (**f14** file). This file provides the information on the particles: space-time coordinates (t, x, y, z) , four-momentum (E, p_x, p_y, p_z) , mass, identity, isospin, charge, and information regarding the history of the particle (which is of no use for this particular analysis).

3.2 PHSD event generator

The Parton-Hadron-String Dynamics (PHSD) is also a microscopic transport model approach [63, 64]. As described in the Chapter 1, the collision starts with several nucleon scatterings. The interaction among partons is then modeled by color strings. Those strings can be pictured as quark-diquark pairs connected through the color flux tube. The strings can melt into a strongly-interacting QGP or fragment directly into hadrons. Next, the hadronization process takes place and the expansion to freeze-out is realized. This event generator can operate in two modes: the PHSD mode (which includes a partonic phase), and the HSD mode (which does not include a partonic phase).

The description of the partonic phase means that the correct degrees-of-freedom to study the problem are the partonic ones (quarks and gluons). And for the case of the PHSD model, it is realized in line with the Dynamical-Quasi-Particle Model (DQPM) in order to reproduce lattice QCD results for a QGP in thermodynamic equilibrium. So, in the QGP (partonic) phase, the time evolution is given by the off-shell transport equations with self-energies and cross-sections from the DQPM.

After the partonic phase (if activated), the system undergoes a dynamical hadronization, when the fireball expands. The probability for the partons to hadronize increases strongly close to the phase boundary. Then, the hadronization takes place based on covariant transition rates. The description of the hadronic degrees-of-freedom is given by the off-shell Hadron-String Dynamics (HSD) transport approach.

Just like in the UrQMD case, PHSD has an input file to which we provide the minimum necessary parameter values in order to make the simulation work with the required initial conditions. The name and description of the parameters are given according to the manual in Ref. [65],

- **MASSTA**: mass number (A) of the target nucleus.
- **MSTAPR**: number of protons (Z) of the target nucleus.
- **MASSPR**: mass number (A) of the projectile nucleus.
- **MSPRPR**: number of protons (Z) of the projectile nucleus.
- **ELAB**: energy per nucleon in the laboratory frame, in [GeV] units
- **BMIN**: minimal impact parameter, in [fm] units.
- **BMAX**: maximal impact parameter, in [fm] units
- **IBweight_MC**: If set =1, chooses a random number in the interval (BMIN,BMAX).
- **FINALT**: final time of calculation, in [fm/c] units.
- **NUM**: number of parallel events simulated.
- **ISUBS**: number of subsequent runs
- **IGLUE**: if set =1 (PHSD mode) a QGP phase is activated. If set =0 (HSD mode) there is no QGP phase.

Some additional parameters were either set to their default values or deemed unimportant for the current analysis, as they do not significantly affect the outcomes. However, certain parameters require further clarification regarding their description. Also, a brief explanation on the chosen parameters values for this work is given.

ELAB can be calculated from the center-of-mass-energy $\sqrt{s_{NN}}$ as follows. We can choose the z direction as the beam direction. Then, in the center-of-mass frame (CMS), the square of total energy of the system (per nucleon-nucleon collision) is simply

$$s \equiv c^2 p^{*\mu} p_{\mu}^* = (E_1^* + E_2^*)^2 = s_{NN}, \quad (3.1)$$

where $p^{*\mu} = p_1^{*\mu} + p_2^{*\mu}$ is the four-momentum in the CMS, and E_1^* , E_2^* the energy of each colliding nucleon. This is because in the CMS; $\vec{p}^* = \vec{p}_1^* + \vec{p}_2^* = 0$.

Now, the laboratory frame is defined in such a way that one of the colliding particles is at rest (target), and thus its four-momentum is given by $p_1^{\mu} = (m_1 c, 0, 0, 0)$. On the other hand, the incident particle (projectile) has a four-momentum $p_2^{\mu} = (\text{ELAB}/c, 0, 0, p_{\text{LAB}})$. So the invariant s is now

$$s = c^2 p^{\mu} p_{\mu} = m_1^2 c^4 + m_2^2 c^4 + 2m_1 c^2 \text{ELAB}, \quad (3.2)$$

where $p^{\mu} = p_1^{\mu} + p_2^{\mu}$.

Finally, from eqs. (3.1) and (3.2). By taking $m_1 = m_2 = m_N = 0.938 \text{ GeV}/c^2$ we get

$$\text{ELAB} = \frac{s_{NN}}{2m_N c^2} - 2m_N c^2. \quad (3.3)$$

IBweight_MC could be set to 0 if we wanted to work in a specific centrality class, but the value was set to 1 in order to study the minimum-bias case. This is also important for the values of **NUM** and **ISUBS**. The difference between PHSD and UrQMD (besides the model itself) is that UrQMD runs by an event-by-event basis, whereas PHSD runs by a parallel ensemble method. This basically means that for each **ISUBS**, there will be simultaneous **NUM** events. But this parallel ensemble has a direct consequence on the impact parameter chosen, because **IBweight_MC** chooses a different random value for the impact parameter (in the interval given) only for each different **ISUBS**. This means that each simultaneous event will have the same impact parameter value. Hence, in order to increase the number of randomly chosen impact parameter values, and thus make sure that the analysis is a minimum-bias one, the **NUM** should be taken considerably lower than **ISUBS**. A ratio of **NUM/ISUBS**=0.05 was considered low enough to work with, but it is important to mention that the computational time is increased mainly by **ISUBS**, and so the sample considered for this work using PHSD is considerably smaller than that of UrQMD.

As for the **FINALT**, the optimal values were obtained as the PHSD manual indicates, according to the equation

$$\text{FINALT} = 35 + \frac{170}{\sqrt{s_{NN}}[\text{GeV}]} [\text{fm}/c]. \quad (3.4)$$

Again, just as in the UrQMD case, PHSD stores different information in different files according to what type of analysis is to be done. We only mention that the output file considered for this analysis in the PHSD case contains essentially the same relevant information as that chosen for UrQMD.

Once the *output files* are obtained, the analysis can be done at the MC level, which is one of the goals in this work. Alternatively, if one wants to study the properties of a determined apparatus, a simulation through the detector's geometry is needed. This work does not pretend to give a complete analysis of this type, because the software is still under development and the detector itself is not yet completed. But a rather detailed analysis of this type is given with the hope to continue this work in the future.

Chapter 4

Monte Carlo and reconstructed data

This chapter presents the characteristics of the data obtained from simulations, according to the descriptions given in the previous chapter.

A general discussion on how the code for the analysis works is given below. Event and track selection criteria are discussed, as well as their associated efficiencies and contamination. Finally, we discuss the identification process, which is only applied to the reconstructed data.

4.1 Monte Carlo data sample (from UrQMD)

The data was generated by the version 3.4 of UrQMD (dated August 1st, 2014), and it is arranged in five different sets:

Au+Au collisions at: 4.5, 7.7, 9.2 & 11.5 GeV

Bi+Bi collisions at 9.2 GeV

For the Au+Au collisions, the data was generated with the help of the ICN cluster. As stated in the previous chapter, generating the data from UrQMD requires an input file, which assigns values to a minimal set of variables. The following list shows the values input values:

Energy:	4.5 GeV			7.7 GeV			9.2 GeV			11.5 GeV		
pro	197	79		pro	197	79	pro	197	79	pro	197	79
tar	197	79		tar	197	79	tar	197	79	tar	197	79
nev	500			nev	500		nev	500		nev	500	
imp	-20			imp	-20		imp	-20		imp	-20	
ecm	4.5			ecm	7.7		ecm	9.2		ecm	11.5	
tim	200	200		tim	200	200	tim	200	200	tim	200	200

The list shows how each data set was produced for the UrQMD Au+Au collisions at 4.5, 7.7, 9.2 and 11.5 GeV. Projectile, target, No. of events, impact parameter, center-of-mass energy and simulation time are shown in rows 2-7, respectively. For a detailed discussion and definitions of each variable, including the units, we refer to the Chapter 3.

The Bi+Bi collisions were simulated at the JINR, by the MPD collaboration. As a part of the testing, the detector performance is studied in different scenarios, so the collaboration is continuously providing new MC data sets focused on different lines of investigation. This particular data set was generated for general-purpose studies. The corresponding input file has the following values:

```

1      pro  209  83
2      tar  209  83
3      nev  500
4      imp  -16
5      ecm  9.2
6      tim  200  200
7      eos  0
8      rsd  11
9      stb  101
10     stb  102
11     stb  103
12     stb  104
13     stb  107
14     stb  109
15     stb  108
16     stb -108
17     stb  110
18     stb -110
19     stb  29
20     stb -29
21     stb  41
22     stb -41
23     stb  50
24     stb -50

```

The list shows how the UrQMD Bi+Bi collisions at 9.2 GeV was produced. Projectile, target, No. of events, impact parameter, center-of-mass energy, simulation time, and EoS are shown in rows 1-7, respectively. For a detailed discussion and definitions of each variable, including the units, we refer to the Chapter 3. Additional variables (stb) are used to prevent the decay of some resonances (rows 9-24).

Two major differences arise between the Au+Au and the Bi+Bi data sets: the first is related to the impact parameter (a difference of 4 fm), which is roughly half the radius of the nucleus under consideration, so it is unlikely that for a minimum-bias analysis this difference becomes relevant. The second concerns the parameter “stb” (optional special parameter). This parameter is defined by the UrQMD user manual as: “Set particle species with ityp¹ as stable particles. This parameter can be given multiple times, but no more than 20 times” [62]. This means that some unstable particles are forced to be stable throughout the simulation process² (such as stb 102 = η , stb 107 = η' , stb 109 = ϕ , etc.).

Once the MC data is generated, the simulation which transports the particles through the detector’s materials follows. During this process, the particles propagate, decay and interact

¹ityp is a label to distinguish each particle type, similar to a pdg code.

²They are considered stable for the collision process. Once the simulation of their interaction with the detector is running, they will no longer be considered as stable.

with the materials conforming the (sub)detectors. For the case of the Au+Au collisions (at all energies), the simulation was carried out by the Geant3 [66] software, and by the Geant4 [67] software for the Bi+Bi case. A total of 150,000 collision events were analyzed for each of the Au+Au cases, and a sample of 500,000 events was considered for the Bi+Bi collisions.

4.2 Monte Carlo data sample (from PHSD)

The data was generated by the version 5.2 of PHSD (March 23, 2023). It is arranged in five sets:

Au+Au collisions at: 4.5, 7.7, 9.2 & 11.5 GeV
 Bi+Bi collisions at 9.2 GeV

Here again, the data was generated with the help of the ICN cluster for the Au+Au case. The difference comes from two parameters: **ISUBS** and **NUM**. As discussed in Chapter 3, a ratio of **NUM/ISUBS**=0.05 was considered low enough to properly do the minimum-bias analysis. Because of the values chosen, a total of 5 jobs were sent for each energy (and mode, PHSD and HSD). This represents 10,000 events analyzed in this work for each case. The values of the parameters are:

Energy:	4.5 GeV	7.7 GeV	9.2 GeV	11.5 GeV
MASSTA	197	197	197	197
MSTAPR	79	79	79	79
MASSPR	197	197	197	197
MSPRPR	79	79	79	79
ELAB	8.918	29.728	43.241	68.620
BMIN	0.0	0.0	0.0	0.0
BMAX	20.0	20.0	20.0	20.0
IBweight_MC	1	1	1	1
FINALT	72.778	57.078	53.478	49.782
NUM	10	10	10	10
ISUBS	200	200	200	200
IGLUE	0 or 1	0 or 1	0 or 1	0 or 1

The list shows the parameters for the PHSD Au+Au collisions at 4.5, 7.7, 9.2 and 11.5 GeV. No. of neutrons of target, No. of protons of target, No. of neutrons of projectile, No. of protons of projectile, lab. energy, minimum and maximum impact parameter in minimum bias mode, calculation time, events, parallel events and QGP phase are indicated in rows 2-13, respectively. For a detailed discussion and definitions of each variable we refer to Chapter 3.

Evidently, for the PHSD event generator both the PHSD and HSD modes have been included. This means that actually there are 10 Au+Au data sets; 5 of them include a QGP phase (PHSD mode), and 5 who do not (HSD mode). Also the impact parameter was chosen to be the same as in the UrQMD case so that the three data sets have the same initial conditions (whenever possible).

Just as in the UrQMD case, the PHSD Bi+Bi collisions were produced by the MPD collaboration, also for general-purpose studies. Some values of the input parameters are listed

in the following:

1	MASSTA	209
2	MSTAPR	83
3	MASSPR	209
4	MSPRPR	83
5	ELAB	43.241
6	BMIN	0.0
7	BMAX	12.0
8	IBweight_MC	1
9	FINALT	>54.650
10	NUM	40
11	ISUBS	50
12	IGLUE	0 or 1

The list shows the parameters for the PHSD Bi+Bi collisions at 9.2 GeV. No. of neutrons of target, No. of protons of target, No. of neutrons of projectile, No. of protons of projectile, lab. energy, minimum and maximum impact parameter in minimum bias mode, calculation time, events, parallel events and QGP phase are indicated in rows 1-12, respectively. For a detailed discussion and definitions of each variable we refer to Chapter 3.

Values were obtained from the available information on the production of the data at the JINR cluster archives. Given that the input files were not found, limited information could be extracted. The freeze-out time indicates that some particles of the final spectra were fixed at a time as long as 54.650 fm/ c , so this provides a lower bound for the calculation time. It is not clear if the simulation is in PHSD or HSD mode, neither the PHSD version employed. The whole sample at the JINR cluster consists of 10 million events, but a reduced sample of 500,000 events was considered for this analysis to match that of UrQMD Bi+Bi.

No transport process was realized for the locally generated data in the PHSD case (Au+Au at all energies). But the process is, with some minor modifications, the same as will be described for the UrQMD case in the following section. The Bi+Bi collisions data has already undergone this process, which was done by the MPD collaboration within the Geant4 framework.

4.3 Transport process

The transport process was realized within the Geant3 (or Geant4) framework, which requires the collision data in an appropriate format to work. To do this, the raw output file from the event generators is read and transformed into a root file. This file is the input for the transport process, but it is also important to load the libraries containing the information of the geometry of the detector, fix the initial parameters, turn on/off the detectors to be employed, etc.

The results are employed in the reconstruction process, and even when this depends on the precise type of analysis to be done, most of the analyses (if not all) require knowledge of the identity of the particles produced, i.e. the identification process. In any case, information such as the lost energy, momentum, electric charge, time of flight, are among the most basic physical properties to be extracted from our detectors, either in the simulation or in a real experiment. The identification process will be described in some detail later in this chapter.

The analysis of the data of both the MC and transport process is stored in a single file once the whole process is finished. This will be necessary for obtaining the efficiencies. Once the transport process is finished, the reconstruction process is realized, which employs detector measurements and MC data to reconstruct the particle's tracks and store all measured physical quantities. Another important point is that this work was realized within the MPDroot³ framework [68], particularly the 23.03.23 version (March 23, 2023), which is not the latest version.

4.4 Kinematic relativistic in heavy-ions

In heavy-ion collision experiments, the transverse momentum is defined as the total momentum in the plane transverse to the beam direction. Typically the (x, y, z) directions are defined such that the z direction coincides with the beam direction. Thus, the transverse momentum will be given by

$$p_T = \sqrt{p_x^2 + p_y^2}. \quad (4.1)$$

In addition, there is a longitudinal component, $p_L = p_z$. Then we can define the rapidity (y) according to the equation

$$y = \frac{1}{2} \ln \left(\frac{E + p_L}{E - p_L} \right). \quad (4.2)$$

And finally, the pseudorapidity is defined by

$$\eta = \frac{1}{2} \ln \left(\frac{|\vec{p}| + p_L}{|\vec{p}| - p_L} \right) = \ln \left(\cot \frac{\theta}{2} \right), \quad (4.3)$$

where $|\vec{p}| = \sqrt{p_L^2 + p_T^2}$ is the total momentum and θ represents the angle in which the particle is emitted, this is easier to interpret and measure than the rapidity.

Rapidity and pseudorapidity are the same only in the limit of small mass, $m \rightarrow 0$. But we can connect their distributions by the equation

$$\frac{dN}{d\eta d^2p_T} = \frac{|\vec{p}|}{E} \frac{dN}{dy d^2p_T}. \quad (4.4)$$

Of particular interest is the region with $y \approx \eta \approx 0$, which is usually called the *midrapidity region*. The particles measured at midrapidity are either those created during the collision process or those who went through scattering processes, because otherwise their momenta would be unchanged.

4.5 Event selection

The *event selection* refers to the criteria imposed to either accept or reject a given collision event for the inclusion in the statistics. There are four variables which matter for the event selection process; three space coordinates and the impact parameter.

³As described in the webpage [68]; “MPDroot is the off-line software framework for simulation, reconstruction and physics analyses of the simulated or experimental data for MPD experiment”.

The impact parameter is directly related to the centrality, which indicates how central (how far apart are the centers of the colliding nucleus) the collision is. Each collision event will have a definite impact parameter, so by choosing specific interval values, some events will be rejected. Typically this is done if one is interested in dividing the data in centrality classes⁴. For this work, this criterion will be relevant later, when comparing to the experimental data. For the analysis in this chapter, no selection based on the centrality has been imposed.

With respect to the coordinates, they indicate the position (or vertex) at which the collision event has occurred. So, obviously each collision event will have specific coordinates (V_x, V_y, V_z) . Those values are given artificially when the simulation through the detector's geometry is carried out. This is because for the transport process, the whole collision event (simulated by the event generators) is taken point-like when the simulation begins (at $T_0 = 0$). Then, by default the transport process initiates with all the particles originating at the center of the detector (the interaction point). This implies that if no spreading of the initial position of the collision is given "by hand" (artificially) before the simulation begins, all particles of all events originate at coordinates $(0,0,0)$ in our detector's frame. But if one proceeds to a more realistic situation, a spreading should be considered. Typically a Gaussian smearing centered at the origin is applied, but the shape of the vertex distribution can be strongly energy-dependent, as observed experimentally.

In the present work, for the UrQMD locally reconstructed data, a smearing of $\pm(0.1, 0.1, 150)$ [cm] is considered. Exactly the same values were considered for the Bi+Bi collisions of the same event generator. For the PHSD Bi+Bi collisions, a smearing of $\pm(0.1, 0.1, 50)$ [cm] is considered. A limiting value of ± 150 cm in the z direction (beam direction) is necessary because that is the approximate size of one half of the TPC, as described in the Chapter 2. It is also the position at which the FFD is located. Figure 4.1 shows the z vertex distribution for Bi+Bi collisions in the UrQMD case. Similar distributions are observed for the rest of the UrQMD data. As we see, most of the distribution and the global maximum are located around the origin, but there are local maxima at $z = \pm 150$ cm, which represent collisions either with the edges of the TPC or the FFD. This does not occur for the Bi+Bi PHSD data, because the smearing does not permit that type of interaction. To avoid this issue, a cut in the V_z is realized for all the UrQMD data but not for the PHSD data.

For V_x and V_y , no cuts were imposed to any data set. This is because the value of 0.1 cm is small, so it does not generate any issue. In real experiments, a cut in the three vertices is almost always necessary. This is because in a real experiment, interaction with edges of the detectors (for the V_z vertex), and with the beam pipe (for the V_x and V_y vertices) is unavoidable, so appropriate cuts on the vertices are expected. One of the signals indicating the need for a vertex cut is a reduced multiplicity. The reason is that if the collision occurs at a considerable distance from the interaction point, close to the edges of the detector, some particles will be lost, because no detection can be made for a given solid angle.

⁴The impact parameter is not an experimentally measurable quantity, but the multiplicity is. The latter can be related to the impact parameter and so to the centrality of the collision. This is the proper experimental way to select a centrality class.

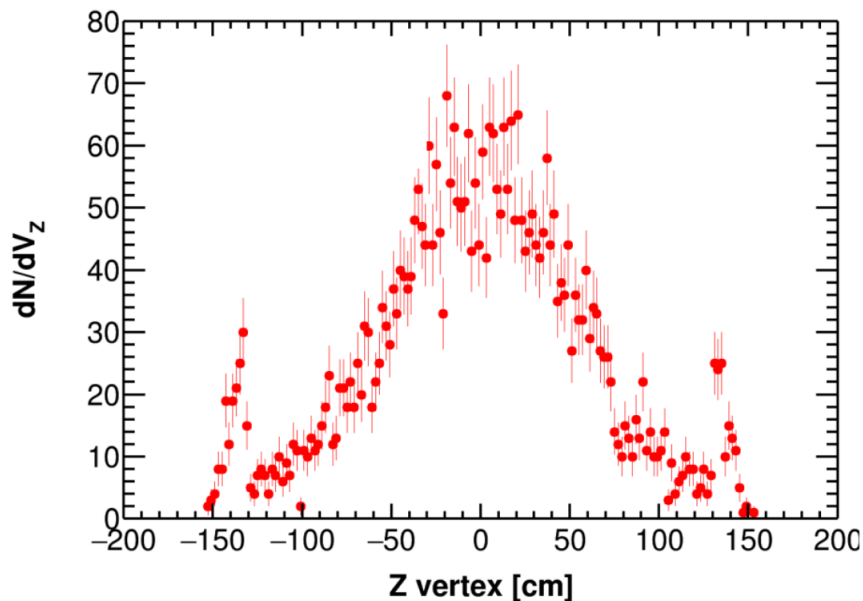


Figure 4.1: z coordinate distribution for the Bi+Bi collision vertices at 9.2 GeV with UrQMD. The peaks at ± 150 cm are attributed to the edges of the TPC or to the FFD. Similar results are observed for the rest of the UrQMD data. The PHSD Bi+Bi data have no peaks (beyond $z = 0$) because the smearing is limited to ± 50 cm.

4.6 Track selection

There is another type of selection criteria which does not select from events but from tracks, this is called the track selection. A track is defined as the path followed by a particle in its journey throughout the full detector’s geometry. In an experimental setup, we can only refer to those tracks which we can actually “visualize” (reconstruct by our tracking detectors). But with the MC data it is possible to track every particle’s trajectory and thus we could get a full picture of the trajectory of each particle in its passing through the detectors.

Generally speaking, there is a huge list of the variables which could be considered to make a track selection. The amount of them is usually determined by the resolution of the apparatus and the reconstruction algorithms. For this work, the variables employed are: Distance of Closest Approach (DCA), transverse momentum, rapidity (or pseudorapidity), number of hits (Nofh), and χ^2/Nofh .

The discussion about the DCA, the Nofh and χ^2/Nofh is left for the following section. This was done so that the concepts are better connected and thus give a broader picture on why they are necessary, and how to choose them adequately.

To make a basic spectra analysis in a given experimental setup, it is necessary to know the capabilities of the employed detectors. As discussed in the Chapter 2, the MPD’s TPC is limited to $p_T > 50$ MeV/ c and acceptance of $|\eta| < 1.2$, so the previous quantities represent kinematical restrictions of the system.

For the purposes of this work, a restriction of $p_T > 0.1$ GeV/ c has been implemented to avoid any issue. A rapidity bound $|y| < 0.5$ has also been imposed in order to be able to make a proper comparison to the data discussed in Chapter 1. And (only when necessary) a restriction of $|\eta| < 0.5$ has been considered to create the reason for the centrality classes is

that they are constructed as cuts of the multiplicity distribution. To define those cuts, we take a reference multiplicity, given by the primary charged particles at $|\eta| < 0.5$. As discussed previously, the multiplicity is related to the geometric parameters of the collision, such as the impact parameter, the number of participants etc. The result is that the centrality classes correspond to certain fractions of the cross section [70, 71].

4.7 Tracks efficiency and contamination

The purpose of track selection is to reduce as much as possible the artifacts, typically associated with wrong measurements and the identification process itself. At the end, one needs to find an equilibrium in reducing the quantity over quality, but without reducing it so that the uncertainties grow too large to arrive at any significant conclusion.

Concepts such as *efficiency* and *contamination* help us to identify the capabilities of our method and/or detectors and what could be the source of problems and uncertainties. This section is devoted to discussing the different sources of contamination associated with the reconstruction of the tracks, and to provide a guide when choosing a definite value as a selection criterion for those tracks.

Whenever we refer to a reconstructed track, it should be interpreted as the trajectory followed by a particle according to our detector. This trajectory is determined from the measurements of our tracking devices, such as the ionization produced inside the TPC. Those measurements are seen as “hit points”, which are joint according to a special algorithm in order to create different curves (tracks). Each curve represents, in the ideal case, a different measured particle. On the other hand, a Monte Carlo track (MC track) represents the theoretical solution of each particle’s trajectory. And thus, at the simulation level, this is to be interpreted as the “real” trajectory.

In order to study the efficiencies, we need a proper way to “track” the tracks. To this end, an association is made between the generated MC tracks and the reconstructed tracks. In the framework of the MPDroot, we can extract the information of all the reconstructed tracks from a branch of the root file called MpdGlobalTracks. The information of the MC is stored in a different branch, defined as MCtracks. Now the process consists of obtaining the identity (ID) of the reconstructed tracks, which is just a label put during the reconstruction process to each of the measured tracks. Then one can associate each reconstructed track with the “real track” (the MC track). It is important that not necessarily each MC track will be associated to a reconstructed track, some tracks will be “lost” because neither the reconstruction algorithm nor any detector is perfect. So, by “counting” how many tracks we really have (MC tracks) and comparing them to those which we can actually reconstruct (MpdGlobalTracks), we define our basic concept of efficiency of the reconstructed tracks. The advantage of this association procedure is that one obtains the real information of the reconstructed tracks because it is extracted directly from the MC. This means that every variable one measures will have the real value (that from the MC), starting with the identity of the particle (its pdg code) corresponding to a particular track. A simple example of the code is as follows:

```

1 fTMCTracks = event.fMCTrack; // MC tracks of the event
2 Int_t nmctracks=fTMCTracks->GetEntriesFast(); // No. of MC tracks
3
4 fTDstEvent = event.fMPDEvent;
```

```

5 fTMpdGlobalTracks = event.fMPDEvent->GetGlobalTracks(); // Global rec.
   tracks of the event
6 TClonesArray *MpdGlobalTracks = (TClonesArray*)fTDstEvent->GetGlobalTracks
   ();
7 Int_t ntracks=fTMpdGlobalTracks->GetEntriesFast(); // No. of rec. tracks
8
9 for (Int_t i = 0; i < nmctracks; i++){ // loop over MC
10   MpdMCTrack *MCTrack = (MpdMCTrack*) fTMCTracks->UncheckedAt(i);
11   Double_t ptmc = MCTrack->GetPt();
12   Int_t pdgmc = MCTrack->GetPdgCode();
13   }
14
15 for (Int_t i = 0; i < ntracks; i++){ // loop reconstructed tracks
16   MpdTrack *track = (MpdTrack*)fTMpdGlobalTracks->UncheckedAt(i);
17   Int_t ID = track->GetID();
18   MpdMCTrack *MCTrack = (MpdMCTrack*) fTMCTracks->UncheckedAt(ID);
19   Double_t ptmc = MCTrack->GetPt();
20   Int_t pdgmc = MCTrack->GetPdgCode();
21   }

```

This macro mainly consist of two loops which run over the MC and reconstructed tracks. All the information corresponding to the MC should then be provided within the MC loop and the Associated Monte Carlo (AMC) is inserted inside the reconstructed tracks loop. A comparison between the MC and reconstruction then tell us how our original data is being transferred from the raw MC to the reconstruction in the idealistic scenario of our detector's measurements.

There will be some errors associated with the reconstruction algorithm and some with the detector's resolution. Those associated with the detector will be studied in the next chapter. Two main sources of contamination at the reconstruction level have been studied in this work: that of the repeated tracks and of the secondary tracks.

4.7.1 Repeated tracks

One particular effect (which in reality is a conglomerate of different effects) is that of the repeated tracks. Repeated tracks (RT) are defined in this work as tracks with the same ID for the same event. This set is divided in two types for this analysis: one corresponding to the Splitted Tracks (ST) and the other to the Ghost Tracks (GT). To distinguish properly between these two sets, it is necessary to mention that the TPC consist of 52 layers in the radial direction in which a hit (point of a track) can occur. This means that a given track can be (at most) reconstructed with 52 hits. "Ghost tracks" are those repeated tracks which, adding up their number of hits, surpass this limit of 52 hits. Let us assume that there are N repeated tracks RT_1, \dots, RT_N with h_1, \dots, h_N number of hits respectively. If the condition $h_1 + \dots + h_N > 52$ is met, those tracks (minus one) are labeled as ghost tracks. This means that there are some points shared between ghost tracks, which should not happen in the case of splitted tracks. However, even if this is true for both the ST and GT, the criterion only works as a lower bound for the real number of GT, because there can exist repeated tracks sharing some points and still having less than 52 hit points. A precise counting for the GT has not been realized for this work because no appropriate algorithm to characterize them has been invented yet. The important point is that the RT encloses both the ST and GT effects.

The discussion is clearer if we look at the distribution of the number of hits per number of tracks in Figure 4.2a.

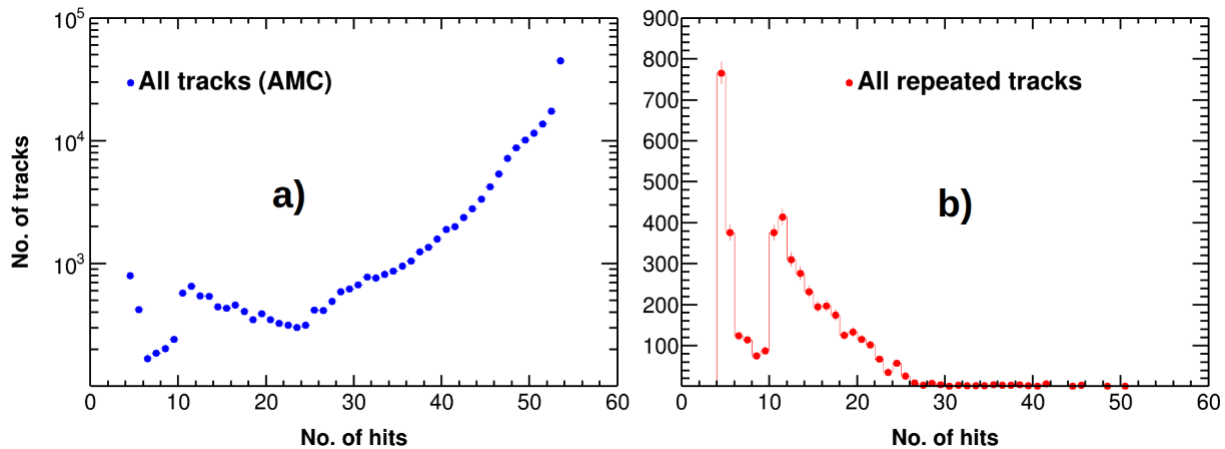


Figure 4.2: Number of hits distribution for UrQMD Bi+Bi Collisions at 9.2 GeV. a) Distribution for all the Associated Monte Carlo tracks. b) Distribution of the repeated tracks only. The distributions for the PHSD Bi+Bi collisions are similar.

Figure 4.2 (left) shows that most of the tracks have a high hit-count, but we also observe two local maxima; at the lowest value (~ 4) and at about 11. If we have repeated tracks, there will only (always) be one considered as the “real” track, while the rest will be either splitted or ghost tracks. In order to distinguish which of the RT will be considered as the real track, we argue that a track is better reconstructed when more points are used, and so the real track is defined as that of the RT with the maximal number of hits. For this reason, from here and unless specified, whenever a discussion about the RT is done, it should be keep in mind that the real track is not a part of the RT. To better justify the definition, the distribution of the number of hits per RT (no real track is considered) is shown in Figure 4.2 (right). If the real track was taken arbitrarily from each RT, the distribution would look similar to that of Figure 4.2a. This is of great importance, because if we look for the Nofh distribution of each data set, we can choose a value such that most of the RT are cut off. This represents a selection criterion over the number of hits.

Another variable of interest is obtained by dividing each tracks’ χ^2 by its number of hits (χ^2/Nofh). The χ^2 can be employed to analyze if the measurements are within reason of our expected values. So, this quantity is calculated while the reconstruction algorithm is in process, with the aim to analyze the quality of those reconstructed tracks. But it turned out that the overall effect of a cut on the number of hits, as discussed in the previous paragraph, and this variable are similar because they are closely related.

4.7.2 Primary and secondary tracks

As discussed in this section, we can identify the main stages of the analysis as: the simulation of the collisions via the MC event generator, then the simulation of the interaction of the generated particles with the detectors, the reconstruction of the tracks and the identification process (if implemented). All the particles produced by the event generators at the interaction point, and reconstructed by the MPD software are defined as *primary particles*. The rest of

the particles, either coming from decays or interactions with the materials of the detectors or any other physical process are defined as *secondary particles*.

This makes it easy to distinguish between primary and secondary tracks when information of the MC is provided. In the MPDroot, a primary selection can be done by means of the motherID of the particle, which is just a label to distinguish whether the particle comes from the generated MC data or not. Nevertheless, in a real experimental situation we cannot do this: the characterization is not that straightforward, so a new variable is needed to account for the primary tracks. To do a proper selection, first we have to know the position of the primary vertex, this is the position where the collision occurs. The position of this vertex is determined by an extrapolation of all the tracks produced by a single collision event. Then we can individually extrapolate each particle's track to the nearest position to this primary vertex; this is called the Distance of Closest Approach (DCA). A DCA cut for each track should, in principle, make a reasonable distinction of primary from secondary tracks. This will be important, for example, in centrality studies, because the particles of interest are the primaries, and thus an adequate primary vertex and track reconstruction is fundamental. Normally, a DCA is expressed as a radial distance (typically of the order ~ 1 cm) between the nearest point of the track to the primary vertex.

The values of the track selection criteria obtained for each data set will be discussed in the next chapter. In the following section, a discussion of the particle identification process is given, this is essential to obtain any results when analyzing real data. Then again, the results and the methodology are preliminary. This will not necessarily be the final form taken when the MPD is commissioned, because the software is still under development.

4.8 Particle identification

Any experimental setup in high energy physics is based on the notion that particles traveling through matter will interact if the appropriate conditions are met. There exist a great variety of possible interactions (usually ionization), but the goal in any experiment is to isolate as much as possible this type of interactions to only a reduced amount, to be able to arrive at a significant conclusion.

In Chapter 2, the different detectors of the MPD apparatus were discussed, and a brief overview on how the apparatus works was given. The idea in this section is to focus on the identification process itself rather than giving a precise description on the physical processes involved, the theoretical and experimental concepts were adopted mainly from the Refs [72, 73].

There are three key measurements to be done in the apparatus: the momentum, the stopping power or energy loss dE/dx , and the time-of-flight of the particle. The first quantity is indirectly measured by the bending of the particles trajectory given that there is a uniform magnetic field (a magnetic field of 0.5T is applied in the z direction when the Geant4 simulation starts). The second quantity is measured by the ionization in the TPC. And the third one is measured by the TOF system. The time is not directly reported in this work, but it is used in combination with the momentum measurements in order to obtain the mass squared (m^2) of the particle.

The identification process itself is realized by a C++ class called “mpdpid”, created by the MPD collaboration. The process is greatly simplified with the introduction of this class. To make it work properly, one needs to fix the values of seven variables; σ_M , σ_E , E , koef,

Generator, Tracking and “string of particles”. They are defined in the following way:

- σ_M : Number of standard deviations from the average mass-squared.
- σ_E : Number of standard deviations from the average energy loss per length $\langle dE/dx \rangle$.
- E : Energy of the collision in the center-of-mass reference.
- *koef*: Scale coefficient of dE/dx , should be used if dE/dx has been multiplied by this value during the reconstruction process.
- *Generator*: The model which has been used in the simulation (for example, URQMD or PHSD).
- *Tracking*: It can be “HP” (Hit Producer), “CF” (Cluster Finder MLEM) and “CFHM” (Cluster Finder MLEM + HEED).
- “string of particles”: String of particles which are used in n -sigma method (this means, “which particles are we interested in?”).

The first two quantities will be clarified later. The *koef* is needed depending on the tracking system employed. It consist of different algorithms to obtain each tracks’ dE/dx . Both HP and CF are old versions, which calculate the dE/dx in some arbitrary units, and thus the *koef* was introduced to work as a correction factor. The most recent version CFHM does not need any correction factor and *koef* should be set to 1 if this tracking is employed. The last variable specifies to which particle(s) the n -sigma method should be applied (this method will be explained later, together with the σ_M and σ_E).

The basic idea with this class is to create a probability vector with the input information from the detectors. Each entry represents the probability of either being a kaon, a proton or a pion (“string of particles”), and is calculated by adding up the individual probabilities in a Bayesian approach. The entries of the probability vector can be stored if enough information is provided, either with only the information of the TPC or with both the TPC and TOF. In principle, this would mean that there exist two possibilities for the identification of the particles, but additional identification methods can be constructed by combining the two previous possibilities. For this work, one additional option was created, so three modes in which the identification can be made are:

- TPC (PID mode 0): Uses only dE/dx and momentum measurements (only TPC measurements).
- TPC+TOF (PID mode 1): Uses a combination of TPC and TOF measurements. TPC only measurements are discarded.
- TPC+TOF modified (PID mode2): Uses the TPC only at low p values if the TPC+TOF cannot be used.

The first two methods have already been discussed, but the third method was introduced to avoid the so called *mismatch effect*. The problem arises when one uses both the TPC and TOF, particularly at low p values. This is produced because when combining the information

of the TPC and TOF, the tracks reconstructed by the TPC should be matched with the measurements of the TOF, but it can happen that some tracks are wrongly overlapped to those measurements. In that case, the probability vector does not store the information of the track, and so it is lost. The modification is that when is not possible to use the TPC+TOF method, and if the momentum is low enough, then the probability vector can be filled only with the TPC information if possible. This second method consistently proved to be the most efficient of the three PID modes, as shown in Figure 4.3. It can be observed that PID mode 1 and 2 are similar at almost all values, except for low p values. In fact there are no protons identified in the first bin with the PID mode 1, and the uncertainty in the second bin is greatly reduced with the PID mode 2. A similar situation was observed at all energies for protons, for the kaons, and the pions were almost unaffected by the PID mode.

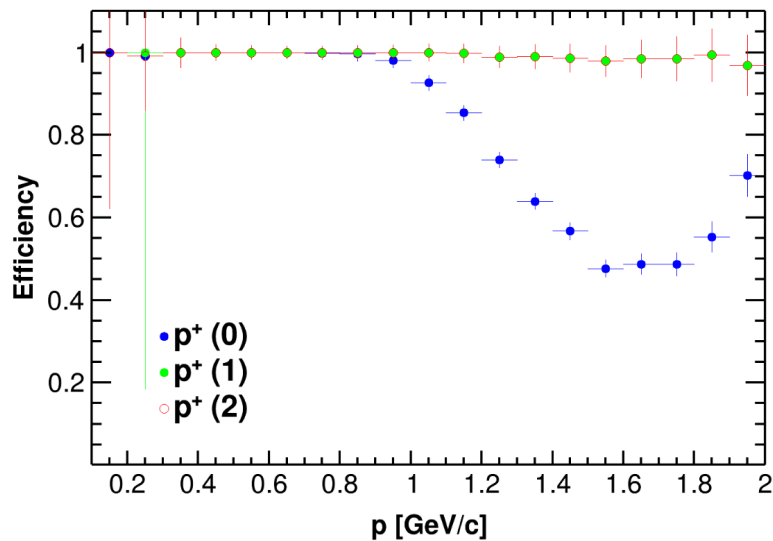


Figure 4.3: Reconstruction efficiency of protons vs. momentum for Bi+Bi collisions from UrQMD. Three identification modes are shown: TPC only (0), TPC+TOF (1) and TPC+TOF modified (2). The only difference between (1) and (2) is at low momentum.

A simplified version of the code which makes the identification process is shown below:

```

1 pid = new MpdPid(2.0, 2.0, 9.2, 1.0, "URQMD", "CFHM", "pikapr"); //
  mpdpid class (sigM,sigE,E,koef,Generator,Tracking,"string")
2 const Int_t PIDmode = 2;
3 Double_t fProbCut = 60.e-02; // cut on probability
4 Double_t toflim=40.e-02; // TPC only (if needed) for pT<
5 Bool_t ret, retTPC; // activated only if a probability vector is filled
6 Bool_t pidFlag; // activated if a TOF measurement is done
7
8 // obtaining info from branches, etc...
9
10 for (Int_t i = 0; i < ntracks; i++){ // loop reconstructed tracks
11 MpdTrack *track = (MpdTrack*)fTMpdGlobalTracks->UncheckedAt(i);
12 Double_t pt = track->GetPt();
13 Int_t charge = track->GetCharge();
14 Double_t px = track->GetPx(); Double_t py = track->GetPy(); Double_t pz
  = track->GetPz();
15 Double_t mpdP = TMath::Sqrt(px*px + py*py + pz*pz);

```

```

16 Double_t dedx = track->GetdEdXTPC();
17 pt = TMath::Abs(pt); // because of the charge pT can be <0
18
19 // cuts are introduced here
20
21 if (mapTof.count(i) > 0)
22     {
23         m2 = ((MpdTofMatchingData*)tofMatches->UncheckedAt(mapTof[i]))->
24         GetMass2();
25         pidFlag = kTRUE; // succesful TOF measurement
26     }
27
28 // ...
29
30 if (PIDmode==0) retTPC=pid->FillProbs(mpdP,dedx,charge); // TPC only
31 else if (PIDmode==1) { // TPC+TOF
32     if (pidFlag) ret = pid->FillProbs(mpdP,dedx,m2,charge);
33 }
34 else if (PIDmode==2) { // TPC+TOF modified
35     if (pidFlag) {
36         ret = pid->FillProbs(mpdP,dedx,m2,charge);
37         if (!ret && mpdP < toflim) retTPC = pid->FillProbs(mpdP,dedx,
38         charge);
39     }
40 } else continue; // Wrong PIDmode expression
41
42 Double_t pion = pid->GetProbPi(); // probability of bein pion
43 Double_t proton = pid->GetProbPr(); // probability of bein proton
44 Double_t kaon = pid->GetProbKa(); // probability of bein Kaon
45 Int_t maxloca = 0;
46 Double_t Probs[] = {pion,kaon,proton};
47 Double_t maxprob = TMath::MaxElement(3, Probs); // where is the maximum?
48 maxloca = TMath::LocMax(3, Probs);
49
50 if (maxprob<fProbCut) continue; // identified only if probability of
51 being X > fProbCut
52 if (charge > 0) // could be either positive or negative or no
53 distinction
54     {
55         // fill histograms
56     }
57 // ...
58 }

```

Boolean operators such as `ret`, `retTPC` are introduced for further Quality Assurance tests, which account for the identification efficiency and contamination, which will be discussed in the next chapter. Once the identification method is chosen, the algorithm evaluates for each track what is the most likely particle associated to it, and if it satisfies a minimum probability criterion, then it contributes to the corresponding histogram. This probability cut can also be considered as a track cut, but no considerable differences were observed for values $> 60\%$ and thus this value was fixed.

The `mpdpid` class relies on a Bethe-Bloch like formula, which describes how different types of particles lose energy while traversing through different materials. This class makes use of a modified version of the formula, due to Allison & Cobb [74]. A reference (average) energy

loss per unit length is calculated from a particular simulation, and is parameterized by

$$\left\langle \frac{dE}{dx} \right\rangle = \frac{p_1}{\beta^{p_4}} \left\{ p_2 + \beta^{p_4} - \ln \left[p_3 + \left(\frac{1}{\beta\gamma} \right)^{p_5} \right] \right\}, \quad (4.5)$$

where $\beta^2 = p^2/(m^2c^2 + p^2)$, γ is the Lorentz factor, and p_i are free fitting parameters.

A fit for the UrQMD Au+Au collisions at $\sqrt{s_{NN}} = 11.5$ GeV is shown in Figure 4.4 (solid black curves). Pions are shown in red, kaons in green and protons in blue. The identification at low p_T can be realized by the TPC alone, but at approximately 0.7 GeV/c an overlapping of the dE/dx of kaons and pions occurs, whereas an overlap of protons, kaons and pions is observed at ~ 1.3 GeV/c. This is why the PID mode 0 is not particularly well suited for protons (and kaons) at high p_T , as Figure 4.3 shows.

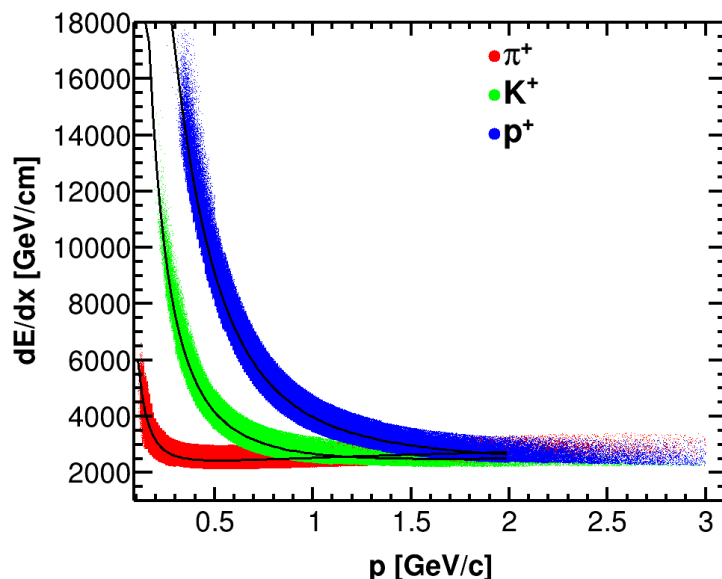


Figure 4.4: Energy loss per unit of distance vs. momentum for positively charged particles at $|y| < 0.5$ for Au+Au collisions at $\sqrt{s_{NN}} = 11.5$ GeV (UrQMD). Colored symbols represent values measured by the TPC and the black lines show the predicted energy loss according to the Allison-Cobb model [74].

The idea of introducing the TOF system in the MPD detector is to improve data at high p_T . When this system is implemented, by acquiring the information on the time taken for the particle in traversing the TOF, their separation distance, and together with the momentum of the particles, the value m^2 is extracted. This is easily derived from the relativistic energy relation

$$\gamma^2 m^2 c^4 = E^2 = p^2 c^2 + m^2 c^4, \quad (4.6)$$

where $1/\gamma^2 = 1 - v^2/c^2$.

If L is the distance traveled by the particle, with a time of flight T , then $v = L/T$ its velocity. We finally obtain

$$m^2 c^2 = p^2 \left(\frac{c^2 T^2}{L^2} - 1 \right). \quad (4.7)$$

Figure 4.5 shows the p vs. m^2 distributions for all positively charged particles. Color codes are the same as the Figure 4.3. Observe that $m^2 < 0$ occurs. This would naively lead us to the conclusion that the particle is traveling at speeds higher than the speed of light, because $L/T = v$ is the velocity of the particle. Then the only way of obtaining a negative m^2 is if $c < v$. But these cases are just artifacts, consequence of signals from different tracks being triggered and incorrectly matched. It is important to keep on mind that the detectors are not perfect. We should get rid of these signals as much as possible when analyzing real data, or dire consequences would be obtained by making precipitated claims.

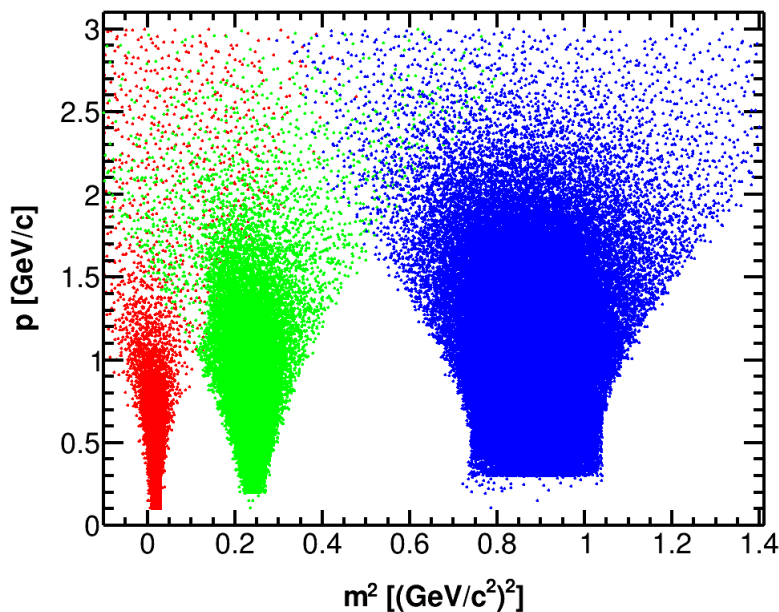


Figure 4.5: Reconstructed momentum vs. mass-squared distribution for UrQMD Au+Au at 11.5 GeV. The calculation is done by combining TPC and TOF information. Red, green and blue symbols represent pions, kaons and protons, respectively.

The last step of the identification then consists of comparing the reference values $\langle dE/dx \rangle$ and $\langle m^2 \rangle$ to the individual dE/dx and m^2 for each track. Next, the `mpdpid` class makes use of the σ_M and σ_E variables, which tells the algorithm how many standard deviations from that reference value should be taken in consideration for assigning a probability of being one type of the particles of interest. This is called the n -sigma method.

4.9 Identification efficiency and contamination

Once the identification process is realized, we can calculate how efficient the process is. To achieve this, it is necessary to define what efficiency and contamination mean in this context, which are concepts different from the tracks' efficiency and contamination.

As stated in the previous section, in order to identify the particles we make use of different variables which help us to improve the quality of the reconstructed tracks and diminish the background and errors, such as Number of hits, DCA, etc. Once the selection process (all cuts) is realized, by applying the Monte Carlo Association method previously discussed, we

can obtain each track's pdg code from the MC (which tells us the real identity of the particle, not the one assigned by our algorithm with the detector's information).

Then, we can define:

- *All tracks selected* (TS): All reconstructed tracks satisfying the selection criteria, whose identity is determined by the real (MC) pdg code.
- *True positives* (TP): All reconstructed tracks satisfying the selection criteria, whose assigned identity (determined by the identification process) coincides with that of the MC.
- *False positives* (FP): All reconstructed tracks satisfying the selection criteria, whose assigned identity (determined by the identification process) does not coincides with that of the MC.

By employing those definitions, we can calculate the efficiency ϵ_{id} and contamination δ_{id} of the identification process as

$$\epsilon_{id} = \frac{TP}{TS} , \quad (4.8a)$$

$$\delta_{id} = \frac{FP}{TS} . \quad (4.8b)$$

Figure 4.6 shows the efficiency and contamination for UrQMD Au+Au collisions. As it can be observed, the overall behavior is similar for all energies. Given the identification method employed, the drop in the efficiency can be explained by looking at Figure 4.5: the mass distributions for the kaons starts to overlap that of the pions at around 1 GeV/c, where the efficiency for the kaons drops. As the momentum increases, the kaon and pion distributions are more or less merged, so the pions distribution also starts to drop at around 1.5 GeV/c. For the protons, the efficiency remains almost constant over the whole interval, but at low momentum the efficiency is relatively low due to two main reasons: from Figure 4.4 we can observe that there are hardly any low momentum proton detected by the TOF, probably because most of the tracks have been lost due to the mismatch effect. On the other hand, as can be observed in Figure 4.4, the TPC alone detects few low momentum protons, thus the efficiency drops and the errors increase. All the efficiencies are qualitatively similar to those reported by the MPD collaboration [52]. Also, the efficiency (contamination) for the negatively charged particles is qualitatively and quantitatively similar to that of the positively charged particles, with the only noticeable difference being in the antiproton case, where the statistics is low and so the relative errors are larger.

The results for the whole analysis presented in this chapter and the main outcome of this work will be discussed in the next chapter.

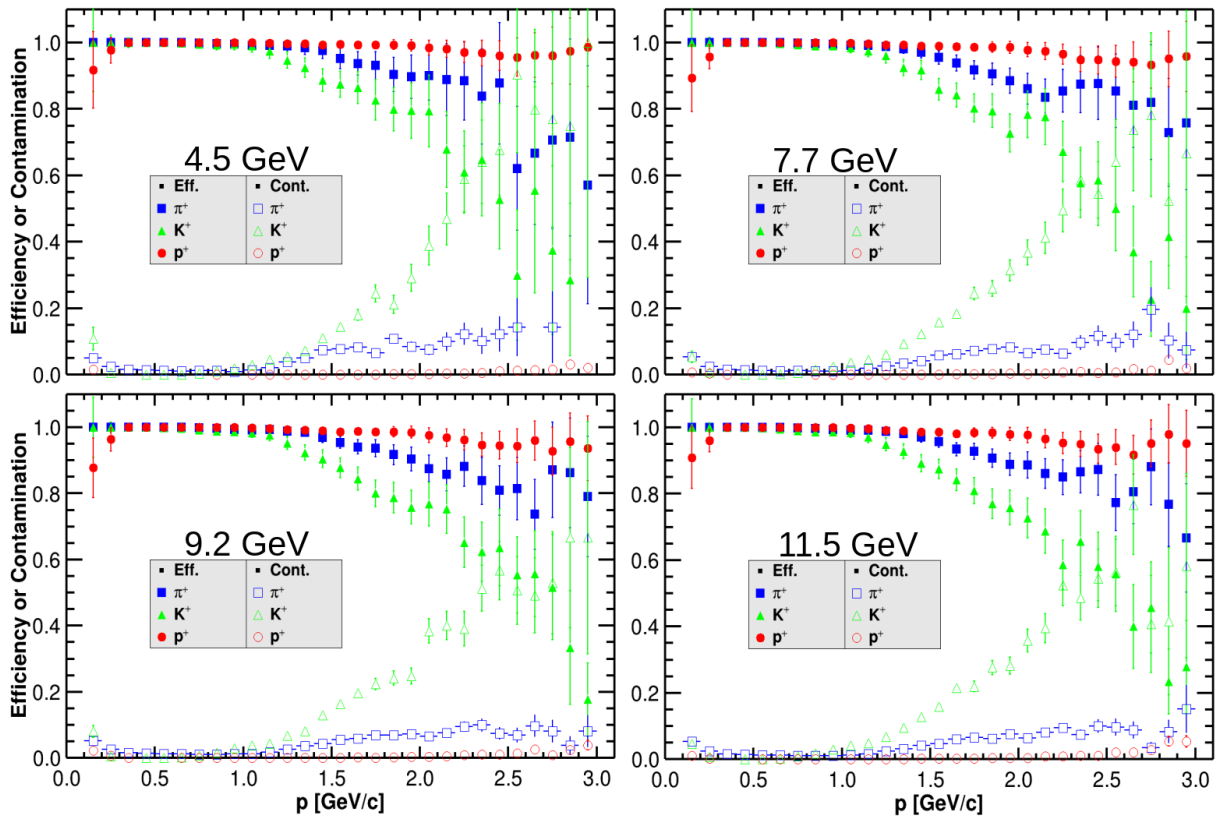


Figure 4.6: efficiency and contamination for the UrQMD Au+Au collisions at all energies. Similar results are obtained for the negative charged particles.

Chapter 5

Results and discussion of the Monte Carlo data

This chapter focuses on presenting and discussing the transverse momentum distributions for both the generated MC and reconstructed data with the MPD detector. Additionally, it delves into the results of the track analysis, including the corresponding efficiencies and contamination for the reconstructed data. All of these analyses were conducted within the framework of MPDroot [68].

With the obtained distributions, the integrated yield ratios are calculated for some special cases and compared to real data. The distributions are fitted and the evolution of the meson and baryon production is studied. This could provide relevant physical information related to their production mechanisms.

5.1 Event and track selection analysis

Table 5.1 shows a summary of the results for the Bi+Bi collisions when no primary or secondary selection is imposed, only the basic kinematic restrictions are applied; $p_T > 0.1$ GeV/c and $|y| > 0.5$. The study was done only for the Bi+Bi collisions, both with UrQMD and PHSD, but similar results are expected for the Au+Au collisions, because their mass numbers are close to each other, 208 for the former, 197 for the latter. The quantities are the total number of tracks (ToT) coming from: the MC, AMC, RT and GT. Similar results are observed for both event generators. The number in parenthesis in the third column indicates the efficiency of the reconstructed tracks when comparing to the MC tracks, it means that about 80% of the tracks are lost if no selection over primary or secondary tracks is done. Regarding the total number of reconstructed tracks, the fourth column indicates that about 3% are repeated tracks, whereas at least 15% of those repeated tracks are ghost tracks.

From Table 5.2, where a selection of primary tracks is done via the motherID of the tracks (meaning that we can be sure that all tracks are in fact primary tracks), we can observe that the reconstruction efficiency is excellent, because only about 6% of the primary tracks got lost in the process. The total number of repeated tracks stays about the same as in the previous case, and the ghost track's lower bound is only reduced to $\sim 13\%$. By combining the information of Tables 5.1 and 5.2, we can conclude that most of the MC tracks come from secondary particles: $\sim 90\%$ for the UrQMD case, and $\sim 80\%$ for PHSD.

Data	ToT MC	ToT AMC	ToT RT	ToT GT
UrQMD	1873881	319659 ($\sim 17\%$)	9617 ($\sim 3\%$)	1514 ($\sim 15\%$)
PHSD	2255585	508396 ($\sim 23\%$)	16596 ($\sim 3\%$)	2494 ($\sim 15\%$)

Table 5.1: Number of repeated tracks in the Bi+Bi samples without any selection of either primary or secondary tracks. Columns from left to right: event generator, Total number of tracks (ToT) from the Monte Carlo, from the Associated Monte Carlo, from the Repeated tracks, and for the Ghost tracks. Each number in parentheses represents the percentage of the sample with respect to the quantity on its left column, i.e. (ToT AMC)/(ToT MC), (ToT RT)/(ToT AMC), (ToT GT)/(ToT RT), respectively.

Data	ToT MC	ToT AMC	ToT RT	ToT GT
UrQMD	166730	156659 ($\sim 94\%$)	4459 ($\sim 3\%$)	604 ($\sim 13\%$)
PHSD	420065	396702 ($\sim 94\%$)	11678 ($\sim 3\%$)	1489 ($\sim 13\%$)

Table 5.2: Number of repeated tracks in the Bi+Bi samples of only primary tracks via the motherID of the track. Columns from left to right: event generator, Total number of tracks (ToT) from the Monte Carlo, from the Associated Monte Carlo, from the Repeated tracks, and for the Ghost tracks. Each number in parentheses represents the percentage of the sample with respect to the quantity on its left column (same as in Table 5.1).

In Table 5.3, a DCA cut is implemented to make the selection of primary tracks. The results appear rather strange for the case of UrQMD, because the efficiency of reconstructed tracks is about 137%. This means that there should be a source of enormous contamination, but if we look into the numbers of repeated tracks we can observe that they represent about 1% of the sample. Then we cannot explain this contamination in terms of the repeated tracks. Most likely the source of contamination should come from the secondary tracks. For the PHSD case we observe that even when the DCA cut reduces the reconstruction efficiency to about 88%, the contamination due to repeated tracks is also reduced down to 1% and the lower bound for ghost tracks is reduced even more.

Data	ToT MC	ToT AMC	ToT RT	ToT GT
UrQMD	166730	228243 ($\sim 137\%$)	2836 ($\sim 1\%$)	5 ($\sim 0.2\%$)
PHSD	420065	368689 ($\sim 88\%$)	4920 ($\sim 1\%$)	12 ($\sim 0.2\%$)

Table 5.3: Number of repeated tracks in the Bi+Bi samples of only primary tracks via a $DCA < 1$ cm. Columns from left to right: event generator, Total number of tracks (ToT) from the Monte Carlo, from the Associated Monte Carlo, from the Repeated tracks, and for the Ghost tracks. Each number in parentheses represents the percentage of the sample with respect to the quantity on its left column (same as in Table 5.1).

Table 5.4 shows that a cut over the number of hits (additional to the DCA cut) does in fact reduce the number repeated tracks and ghost tracks, but the DCA cut by itself makes a better job in reducing this number. Probably the explanation is that the repeated tracks usually have a reduced number of hits. This leads us to extrapolate a curve that, in its DCA,

will be too far from the primary vertex. So, a cut over the DCA will take most of the RT off.

Data	ToT MC	ToT AMC	ToT RT	ToT GT
UrQMD	166730	224092 ($\sim 134\%$)	2078 ($\sim 1\%$)	1 ($\sim 0\%$)
PHSD	420065	361956 ($\sim 86\%$)	3576 ($\sim 1\%$)	1 ($\sim 0\%$)

Table 5.4: This table shows the number of repeated tracks in a sample of only primary tracks via a $DCA < 1$ cm plus a cut on the number of hits > 30 . Columns represent, from left to right: request No., Total number of tracks (ToT) from the Monte Carlo, from the Associated Monte Carlo, from the Repeated tracks, and for the Ghost tracks. Each number in parentheses represents the percentage of the sample with respect to the quantity on its left column (same as in Table 5.1).

Tables 5.5-5.7 summarize the results for the primary and secondary tracks, and together with the previous tables they lead to a better understanding of the whole analysis.

Table 5.5 introduces two new quantities coming from the reconstruction: the number of primary tracks (PrimT) and secondary tracks (SecT). It is observed that without making any selection of the primary or secondary tracks, about half of the reconstructed tracks come from primary tracks, and half from secondary tracks in the UrQMD simulation. A considerable difference is observed for the PHSD data, in which about 80% of the tracks consist of primary tracks and 20% of secondary tracks.

Data	ToT MC	ToT AMC	ToT PrimT	ToT SecT
UrQMD	1873881	319659 ($\sim 17\%$)	156659 ($\sim 49\%$)	163000 ($\sim 51\%$)
PHSD	2255585	508396 ($\sim 23\%$)	396702 ($\sim 78\%$)	111694 ($\sim 22\%$)

Table 5.5: Number of primary and secondary tracks with only basic cuts. Columns from left to right: event generator, Total number of tracks (ToT) from the Monte Carlo, from the Associated Monte Carlo, from the Primary tracks, and from Secondary tracks. The numbers in parentheses in columns 4 and 5 represent the percentage of the sample with respect to the total number of AMC tracks, i.e. $(ToT\ PrimT)/(ToT\ AMC)$ and $(ToT\ SecT)/(ToT\ AMC)$, respectively.

In Table 5.6 a cut on the $DCA < 1$ cm is applied to the tracks. The results for the UrQMD case shows that the DCA cut does not considerably reduce the contamination due to secondary tracks, they represent up to $\sim 40\%$ of the tracks. This means that the 137% efficiency in track reconstruction of primary tracks has quite a big error. As for the PHSD simulation, the primary tracks represents about 90% of the reconstructed tracks, while there is a contamination of $\sim 10\%$ of secondary tracks.

Next, Table 5.7 shows an even more restrictive cut over the DCA (< 0.5 cm). The effect is an overall reduction in the reconstruction efficiency for both event generators of about 20-30%. In the case of the UrQMD data, the percentage of primary and secondary tracks stays about the same as in the $DCA < 1$ cm case. But for the case of PHSD, a little improvement is observed, less contamination from secondary particles on the condition of losing about 20% of the tracks.

Another interesting result is presented in Table 5.8: it shows how many tracks corresponding to a particular particle species ($X = \pi^\pm$ or K^\pm or p^\pm) are there in the total reconstructed tracks which are primary tracks (motherID criterion). Then the new quantities shown are: the

Data	ToT MC	ToT AMC	ToT PrimT	ToT SecT
UrQMD	166730	228243 ($\sim 137\%$)	133681 ($\sim 59\%$)	94562 ($\sim 41\%$)
PHSD	420065	368689 ($\sim 88\%$)	336032 ($\sim 91\%$)	32657 ($\sim 9\%$)

Table 5.6: This table shows the number of primary and secondary tracks with a DCA < 1 cm. Columns represent, from left to right: event generator, Total number of tracks (ToT) from the Monte Carlo, from the Associated Monte Carlo, from the Primary tracks, and from Secondary tracks. The numbers in parentheses in columns 4 and 5 represent the percentage of the sample with respect to the total number of AMC tracks (same as in Table 5.5).

Data	ToT MC	ToT AMC	ToT PrimT	ToT SecT
UrQMD	166730	180337 ($\sim 108\%$)	107108 ($\sim 59\%$)	73229 ($\sim 41\%$)
PHSD	420065	287815 ($\sim 68\%$)	269884 ($\sim 94\%$)	17931 ($\sim 6\%$)

Table 5.7: Number of primary and secondary tracks with a DCA < 0.5 cm. Columns from left to right: event generator, Total number of tracks (ToT) from the Monte Carlo, from the Associated Monte Carlo, from the Primary tracks, and from Secondary tracks. The numbers in parentheses in columns 4 and 5 represent the percentage of the sample with respect to the total number of AMC tracks (same as in Table 5.5).

total number of tracks corresponding to the X species for the UrQMD data (ToT UrQMD) and for the PHSD data (ToT PHSD), also the percentages of the X particle species with respect of the total number of reconstructed tracks (% in ToT AMC) for UrQMD/PHSD. The numbers in parentheses represent the tracks' reconstruction efficiency (how many of the MC tracks can be —at most— reconstructed). As it can be observed, the overall efficiency stays about the same for each data set, being the highest for π^\pm, p^\pm ($\sim 95\%$) and the lowest for K^\pm ($\sim 80\%$). The relative abundances of each particle species is rather similar for both event generators, having only a subtle difference in the case of p^+ . Most of the primary particles produced in the collision are π^+ ($\sim 70 - 80\%$), about $\sim 12 - 25\%$ are p^\pm and the least contribution comes from the K^\pm ($\sim 7\%$). The relative abundances remain more or less similar even when applying several different cuts.

Particle	ToT UrQMD	ToT PHSD	% in ToT AMC
π^+	51938 ($\sim 95\%$)	143870 ($\sim 96\%$)	33/36
K^+	6658 ($\sim 82\%$)	25115 ($\sim 82\%$)	4/6
p^+	37061 ($\sim 95\%$)	45881 ($\sim 96\%$)	24/14
π^-	56493 ($\sim 95\%$)	167336 ($\sim 96\%$)	36/40
K^-	3964 ($\sim 81\%$)	13458 ($\sim 82\%$)	3/3
p^-	500 ($\sim 96\%$)	1042 ($\sim 95\%$)	0.3/0.3

Table 5.8: Information per particle species only for primary tracks. Columns from left to right: particle type, total number of reconstructed tracks from UrQMD, total number of reconstructed tracks from PHSD, and the percentage of tracks of that particle specie for UrQMD / PHSD. The number in parentheses in columns 1 and 2 represents the tracks' reconstruction efficiency.

Table 5.9 shows how the repeated tracks' contamination (\sim RT) and secondary tracks' contamination (\sim SecT) effects propagate per particle species, with the basic kinematics cuts plus a DCA >1 cm cut. As it can be observed from the column corresponding to the UrQMD tracks, most of the contamination comes from secondary particles, either from π^\pm or K^\pm , whereas the contamination from p^\pm even if considerable, is not the main source. For the case of the PHSD tracks, the contamination coming from secondary particles is quite reduced for the case of K^\pm , whereas the contamination from π^\pm is greatly reduced compared to the UrQMD. The main source of contamination from secondary tracks is due to the p^\pm and is in correspondence to that of UrQMD. On the other hand, the contamination due to the repeated tracks is very low and equal for both data, at most about 1% per particle species, which is almost negligible.

Particle	ToT UrQMD	ToT PHSD	\sim RT(%)	\sim SecT(%)
π^+	84735 (\sim 155%)	131027 (\sim 87%)	1/1	48/7
K^+	9733 (\sim 120%)	21004 (\sim 69%)	1/1	41/0.1
p^+	37339 (\sim 95%)	58117 (\sim 101%)	1/1	14/19
π^-	90595 (\sim 152%)	147729 (\sim 88%)	1/1	47/8
K^-	5317 (\sim 109%)	9341 (\sim 69%)	1/1	37/0.32
p^-	524 (\sim 101%)	1471 (\sim 134%)	1/1	17/37

Table 5.9: Information per particle species with a DCA < 1 cm. Columns from left to right: particle type, total number of reconstructed tracks from UrQMD, total number of reconstructed tracks from PHSD, contamination due to repeated tracks for UrQMD / PHSD, and contamination due to secondary tracks for UrQMD / PHSD. The number in parentheses in columns 2 and 3 represents the the tracks' reconstruction efficiency.

In Figures 5.1 and 5.2, the π^+ 's z vertex vs. DCA distribution are presented for both data sets, which represents the majority of the source of contamination from secondary particles.

As seen in Figure 5.1, both the primary and secondary pions are denser in the low DCA region, and only some extra secondary pions appear when collisions at a position closer to the edge of the TPC occur. This explains why a DCA cut does not work for the selection of primary particles, but it does not explain why this happens.

Figure 5.2 refers to a different situation, the smearing of the z vertex is not as big as for the UrQMD data, which was already discussed in the previous chapter. The distribution for primary and secondary particles looks similar in the z vertex direction, but different in the DCA. Basically, there is a considerable amount of π^+ having a high (> 1) DCA, which in fact are taken out by the DCA cut, thus reducing the contamination from secondary tracks for the PHSD data.

In Table 5.10 we observe that the results are similar to those of the Table 5.6. The comparison is for each event generator, not between them. The conclusion is that a very restrictive cut over the z vertex (second column), additional to the DCA <1 cm, makes no real difference to the amount of secondary tracks' contamination (SecT cont.), neither for PHSD nor for UrQMD. Differences do exist but they are very small and mainly given by the amount of events considered for the analysis. If we were to observe a considerable difference, an even more restrictive cut on the z vertex should be applied, but as we reduce the cut,

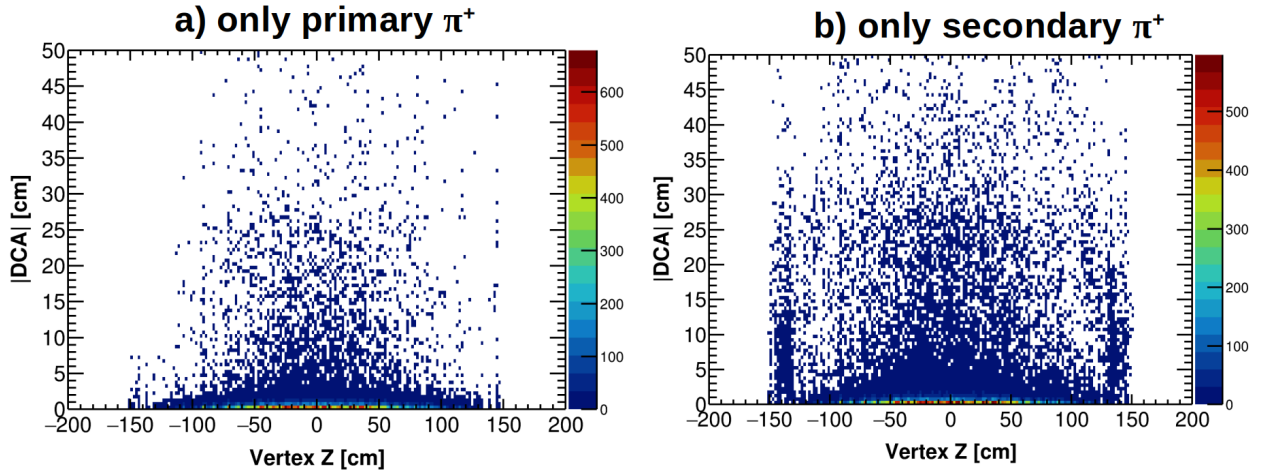


Figure 5.1: Z vertex vs DCA of π^+ from the UrQMD Bi+Bi data with $p_T > 0.1$ GeV/ c and $|y| < 0.5$. Primary tracks only (a), and secondary tracks only (b).

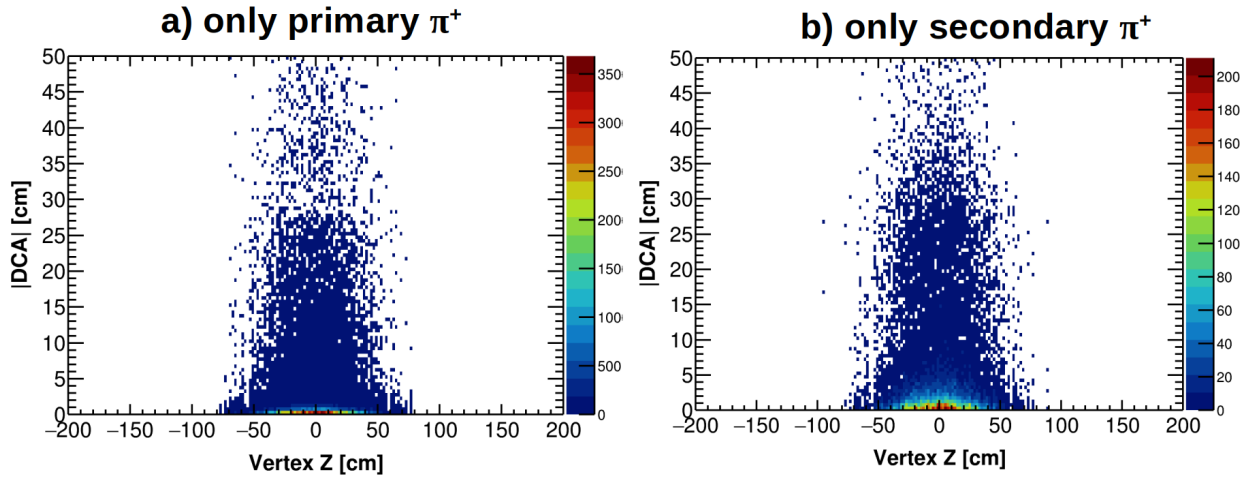


Figure 5.2: Z vertex vs DCA of π^+ from the PHSD Bi+Bi data with $p_T > 0.1$ GeV/ c and $|y| < 0.5$. Primary tracks only (a), and secondary tracks only (b).

more events will be taken off. So a very restrictive cut should only be applied when a really big sample is analyzed.

Table 5.11 shows the efficiencies and contamination with an implemented cut on the $\chi^2/(\text{Number of hits}) < 4$. Table 5.11 is also in good agreement with Table 5.10. Then a more restrictive cut should be applied if one wants to observe some differences. But one should be careful to not take out too many tracks in this case, and thus reduce the reconstruction efficiency greatly.

Table 5.12 shows the total amount of secondary particles produced in the analyzed data (No. SecT). We also show the number of secondary tracks which are produced at the same time at which the collision occurs (SecT T_0). Now, when the reconstruction process takes place, the whole collision events (simulated by the event generators) are considered to occur at times $T_0 = 0$. This implies that when the transport simulation initiates, the time starts running, and thus all the particles produced by any physical process will be considered as

Data	$V_z < [\text{cm}]$	Rec eff. (%)	RT cont. (%)	SecT cont. (%)
UrQMD	50	137	1	41
PHSD	30	87	1	9

Table 5.10: Different efficiencies for a selection of basic cuts, plus z vertex cut, plus $\text{DCA} < 1$ cm. Columns from left to right: event generator, the value of the Z vertex cut, tracks’ reconstruction efficiency, contamination from repeated tracks and contamination from secondary tracks.

Data	Rec eff. (%)	RT cont. (%)	SecT cont. (%)
UrQMD	136	1	41
PHSD	87	1	9

Table 5.11: Different efficiencies for a selection of basic kinematic cuts, plus $\chi^2/\text{Nofh} < 4$, plus $\text{DCA} < 1$ cm. Columns from left to right: event generator, tracks’ reconstruction efficiency, contamination from repeated tracks and contamination from secondary tracks.

secondary particles. In the UrQMD data one observes up to 41% of secondary particles produced at $T = 0$. We argue that, most likely (or at least dominantly), they come from heavy resonances which are decaying immediately (for any practical purposes). This makes sense when observing the input file, because the software enforces a decaying of all unstable particles¹ when the simulation ends [62]. But for the case of the UrQMD Bi+Bi collision, some resonances were considered as stable throughout the whole collision events, they were “deactivated” (to decay). Finally, when the simulation through the detector is done by the GEANT software, those resonances are again “activated”, and so they decay quickly. All those particles are then considered by the reconstruction process as secondary tracks, produced at a time $T = T_0 = 0$. This implies that a cut over the DCA will not be able to distinguish properly with the definition of primary/secondary tracks considered by the reconstruction algorithm. This problem could be solved (at least most of this contamination) if no “stb” option is activated in the input file, so we do not expect that the UrQMD Au+Au data at all energies includes this problem when applying this same analysis.

Data	No. SecT	SecT T_0
UrQMD	163000 ($\sim 51\%$)	93969 ($\sim 58\%$)
PHSD	111694 ($\sim 22\%$)	8289 ($\sim 7\%$)

Table 5.12: Amount of secondary tracks with basic selection cuts. The last column indicates the number of secondary tracks which are produced at $T = T_0 = 0$, meaning that they are produced at the same time as the collision events. The numbers in parentheses indicate the percentage of secondary tracks with respect to the total number of tracks (left), and the percentage of secondary tracks produced at $T_0 = 0$ with respect to the total number of secondary tracks (right).

¹We are referring to the default settings of the UrQMD software. In that case, a decay is always enforced even if the time is so small that the unstable particle is unlikely to decay. This can be changed by the user in the input file.

This is only a summary of the most relevant results, different cuts and combinations were also studied. The idea was to optimize those values in order to obtain the highest efficiency and lowest contamination with sufficient statistics. The approach was to make use of the *significance*, defined as $s = \text{signal}/\sqrt{\text{signal} + \text{background}}$. When using this method, for each different value of the cut parameter, the corresponding significance is calculated, then a plot of the parameter vs. significance is realized, and the parameter value at which the distribution reaches its maximum is what we call the “optimized value”. This approach (with this definition of significance) tends to favor the identification of more particles, even if it reduces the efficiency and increases the contamination. So, even when flawed, this is the current method for determining the track cuts’ values, but a more adequate definition of significance has yet to be found.

In Table 5.13 all parameter cut values are shown. For the case of the Au+Au collisions only the set at 9.2 GeV was optimized by means of the significance, but this was realized in an older version of the MPDroot. This was mainly due to the limited time and because of the ineffectiveness of the current definition of the significance.

Parameter	Au+Au UrQMD	Bi+Bi UrQMD	Bi+Bi PHSD
$ Z < [\text{cm}]$	100	100	none
Nofh >	13	25	24
$\chi^2/\text{Nofh} <$	8	4	4
DCA < [cm]	1	1	1
σ_E	3	2	2
σ_M	3	2	2
TPC if $p_T < [\text{GeV}/c]$	0.3	0.4	0.4

Table 5.13: Values of the cuts “optimized” for this work. They represent, from top to bottom: The maximal z vertex position, the minimal number of hits, the maximal $\chi^2/(\text{number of hits})$, the maximal distance of closest approach, the standard deviation from the average energy lost, the standard deviation from the average mass-squared and the p_T at which TPC alone can make the identification. The values obtained for the UrQMD Au+Au analysis were obtained only at 9.2 GeV, with an older version of the MPDroot.

5.2 Transverse momentum distributions

The transverse momentum distributions are presented for $0.1 \text{ GeV}/c < p_T < 2 \text{ GeV}/c$ and $|y| < 0.5$ at all energies and for each particle species. These distributions are obtained by filling a histogram with the p_T information corresponding to each particle type for all the events satisfying the selection criteria. The distributions are written in the form

$$\frac{dN}{dy dp_T} = F(p_T), \quad (5.1)$$

where $F(p_T)$ is only a function of the transverse momentum. This is because, in the central region (for $p_L \ll \sqrt{s_{NN}}$), the distributions are independent of the rapidity, which makes them boost-invariant [2].

In Figures 5.3-5.5 we show the transverse momentum distributions for the three Au+Au data sets at all energies. PHSD and HSD are almost identical, but compared to UrQMD they only exhibit similar behaviour overall, particularly at medium p_T . At low p_T values, (P)HSD distributions reach higher values, whereas at high p_T they take lower values. We observe that the positive and negative distributions for pions are rather similar (for the three sets), meaning that they are produced in more or less the same proportion. As we increase the energy of the collision, the transverse momentum distribution reach higher values overall, and so more particles are created. Even tough pion production in heavy-ion collision is not yet fully understood, it is well known that at NICA energies, their production, propagation and reabsorption is mostly related to the properties of the Δ resonance [75, 76]. In particular, their production at low momentum can be explained by the decay kinematics of Δ resonances, but there is also an effect due to the radial flow [77]. In particular, we can understand to some extent the spectra by the reabsorption of the pions at different stages. High transverse momentum pions stem from the early stage of the collision, and so they are mostly reabsorbed by the medium², whereas low transverse momentum pions are produced in the late stage when the system is near the freeze-out [78]. This explanation gives a general description of the spectra obtained in Figures 5.3-5.5, but it is still under discussion if their behavior at high transverse momentum is also related to the decay of the Δ resonances or this is just a thermal effect.

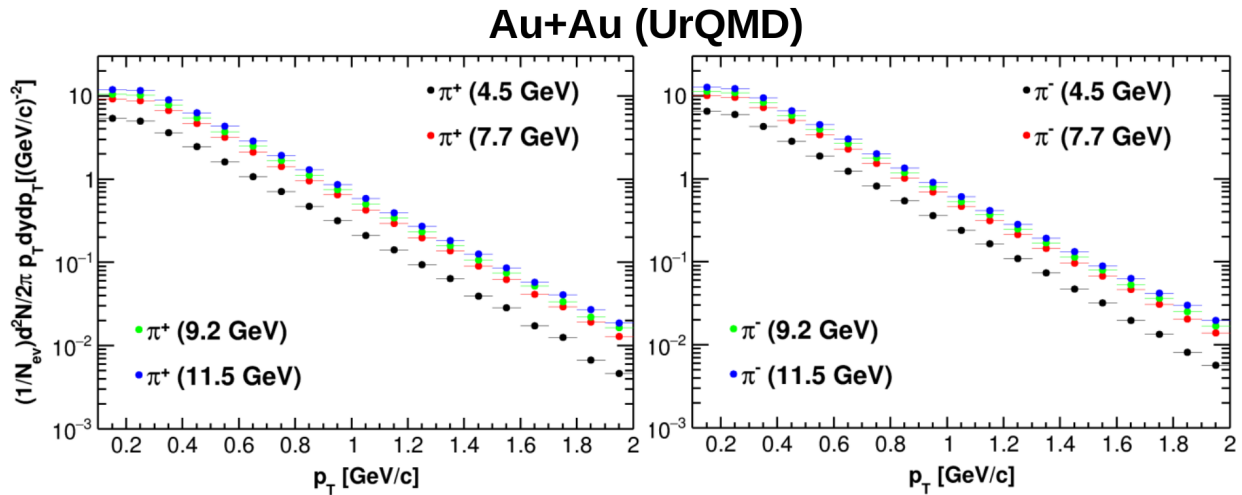


Figure 5.3: Transverse momentum distributions (Monte Carlo) in Au+Au for π^\pm at different energies for the UrQMD event generator.

²For example, via the sequential process $\pi N \rightarrow \Delta$ and $\Delta N \rightarrow NN$.

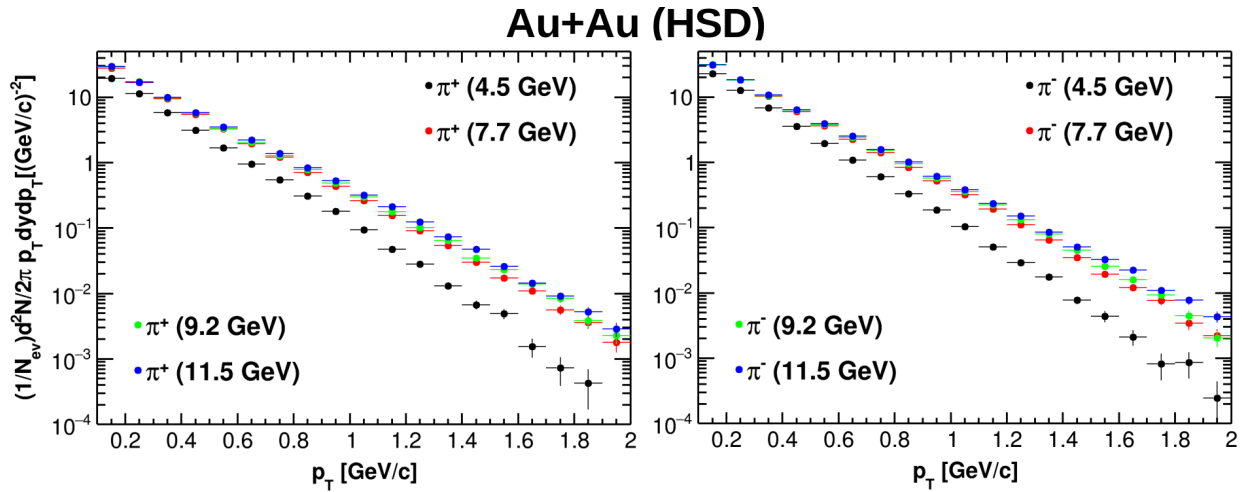


Figure 5.4: Transverse momentum distributions (Monte Carlo) in Au+Au for π^\pm at different energies for the PHSD event generator (in HSD mode).

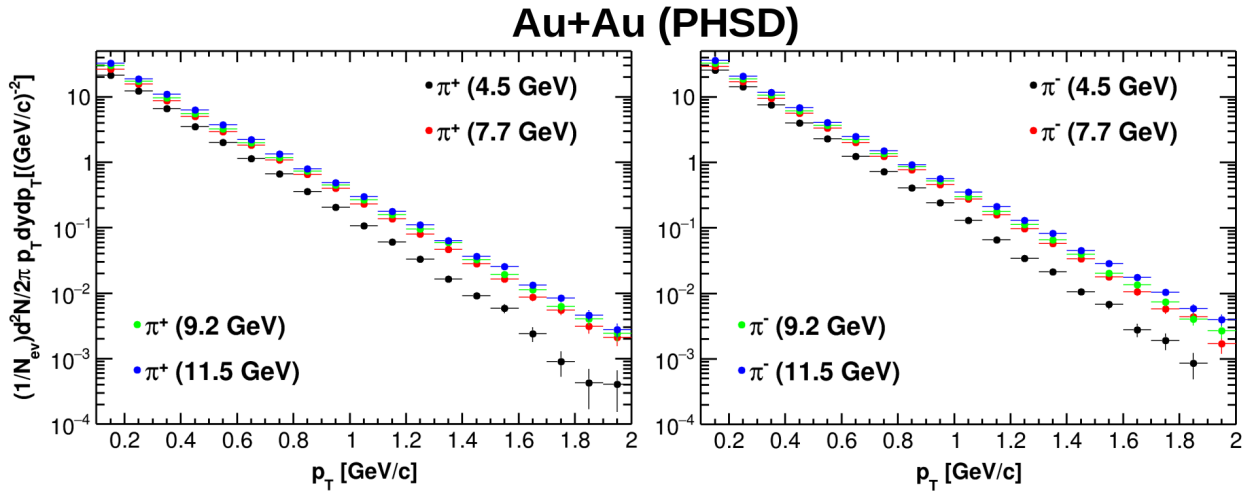


Figure 5.5: Transverse momentum distributions (Monte Carlo) in Au+Au for π^\pm at different energies for the PHSD event generator (in PHSD mode).

For the protons and antiprotons (see Figures 5.6-5.8), the spectra reveal considerable differences. Here again, PHSD and HSD are almost identical to each other, but compared to UrQMD they differ greatly, particularly at low-to-medium p_T . For the UrQMD case, the maximum of the proton distribution is reached at ~ 0.5 GeV, but for (P)HSD the maximum occurs at 0.1 GeV. It looks as if the (P)HSD distributions were just the UrQMD distributions moved to the left. This might be due to the radial flows, because each model predicts different behaviour. The number of antiprotons produced drops dramatically as we decrease the energy of the collision. Compared to the protons, they are produced $\sim 100 - 10000$ times less frequently, but follow the same trend as discussed for the protons. Note that the bin size for the lowest energy antiprotons is bigger because otherwise the poor statistics would produce large fluctuations. It is interesting to notice that the distribution for protons reach higher values as we decrease the energy of the collision, but the situation is reversed for the

antiprotons. This is probably because most of the contributions to the proton distribution come from the protons of the colliding nuclei. This means that a fair amount of protons are colliding elastically when the energy available is low, but as the energy increases, elastic collisions where a proton is a part of are less likely.

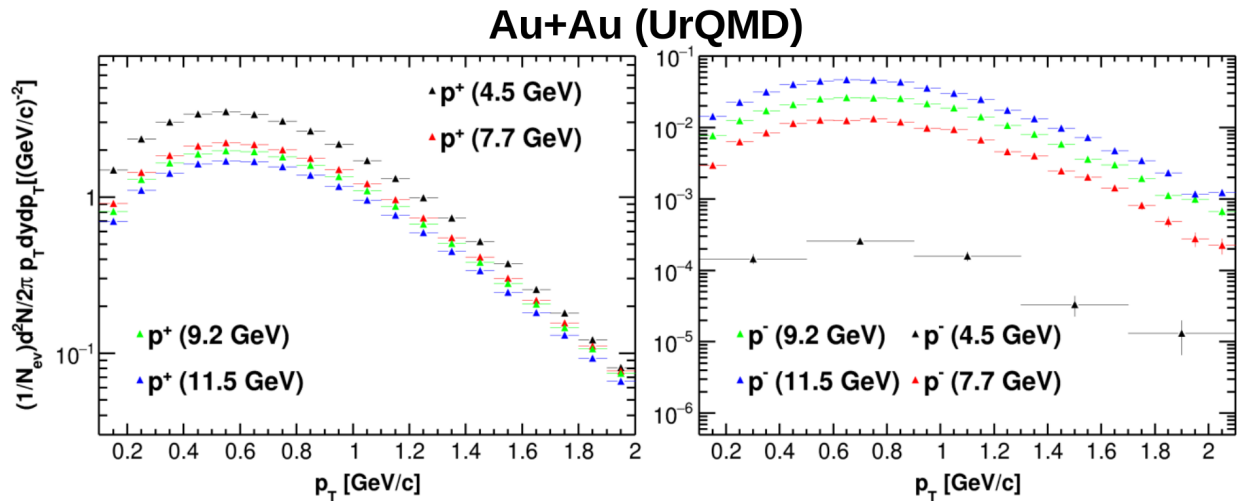


Figure 5.6: Transverse momentum distributions (Monte Carlo) in Au+Au for p^\pm at different energies for the UrQMD event generator.

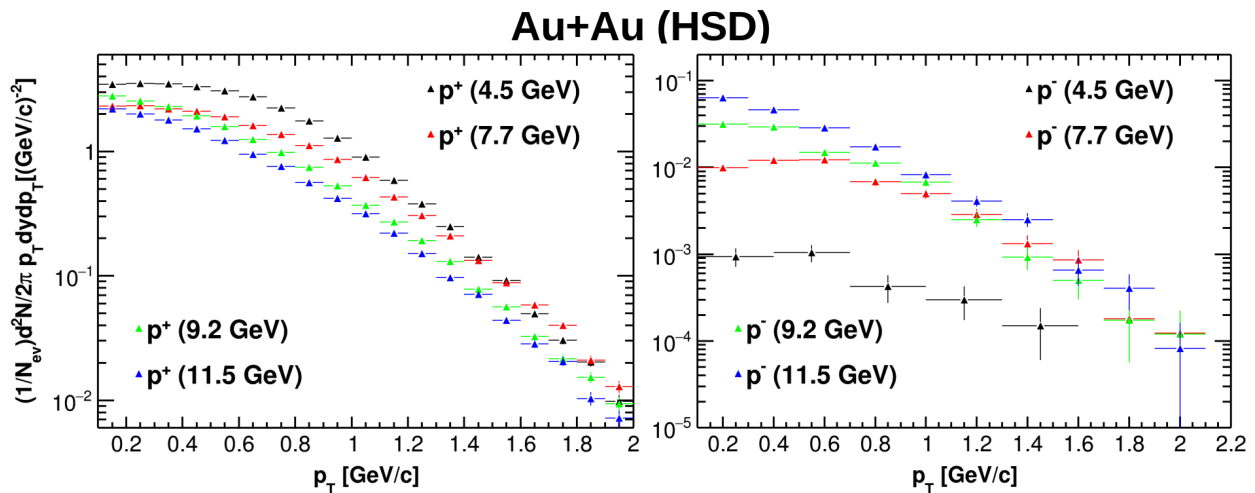


Figure 5.7: Transverse momentum distributions (Monte Carlo) in Au+Au for p^\pm at different energies for the PHSD event generator (in HSD mode).

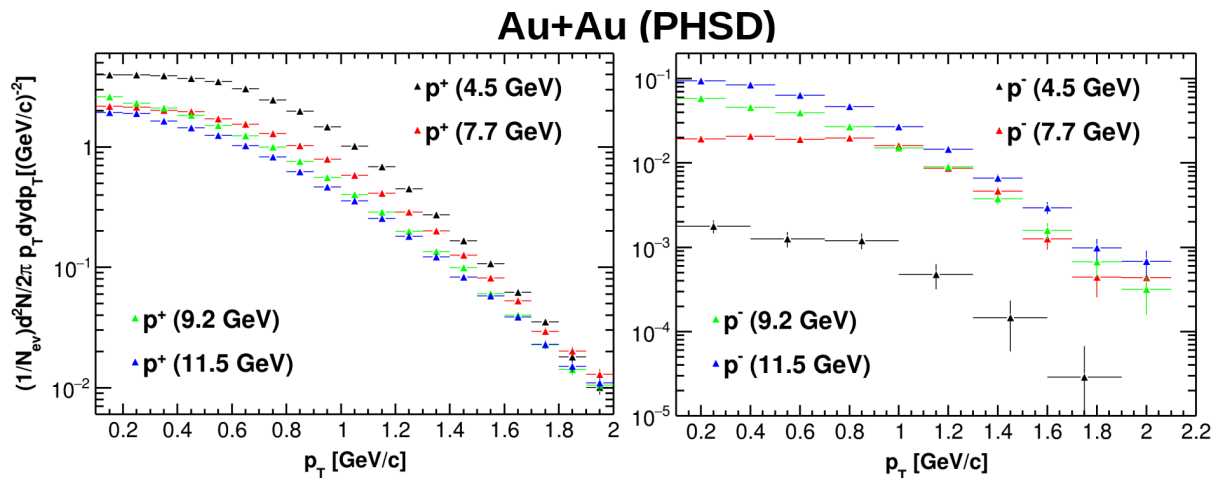


Figure 5.8: Transverse momentum distributions (Monte Carlo) in Au+Au for p^\pm at different energies for the PHSD event generator (in PHSD mode).

The transverse momentum distributions for kaons is shown in Figures 5.9-5.11 and the shapes of the distributions look similar for both the positive and negative case and at all energies and event generators. The same behaviour described for the pions and protons is shown here, (P)HSD data reaches higher values at low p_T and lower at high p_T . Given that the PHSD data consist of only 10,000 events, the negative kaons at high p_T have considerable fluctuations at low energies, where they are not so abundantly produced. The main difference between positive and negative kaons (independently of the model) is in the proportion. At low energies, the negative kaons are less abundantly produced, but as the energy increases, the situation tends to be more balanced. In both cases, the distribution rises overall as we increase the energy of the collision. The kaons are of particular interest because of their valence quark content; K^+ are composed of $u\bar{s}$ and K^- of $s\bar{u}$. Given that the strange content before the collision is zero, some of the strangeness production mechanisms can be studied by means of these mesons. Different approaches [79–81] have shown consistently that there are two main chains contributing to the K^+ production: $\pi N \rightarrow K^+ Y$ and $\Delta N \rightarrow K^+ Y N$, with $Y \in \{\Lambda^0, \Sigma^0\}$. Thus, the production of the strange baryons $\Lambda^0(uds)$ and $\Sigma^0(uds)$ is highly correlated to that of the K^+ , because typically K^+ is produced in pairs with a Λ^0 or Σ^0 due to strangeness conservation. For the K^- , the two main production channels are: $\pi \bar{\Lambda} \rightarrow K^- N$ and $\pi \Sigma \rightarrow K^- N$. This is known as a flavor exchange reaction, where the strange quark from the hyperon is exchanged with a light quark (u or d). A major difference in kaon production occurs because the K^- are strongly absorbed by the medium, whereas the K^+ can hardly be absorbed because of their \bar{s} content [82, 83].

It is evident that each model is distinct, and it is interesting that the major differences are observed for the (anti)proton distributions. Even more intriguing is that, generally speaking, the (P)HSD distributions looks as a UrQMD distribution moved to the left for all particles and at all energies. The gross features of the transverse momentum distributions can be somewhat understood in the presented terms, but a more precise discussion would be required to understand the mechanisms implemented in the generator. We are limited to the capacities of the model, and a comparison to experimental data is essential if we want to discern from different approaches. A further discussion will be given in the following sections.

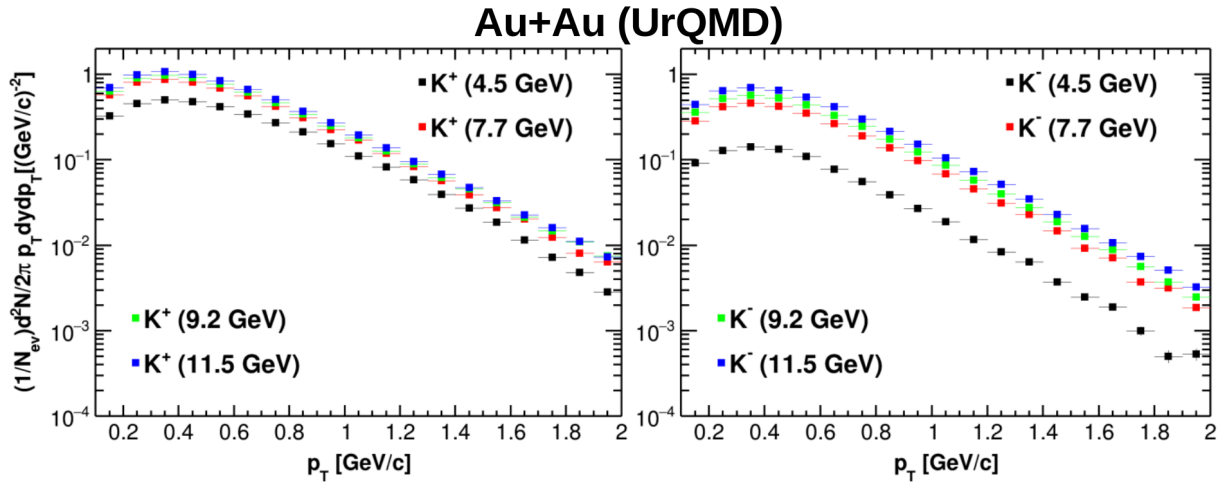


Figure 5.9: Transverse momentum distributions (Monte Carlo) in Au+Au for K^\pm at different energies for the UrQMD event generator.

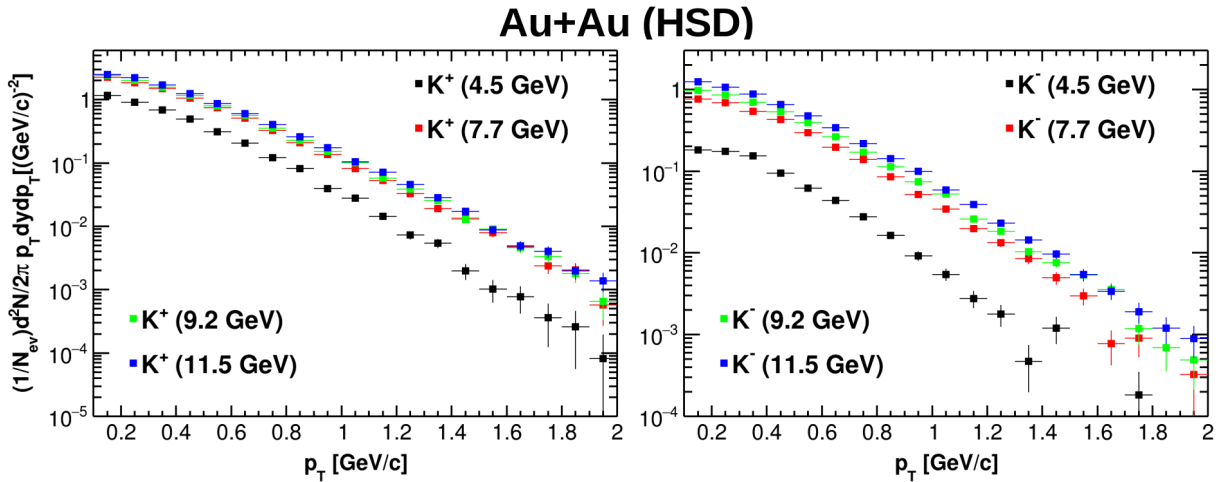


Figure 5.10: Transverse momentum distributions (Monte Carlo) in Au+Au for K^\pm at different energies for the PHSD event generator (in HSD mode).

5.3 Uncorrected reconstructed distributions

A complete analysis of the spectra obtained by a particular experiment should take into account several corrections to the distributions, by the efficiency, acceptance, background noise, etc. It is not an easy task and the complete corrections can only be done when the apparatus is properly working. For this work, only the raw spectra have been analyzed, the distributions presented in this section are just the reconstructed transverse momentum distributions, without any correction. They are presented for $0.1 \text{ GeV}/c < p_T < 2 \text{ GeV}/c$ and $|y| < 0.5$, with the selection criteria from Table 5.13 for all energies.

In Figures 5.12-5.14 we observe the same behavior (qualitatively) as that described for the MC distributions. It is interesting to notice that at a relatively high transverse momentum ($\gtrsim 0.6 \text{ GeV}/c$), the MC and reconstructed distributions are quantitatively similar. Only at low transverse momentum ($\lesssim 0.6 \text{ GeV}/c$) we observe considerable differences for the positive

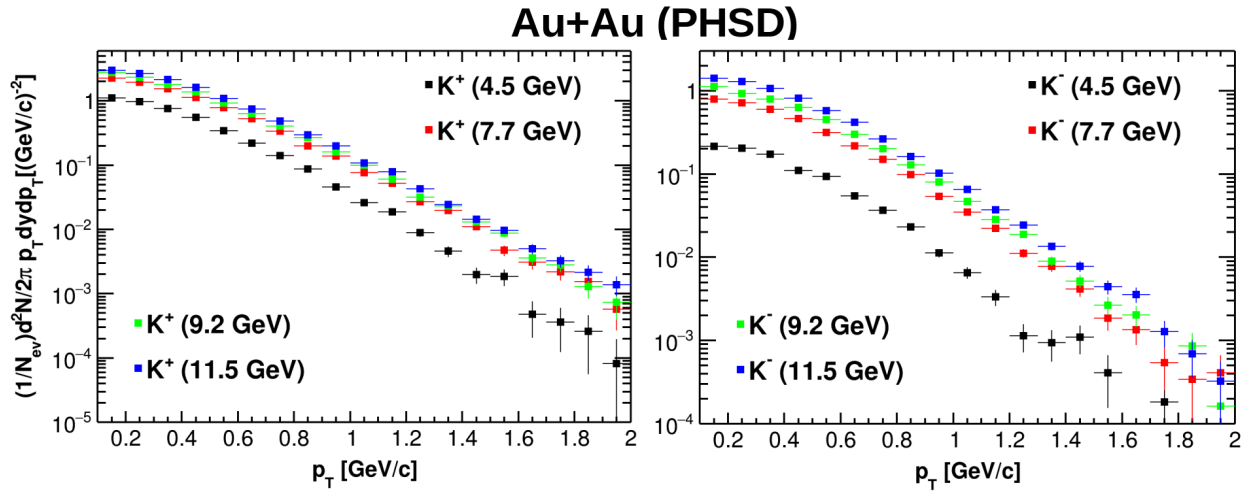


Figure 5.11: Transverse momentum distributions (Monte Carlo) in Au+Au for K^\pm at different energies for the PHSD event generator (in PHSD mode).

and negative kaons and for the protons: the reconstructed distributions at low p_T reach lower values, as if there were almost no low momentum K^\pm and p . On the other hand, for pions the disagreement occurs only at the first p_T bin for all energies, and for antiprotons at the lowest energy the agreement is fairly good.

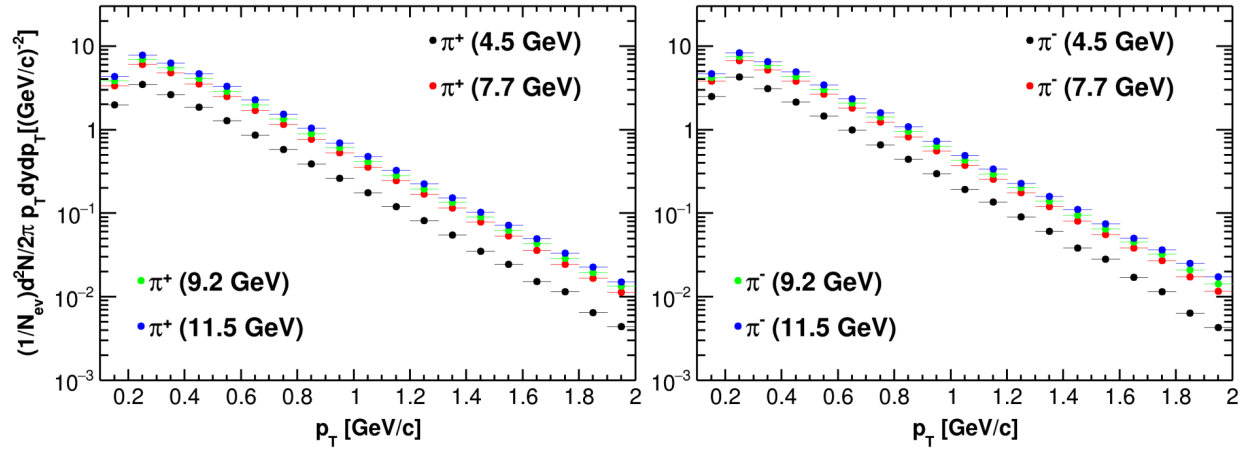


Figure 5.12: Transverse momentum distributions (reconstructed) of π^\pm for UrQMD Au+Au at different energies.

The difference at low momentum K^\pm and p^\pm occurs at all energies. This is not yet fully understood, but it is most likely that this is because of the characteristics of the TPC, because it can be argued (see Figures 4.4 and 4.6) that most of the low transverse momentum kaons or protons are either being identified as high transverse momentum pions or not identified at all. This complements the fact that the TOF system cannot identify low momentum particles or they get lost due to the mismatch effect. It could also be due to the assigned values of parameters given to make the identification (selection criteria). This last explanation seems unlikely, because even though the optimization process does not work as expected, the testing with different cut values showed that those cuts only change the amount of particles

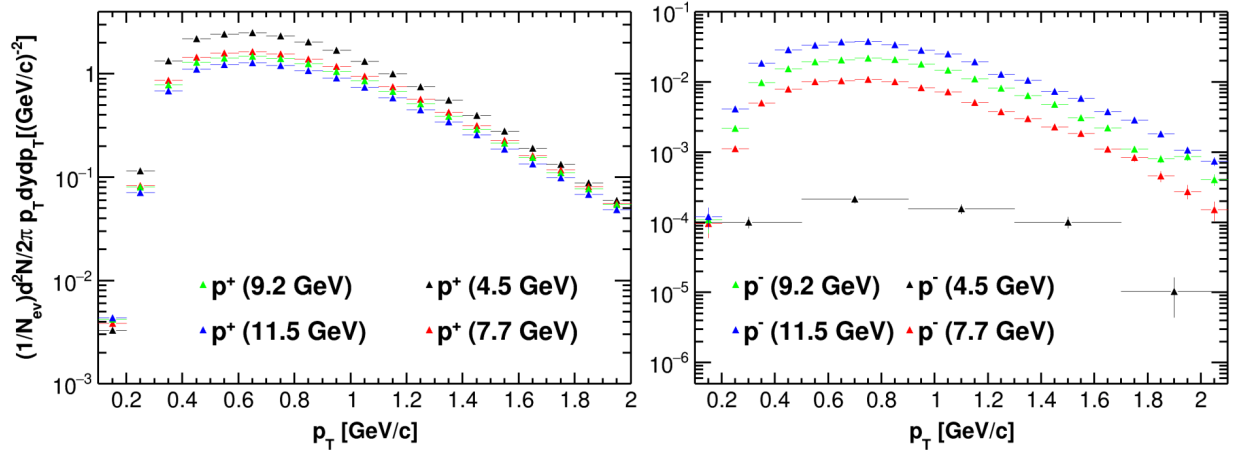


Figure 5.13: Transverse momentum distributions (reconstructed) of p^\pm for UrQMD Au+Au at different energies.

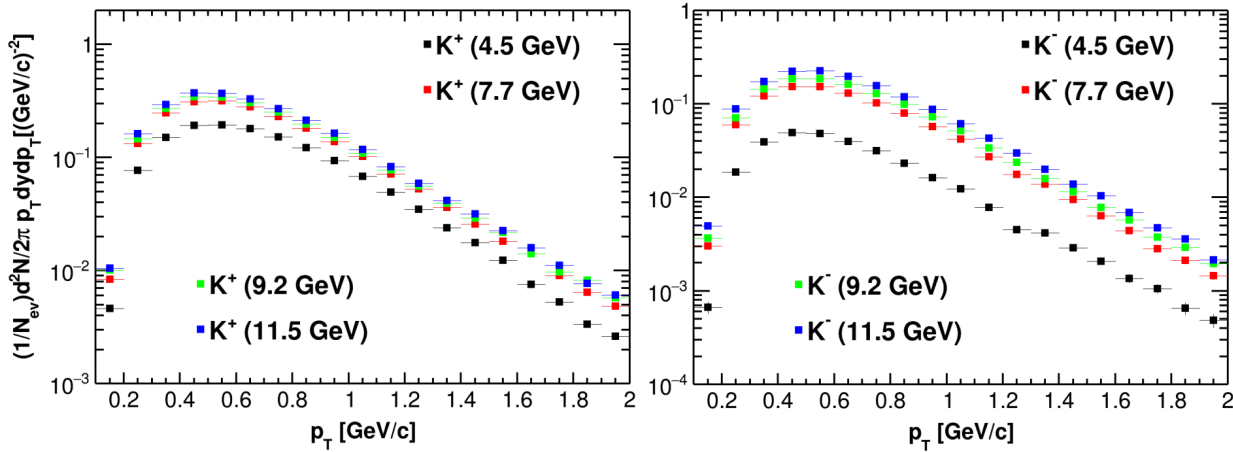


Figure 5.14: Transverse momentum distributions (reconstructed) of K^\pm for UrQMD Au+Au at different energies.

detected, but not the shape (there still exists the drop at low transverse momentum). Thus, the only difference for different cuts (within reason) was quantitatively at all bins and by approximately the same amount, so the distribution was either worsen at low p_T or slightly improved at the cost of higher contamination. We expect to obtain similar results both for the efficiency/contamination as for the transverse momentum distributions with the PHSD Au+Au data sets, but in any case, they are only at the MC stage. It remains as an open question for future development.

Yet again, the software employed to make the analysis is not the newest version. At the beginning of this work, we employed an even older version of the MPDroot, given that the ICN cluster was not updated. And so the macros and the overall procedure have been improved progressively. Some minor errors can be attributed to the version, because differences can be observed when comparing older results. Even so, the overall behaviour described in this chapter remains similar, but the proper study of the reconstructed distributions can only be done when the corrections are fully implemented. In order to avoid any problem carried out

by the raw distributions, the main results are obtained only at the MC level. But the current analysis discussed so far was a part of the learning process, and it will be important for the future development, particularly when the MPD starts operations.

5.4 Bi+Bi collisions at 9.2 GeV

The Bi+Bi collisions need their particular section because they were generated by the JINR, and some preliminary results have already been published [84]. Figure 5.15 shows the transverse momentum distribution (both the MC and reconstruction) for pions on the left side, and the efficiency (contamination) on the right side. A direct comparison for the MC and reconstruction is presented for the pions, and even though they are qualitatively similar (except for the first bin), the reconstructed bins overall are at a higher positions than the generated points, meaning that there seems to be an excess of the measured particles. This could be (as explained in the previous section) because a considerable amount of particles with transverse momentum between $\sim 0.2 - 2$ GeV/c are being identified as pions even if they are not. But most likely, the main source of this excess for this sample comes from secondary tracks. The contamination of the same pions remains approximately constant with maximum peaks at 10%.

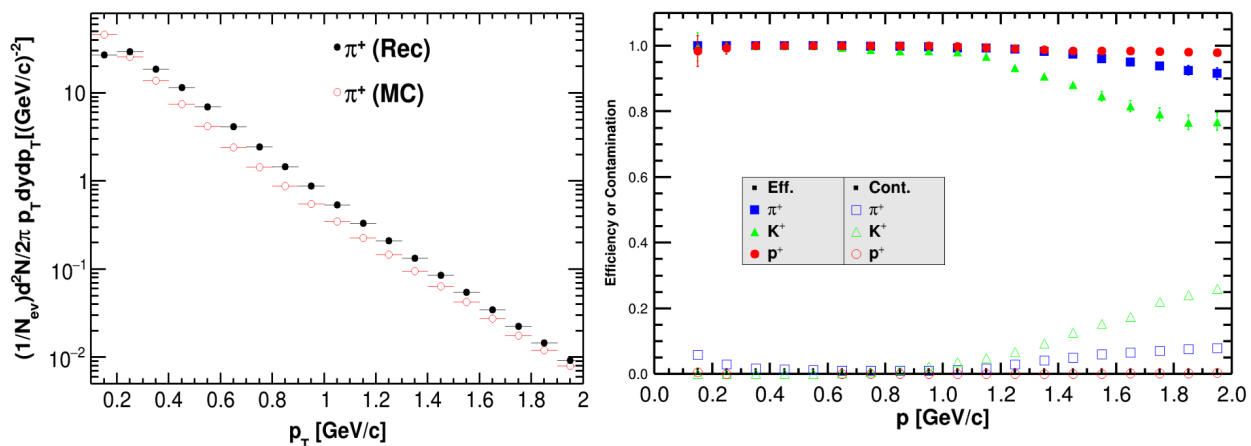


Figure 5.15: Transverse momentum distributions for π^+ , Monte Carlo and reconstruction (left). Efficiency and contamination for positive charged particles (right). All results are presented for UrQMD Bi+Bi collisions at 9.2 GeV.

According to Figure 5.16, the similarity between the transverse momentum distributions occurs only for values of $p_T \gtrsim 0.4$ GeV/c, and still it is only qualitative; quantitatively the difference is small but exists. For $p_T \lesssim 0.4$ GeV/c, the reconstructed distribution drops considerably (as much of ~ 100 times for the first bin). This is in accordance with the explanation for the pion distribution, meaning that a considerable amount of kaons and protons are being identified as pions or not identified at all. Particularly, given that pions are of the lowest mass, low transverse momentum kaons or protons are being identified as mid-to-high transverse momentum pions. Overall, the behavior of the reconstructed data compared to the MC, for all five data sets, is in similar terms.

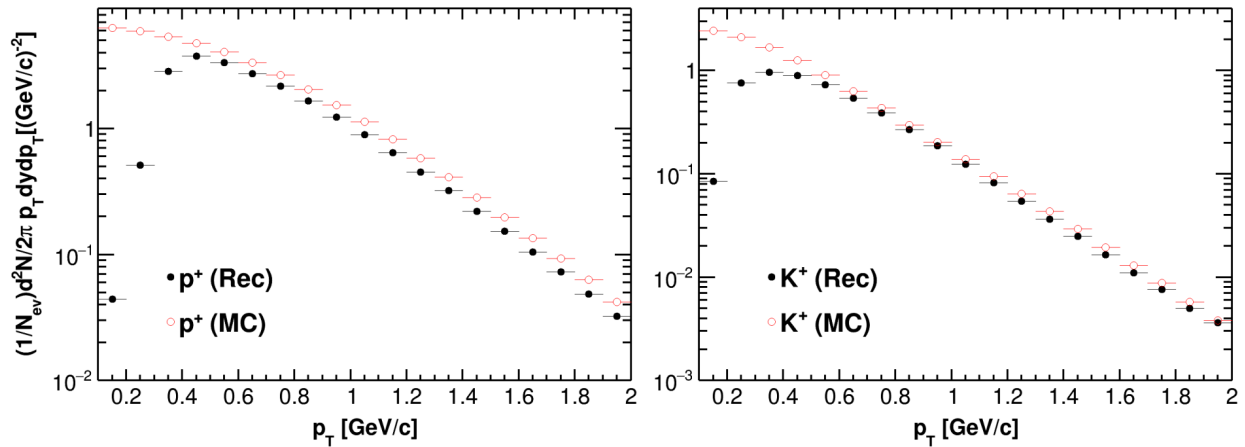


Figure 5.16: Transverse momentum distributions of p^+ (left) and K^+ (right). Both Monte Carlo and reconstruction (MC and Rec) are presented for UrQMD Bi+Bi collisions at 9.2 GeV.

Figure 5.17 shows the results for the PHSD Bi+Bi collisions. The overall behaviour is qualitatively similar to that of UrQMD both for the MC and reconstruction (left side). The major difference is that in this case, the reconstructed pions are no longer at higher values than for MC. It is not clear why this difference is observed, but it could be due to the reconstruction process employed for both data sets, because they were not produced at the same time nor with the same MPDroot version. Some minor differences in the reconstruction algorithm could be responsible or some changes of the geometry. The efficiency and contamination (right side) is also in a good agreement with the UrQMD data, errors seem a bit larger overall, but the trend is similar. Another difference is that no protons are detected in the first bin, but probably more statistics is needed to draw some conclusions.

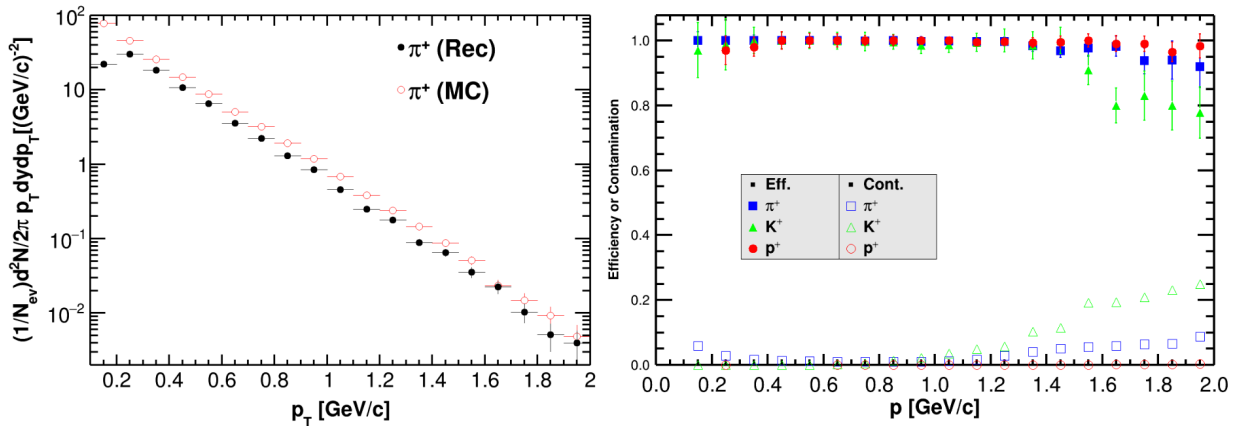


Figure 5.17: Transverse momentum distributions for π^+ , Monte Carlo and reconstruction (left). Efficiency and contamination for positively charged particles (right). All results are presented for PHSD Bi+Bi collisions at 9.2 GeV.

On the other hand, kaon and proton distributions are presented in Figure 5.18. Again, the distributions look similar to those of UrQMD, but there are about four times more K^+ than p^+ at low p_T in the PHSD model. A drop in the distribution for $p_T \lesssim 0.5$ GeV is observed, and for higher p_T values the agreement is good qualitatively, but with a slight

quantitative difference. Overall, it seems that reconstructed PHSD distributions have lower values with respect to their MC. They are even lower compared to the reconstructed UrQMD with respect to their MC. This means that less particles are being identified, but that could be an issue beyond the reconstruction process itself, most likely related with the selection criteria employed.

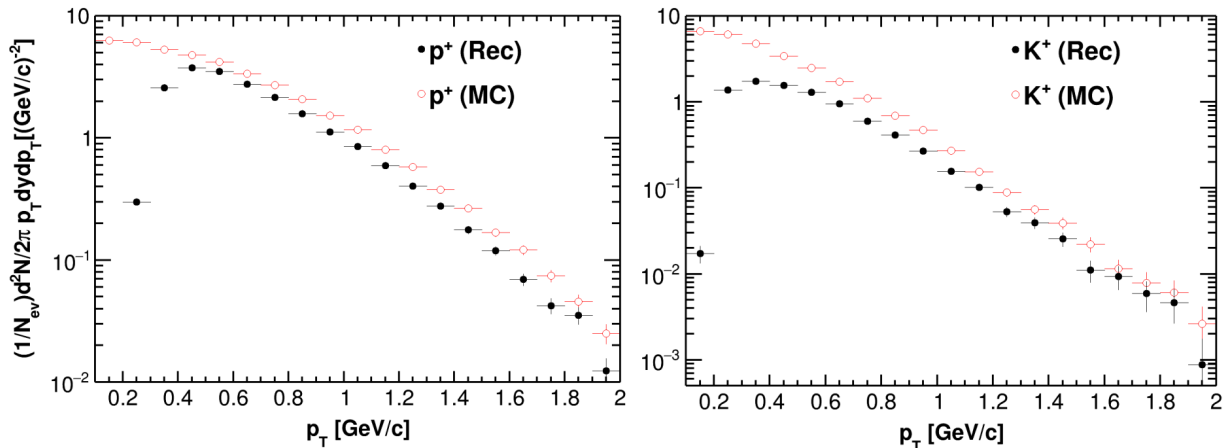


Figure 5.18: Transverse momentum distributions of p^+ (left) and K^+ (right). Both Monte Carlo and reconstruction (MC and Rec) are presented for PHSD Bi+Bi collisions at 9.2 GeV.

The main importance of the study of those distributions are:

- They form a part of the joint effort of the MPD collaboration. Its production was realized under specific requirements at the JINR. So, the results obtained with those data sets are of interest for all the members of the collaboration.
- The MPD will produce its first results precisely with Bi+Bi collisions at 9.2 GeV, so it is important to run simulations and make some predictions on what is to be expected in the real experiment.

Hopefully, this work can later be updated and completed to provide a contribution to the experiment.

5.5 Particle integrated ratios

The main focus of this work is to study the production mechanisms underlying the meson and baryon production at NICA energies. Particularly, as discussed in the Chapter 1, the K^\pm/π^\pm ratio is one of the most interesting and easiest quantities to calculate, because of the strangeness content of the kaons. In order to obtain the ratios for different particles, we should calculate how many of them are produced in the collision at freeze-out³, this is known as the particle yields. Thus, we can calculate the ratios by integrating the transverse momentum distributions over the whole volume in the phase space. For example, if we want to calculate the K^\pm/π^\pm ratio, then we should obtain

³This means that we are only interested in primary particles.

$$\frac{K^\pm}{\pi^\pm} = \frac{\int \frac{d^2 N(K^\pm)}{p_T dy dp_T} p_T dp_T dy}{\int \frac{d^2 N(\pi^\pm)}{p_T dy dp_T} p_T dp_T dy}. \quad (5.2)$$

The yields were calculated by a numerical integration of the transverse momentum distributions over the whole interval, which covers $0.1 \text{ GeV}/c \leq p_T \leq 3.0 \text{ GeV}/c$.⁴ Given that we need to calculate the ratio as a function of the energy of the collision, only the locally generated Au+Au data sets are considered for these calculations. Then again, these results are calculated only for the MC data (directly from the event generators), not for the reconstructed data. The latter will be part of the future work, but at the current stage, the main focus is to shed light on what could be the underlying production mechanisms and how to study them experimentally from the future MPD data.

A proper comparison of the generated samples with the experimental data requires to divide the samples in centrality classes. This was briefly discussed in the previous chapter, but the main idea is that a centrality class can be related to the impact parameter. We say that a collision is “central” whenever its impact parameter is low, and “peripheral” when its impact parameter is high. Experimental data taken for this analysis comprises centrality classes from 0-5% and 0-10%, which represents that percentage of the cross section. So, for the analysis of this section, the values obtained in Ref. [69] were taken. It must be clarified that those values are only valid within the UrQMD model. The values taken to construct the centrality classes for the (P)HSD model are assumed to be the same as that of the UrQMD model. It is hard to estimate at the moment how much the presented results would change if the correct values for the (P)HSD model were imposed.

Table 5.14 presents the K^\pm/π^\pm ratios at the centrality class (0 – 10)% for the UrQMD Au+Au collisions at all energies. For the ratio of positive particles, a decreasing behaviour is observed as the energy increases. For the ratio of the negative particles, an increasing behaviour is observed as the energy increases.

For the case of (P)HSD, Tables 5.15 and 5.16 show the K^\pm/π^\pm ratios at the centrality class (0 – 10)%. The same overall behaviour is observed, for the positive particles, as the energy increases, the ratio increases. The main difference is that, at the lowest energy, the PHSD model predicts a lower value, but as the energy increases, it increases more rapidly than for the HSD model. The same trend is observed for the negative particles, while both ratios increase with energy, PHSD increase at higher rate.

Overall, the ratio of negatively charged particles for UrQMD and (P)HSD present the same trend, even if the values differ slightly. But there is a striking difference in the ratio of the positively charged particles. While UrQMD suggest a strictly decreasing behaviour, the (P)HSD models suggest precisely the opposite. The exact explanation is not well understood so far, but a discussion will be given later in this chapter. First we need to incorporate additional data on particles ratios, in order obtain a better picture of what might be happening with the models.

⁴The transverse momentum distributions presented in previous sections cover up to $2 \text{ GeV}/c$, because the contamination for the reconstructed data for higher values rise, particularly for the kaons ($\gtrsim 50\%$). This analysis is at the MC level, so there is no contamination of the sample, the errors do increase at high p_T due to lower statistics, but not as much as for the reconstructed data.

$\sqrt{s_{NN}}$ [GeV]	K^+/π^+	K^-/π^-
4.5	0.16657 ± 0.00035	0.03417 ± 0.00014
7.7	0.14997 ± 0.00024	0.06736 ± 0.00015
9.2	0.14360 ± 0.00021	0.07362 ± 0.00015
11.5	0.13699 ± 0.00020	0.08041 ± 0.00014

Table 5.14: Particle integrated ratios obtained from the Monte Carlo UrQMD Au+Au collisions at four different energies. All results are presented for the centrality class 0-10%.

$\sqrt{s_{NN}}$ [GeV]	K^+/π^+	K^-/π^-
4.5	0.11538 ± 0.00263	0.02097 ± 0.00100
7.7	0.15894 ± 0.00227	0.05157 ± 0.00117
9.2	0.16816 ± 0.00218	0.06513 ± 0.00124
11.5	0.17468 ± 0.00226	0.08153 ± 0.00142

Table 5.15: Particle integrated ratios obtained from the Monte Carlo HSD Au+Au collisions at four different energies. All results are presented for the centrality class 0-10%.

$\sqrt{s_{NN}}$ [GeV]	K^+/π^+	K^-/π^-
4.5	0.11370 ± 0.00217	0.02050 ± 0.00082
7.7	0.18139 ± 0.00248	0.06087 ± 0.00129
9.2	0.19635 ± 0.00240	0.07571 ± 0.00135
11.5	0.20187 ± 0.00230	0.08754 ± 0.00137

Table 5.16: Particle integrated ratios obtained from the Monte Carlo PHSD Au+Au collisions at four different energies. All results are presented for the centrality class 0-10%.

In Figure 5.19, the calculated ratios from the three models are compared to the experimental data from AGS [85] and STAR [86, 87]. On the left side, K^-/π^- is shown, and on the right side K^+/π^+ . It can be observed that, except for the 7.7 GeV energy, the agreement between the models and the data for the negative mesons is good. Probably the UrQMD model is the closest to reproduce the trend. On the other hand, neither UrQMD nor (P)HSD reproduce particularly well the data for the positive mesons. UrQMD at 4.5 GeV seems to follow the trend but at higher energies it completely breaks down. HSD does not reproduce the trend at all, but PHSD seems to be in a fairly good agreement only at 9.2 and 11.5 GeV.

In order to complete the discussion, an analysis of the antiparticle-to-particle ratios has been realized. Figure 5.20 shows the π^-/π^+ ratio at the four energies and compared to the experimental data (left). The agreement for the three models with the data is quite good, actually the predicted values are almost identical to each other. It also shows that more π^- are produced at lower energies, but as the energy increases, the ratio tends to balance. We already knew this from the transverse momentum distributions, but we can add an explanation of this effect by recalling that the original colliding nuclei are composed mostly of neutrons (236

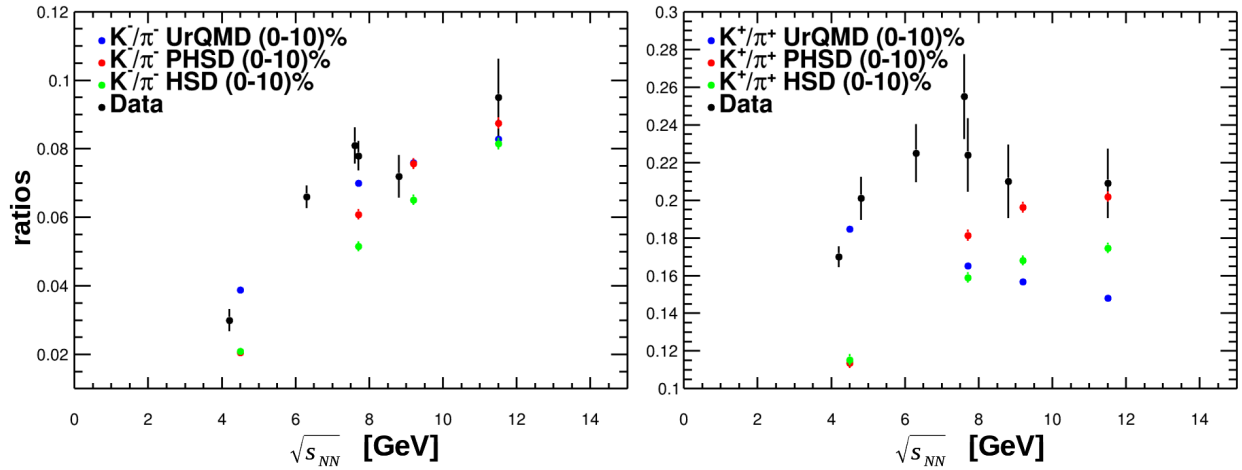


Figure 5.19: Particle ratios as a function of the collision energy for Au+Au collisions. The K^-/π^- ratio (left) is presented at a centrality class (0 – 10)% for UrQMD (blue), PHSD (red) and HSD (green). The K^+/π^+ ratio (right) is presented with the same characteristics and color codes. Data from different experiments [85–87] is shown in black.

vs. 158 protons), whose constituent quark content is udd . Now, the π^- is composed of $d\bar{u}$ and the π^+ out of $u\bar{d}$, and so it will be easier to produce particles with a d content, which are the most abundant before the collision occurs. Therefore, a considerable amount of the produced baryons and mesons, particularly at low energies, will be those with a d content, because it would require additional (higher) energy in order to produce bound states with heavier quark content.

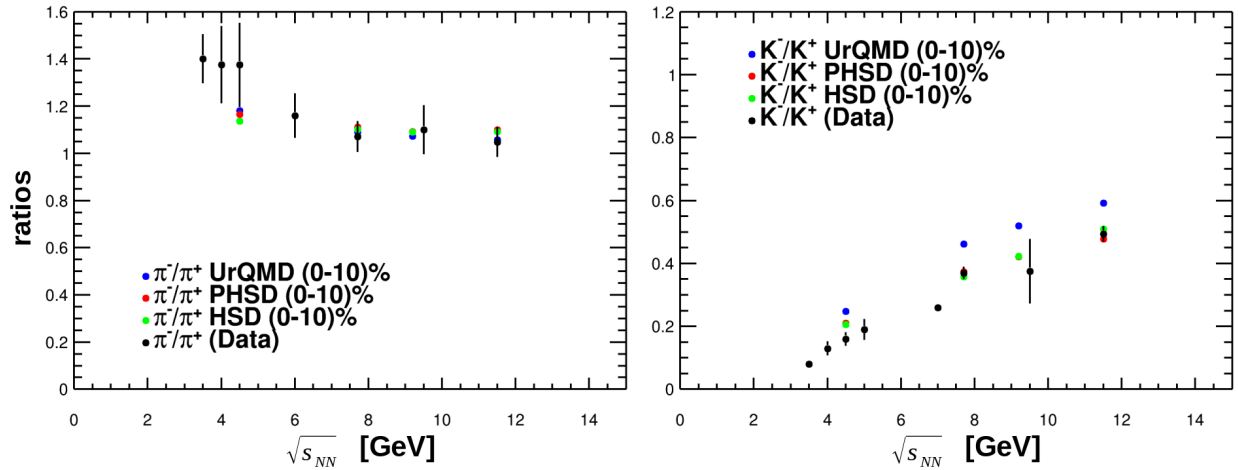


Figure 5.20: Particle-antiparticle ratios as a function of the collision energy for Au+Au collisions. The π^-/π^+ is presented at a centrality class (0 – 10)% for UrQMD (blue), PHSD (red) and HSD (green). The K^-/K^+ ratio (right) is presented with the same characteristics and color codes. Data from different experiments [85–87] is shown in black.

Figure 5.20 (right) shows the K^-/K^+ ratio at the four different energies. For the UrQMD model, the quantitative agreement with experimental data is not particularly good. The calculated ratios show an increasing behavior but not at the same rate as the experimental

data. By comparing the results obtained in Figures 5.19 and 5.20, we observe three key features which could explain the differences:

- The agreement of the π^-/π^+ ratio with the experimental data is good.
- The K^-/π^- ratio seems to follow the experimental trend, but quantitative differences are observed, particularly at high collision energy.
- Both the K^+/π^+ and K^-/K^+ ratios disagree with the experimental data.

These three statements might indicate that (at least) one of the yields is less than the expected, most likely the K^+ . A more detailed analysis is required to verify this suggestion, but at the current stage of the analysis, it seems that the UrQMD model is underestimating the K^+ production. On the other hand, the PHSD and HSD models predict very similar results, and both are in good agreement with the experimental data. The two observations in Figure 5.20 for the (P)HSD data seem rather odd, because it appears that π^+ and K^+ abundances are predicted in about the right (particle-antiparticle) proportions, and yet the K^\pm/π^\pm ratio presents considerable differences, particularly for the positive mesons.

The last of the particle-antiparticle ratios under consideration is p^-/p^+ . Figure 5.21 shows the comparison of this ratio with the data from the STAR collaboration [87]. There are only two data points to make the comparison (no more data were found), which show a discrepancy by a constant factor with a different value for each model. This is because the positions of the four energies of the three models grow in approximately the same proportion (except for the HSD at 9.2 GeV). HSD seems to fit better the experimental data, but with only two points it would be an overstatement. Given that the predicted values are either below or above the experimental data and there are no more plots to verify the predictions, it is hard to say which particle is overestimated (or underestimated). Typically, the event generators tend to underestimate the antiproton production. It would also be helpful to deal with more data at lower and intermediate energies, and higher statistics in the simulations. This is precisely the energy regime where NICA, particularly the MPD, will contribute and so one expects additional data for this ratio at those energies in the near future. For the time being, this can only be considered as a prediction.

There still persists the question about the non-predictability of the horn structure in the K^+/π^+ ratio. For the case of the UrQMD model, the evidence suggest that we should be looking at the production mechanisms of the K^+ , as discussed in this chapter, the production of the strange baryons Λ^0 and Σ^0 is highly correlated to them. Thus, by looking at the combined yield, we can see if there is in fact an underestimation in the production of these strange baryons. Figure 5.22 shows the combined yields of the Λ and Σ^0 strange baryons, both the experimental data and the predictions for the UrQMD model are in the centrality class 0-10%. These two baryons are of great importance to the K^+ yields, because they are mostly produced in pairs with the K^+ (but not with the K^- because of its strangeness content). The values predicted by the UrQMD model are well below the experimental data [88, 89], by a factor of approximately 2. Actually the trend of the UrQMD model is in qualitatively good agreement to experimental data, but for some reason, the model underestimates the production of those baryons, and consequently that of the K^+ (the reason might be due to a lack of a phase transition?).

As for the (P)HSD model, there might also be an underestimation of the K^+ yields, but that would only explain half of the problem, because the model does reproduce the

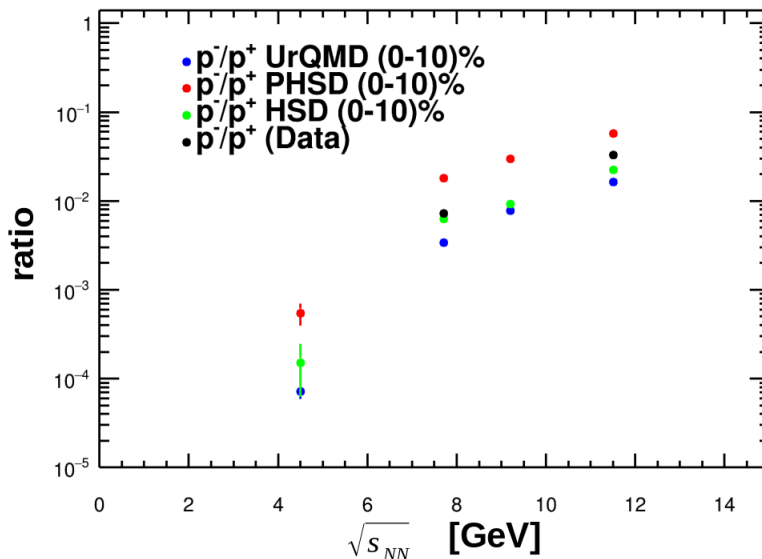


Figure 5.21: The p^-/p^+ ratio as a function of the collision energy for Au+Au. Predictions at a centrality class (0–10)% for the UrQMD (blue), PHSD (red) and HSD (green) models are presented. Data from the STAR collaboration [87] is shown in black.

data at ≥ 9.2 GeV. Thus, the problem might be linked in another direction. There has been some effort put in recent years to unveil the mechanisms responsible for the horn structure of the K^+/π^+ ratio, because no transport model has been able to reproduce the experimental data. Interesting proposals have been made to incorporate a chiral symmetry restoration phase transition (additional to the deconfinement phase transition) to the PHSD event generator [90, 91]. This mechanism, as the authors explain, would be responsible for the rising of the ratio, whereas the drop at higher energies ~ 8 GeV would be because of the appearance of a deconfined partonic medium. This explanation can be in accordance to the results of this work, because we observed that the PHSD model (meaning those including a deconfinement phase transition) are in good agreement with the K^+/π^+ ratio for values ≥ 9.2 . This is not observed when the model is in HSD mode. Even so, we were not able to reproduce the result reported in Ref. [91]. But this is more associated with the fact that the employed PHSD version does not include a chiral symmetry restoration phase, or at least we were not able to find a way to implement it.

5.6 Crossing point

In this section, another interesting effect is studied: the idea is to compare the transverse momentum distributions for a meson (π^+) and a baryon (p^+) in order to observe changes in their behaviour as a function of the collision energy. This spectrum contains information at freeze-out and we should be able to extract the freeze-out parameters in the future.

Figures 5.23-5.25 show both proton and pion distributions at all energies and for the three models. By comparing the protons and pions at the same energy, we can observe that pions are more abundantly produced than protons at low p_T , up to some value at which the situation is reversed: this p_T value is what we call the *crossing point*. Figures 5.23-5.25 show in a vertical line the approximate position at which this transition occurs, from the lowest to

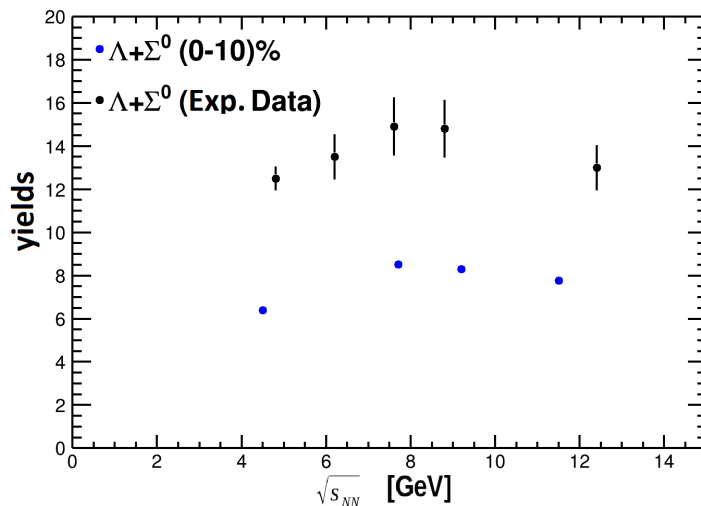


Figure 5.22: Combined particle yields for the Λ and Σ^0 strange baryons. A prediction within the UrQMD for a centrality class 0-10% is shown in blue. Data (black) was taken from Refs. [88, 89].

the highest energy (left side) and from the mid-lowest to the mid-highest energy (right side). The same behaviour is observed for the three models, as the energy of the collision increases, the crossing point also increases its value.

Figure 5.26 shows the evolution of the crossing point as a function of the energy of the collision. It is observed that UrQMD predicts a slightly lower value than the (P)HSD data for all energy values. Both HSD and PHSD present, within error, the same value for the crossing point at all energies except for 11.5 GeV. For each of the models, a simple fit is done with either a linear or a logarithmic function of the form,

$$f_1(x) = a_1 + a_2 \cdot x \quad , \quad f_2(x) = b_1 + b_2 \cdot \log(x) \quad (5.3)$$

with a_1 , a_2 , b_1 and b_2 the fit parameters.

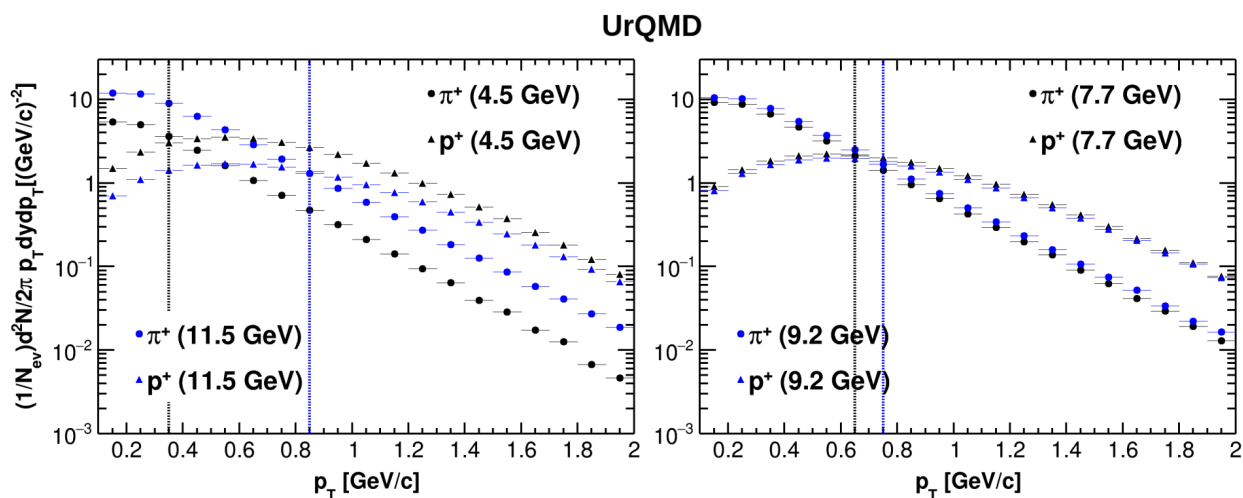


Figure 5.23: Crossing point between protons and positive pions for UrQMD Au+Au collisions. Approximate positions of the crossing point are shown by vertical lines for 4.5 GeV/c (left black), 7.7 GeV/c (right black), 9.2 GeV/c (right blue) and 11.5 GeV/c (left blue).

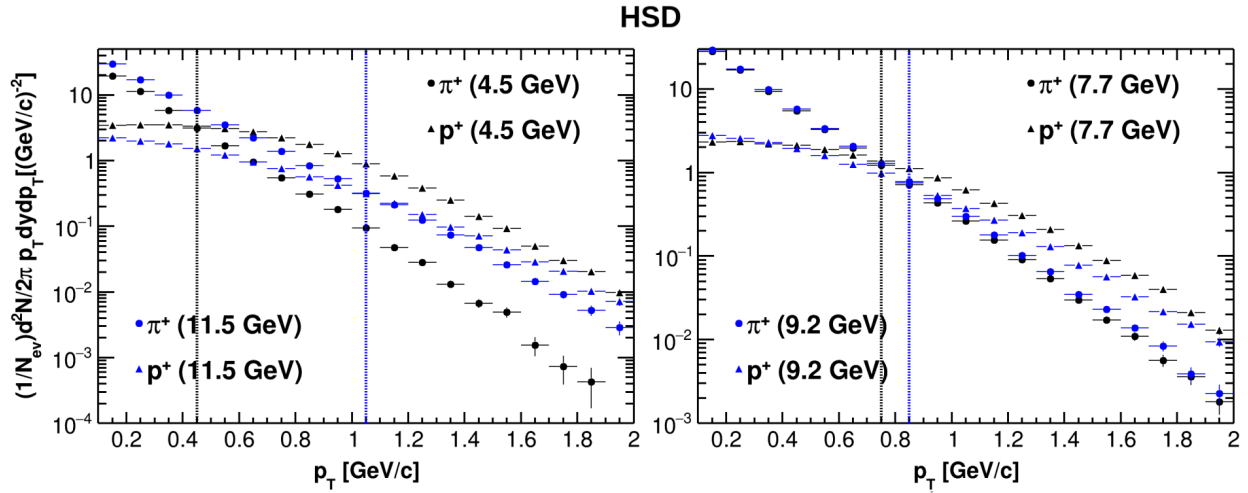


Figure 5.24: Crossing point between protons and positive pions for HSD Au+Au collisions. Approximate positions of the crossing point are shown by vertical lines for 4.5 GeV/c (left black), 7.7 GeV/c (right black), 9.2 GeV/c (right blue) and 11.5 GeV/c (left blue).

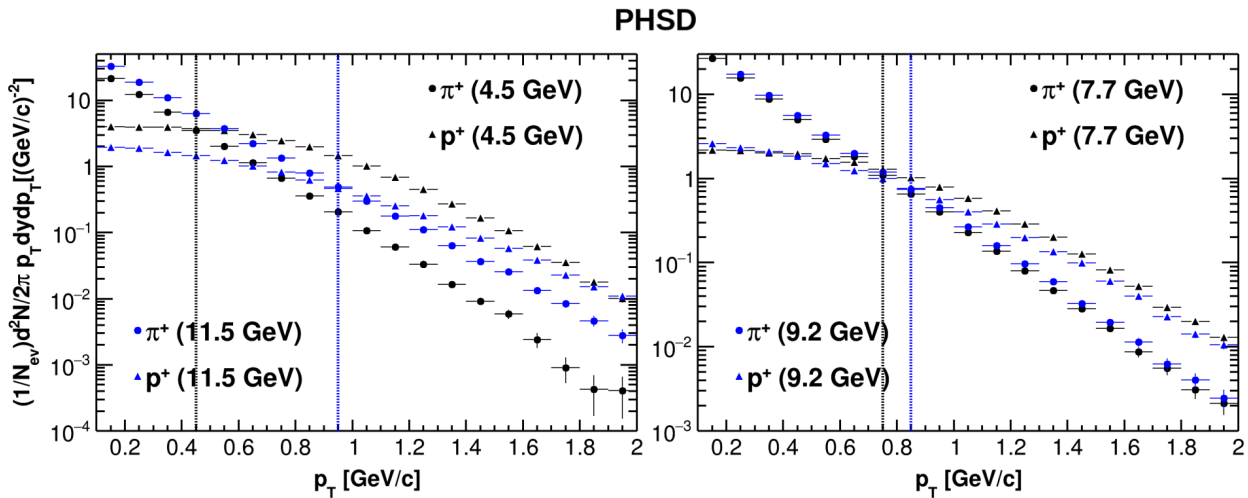


Figure 5.25: Crossing point between protons and positive pions for PHSD Au+Au collisions. Approximate positions of the crossing point are shown by vertical lines for 4.5 GeV/c (left black), 7.7 GeV/c (right black), 9.2 GeV/c (right blue) and 11.5 GeV/c (left blue).

Given the size of the p_T bins, each of the crossing point is taken with an error of 0.1 GeV/c. We observe that each predicted value from the PHSD model is approximately 0.1 GeV/c higher than that of the UrQMD model. Then, both predictions are fitted to the logarithmic function from eq. (5.3), which actually leads to a good fit. For the case of the HSD model, it is fitted to the linear function, because the crossing increases faster than the PHSD case. The fit also looks reasonable well even if the function is very simple. The general result is that both PHSD and UrQMD are transitioning from a mainly mesonic to a mainly baryonic production according to the logarithm of the collision energy. On the other hand, when no partonic phase is introduced, the transition occurs linearly with the collision energy. This is a seemingly strange result, because PHSD does include a deconfinement phase transition, but

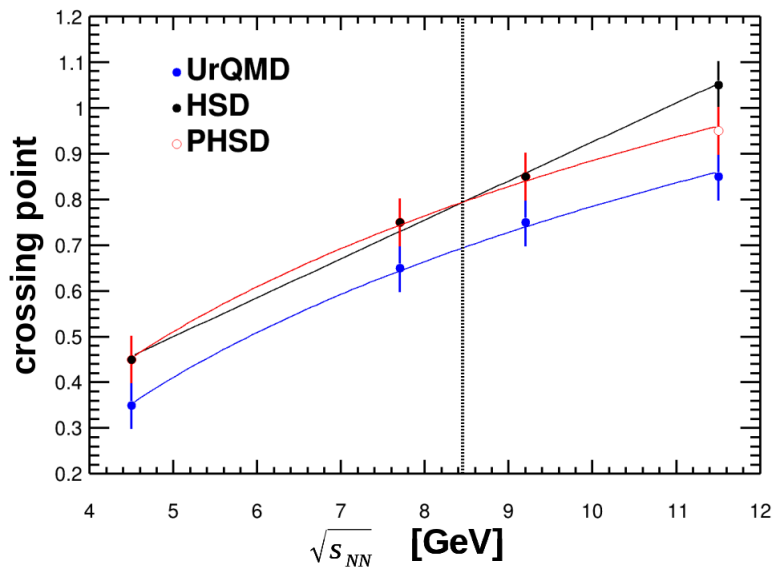


Figure 5.26: Crossing point between protons and pions (positive) for UrQMD Au+Au collisions.

UrQMD does not, and yet both lead to similar conclusions.

Additionally, Figure 5.26 shows in a vertical line the approximate point at which the fit of the HSD model surpasses that of the PHSD model. According to the fits, at low collision energy the transition region in the PHSD model occurs at similar or higher p_T values, but once the energy reaches 8.4 GeV, the transition in the HSD model occurs at higher values. This value could (or not) be accidentally close to the prediction of the statistical models discussed previously, but they occur in different contexts. What this result is telling us is that, depending if the model includes a deconfinement phase transition, a smoother transition from mainly mesonic produced matter to mainly baryonic production should be observed at a given collision energy.

5.7 Future development

There are several different paths to continue and make a more complete version of this work. The immediate one is to do the same analysis done for the MC but for the reconstructed data. That would provide a prediction of what we could expect from the MPD experimental data once the MPD starts operations. The main current issue is that the software is still under development, some important changes have been realized to the MPDroot at the moment of writing. Actually, two updated versions have released since the version employed for this work, and they seem to be focused on the improvement of the particle identification process.

Another interesting approximation is to find a set of better suited parameter values of the event generators, such that they better fit the experimental data. In particular, the same analysis done with the PHSD model with the activation or not of a partonic phase can be realized with the UrQMD model. So, the introduction of the model on the UrQMD+hydro mode with a phase transition could be very interesting for comparison. Also, it would be of interest if we could incorporate chiral symmetry restoration to both models, but that does not seem a trivial issue with the current versions.

In addition, it would be of interest to incorporate an analysis within the statistical models. This could lead to a better understanding of the transverse momentum distributions. The idea has been well established throughout this work, to obtain the freeze-out parameters of the collision, i.e. the temperature and the baryon chemical potential. The very basic approach to follow is to make a fit of the transverse momentum distributions within one of these models (for example, the blast-wave model). With this fit we could directly obtain the temperature and compare to experimental data. We could do the same for the baryon chemical potential and then construct the freeze-out line. The idea is that the statistical model fit of the p_T distributions give a more precise value of the crossing point. This would more or less cover the three types of models of heavy-ion collisions under consideration.

Chapter 6

Conclusions

In this work, we presented an analysis of the transverse momenta distributions for meson and baryons produced in heavy-ion collisions within the MPD-NICA software. The same analysis with three event generators, HSD, PHSD and UrQMD were also studied.

The first part of the analysis was made for the Monte Carlo Au+Au collisions, at MPD-NICA energies: $\sqrt{s_{NN}} = 4.5, 7.7, 9.2$ and 11.5 GeV. Different particle ratios were studied in the three models. Particle-to-antiparticle ratios show a good agreement with experimental data except for the ratio K^-/K^+ in the UrQMD case. The K^-/π^- ratio follows the experimental trend, but quantitative differences are observed, particularly at high collision energy in the UrQMD model and at low collision energy in the (P)HSD model. Meanwhile, the K^+/π^+ ratio is not well reproduced for any model. It is very likely that the UrQMD model fails because it does not predict enough strange baryons at mid-to-high collision energy, which are strongly correlated to the K^+ production. This situation could be corrected to some extent by the introduction of a partonic phase, just as the PHSD model shows, but with the current results it seems insufficient to explain the horn structure in the ratio.

The crossing point between pions and protons was studied as a function as the collision energy. The UrQMD and PHSD models predict a similar logarithmic scaling (in the form $f(E) = a_1 + a_2 \cdot \ln E$) of the crossing point with the energy, whereas the HSD produces a linear behaviour. The disagreement between PHSD and HSD shows that at energies larger than 8.4 GeV the predicted crossing increases slowly if a deconfinement transition is introduced. This is actually in agreement with the findings of Ref. [91]. Evidence suggest that the rising of the K^+/π^+ ratio might not be explained by the existence of the partonic phase alone, as early suggestions anticipated, but could also be related to a chiral symmetry restoration phase transition. In fact, the decreasing at higher energy values (>8.2 GeV) might be due to the existence of the deconfinement or crossover transition. So the horn structure could show an interplay between a chiral symmetry restoration and deconfinement transitions.

The ratio p/\bar{p} and yield of the Λ^0 and Σ^0 hyperons as a function of collision energy was also computed and compared with experimental data. The findings of this work indicate a considerable difference with respect to the experimental data. The disagreement suggest that some improvements in the models are needed.

The second part of the analysis was the reconstruction of the Bi+Bi collision at 9.2 GeV within the MPD software. The contamination and identification's efficiency was studied as a function of the total momentum. Overall, in the $0.1 \text{ GeV}/c < p < 2 \text{ GeV}/c$ range, the protons' efficiency stays higher than 95% (except for the first two bins for the UrQMD Au+Au

set). For the case of pions, the efficiency is observed $> 90\%$ in all sets. The kaons are the worst reconstructed hadrons, but their efficiency stays higher than 80% overall.

Reconstructed transverse momentum distributions were compared to the MC ones. Generally speaking, they reproduce the shape at medium-to-high p_T , but they all fail greatly at low p_T . The issue is likely related to the detector's performance: most of the low momentum particles are not detected by the TPC or are misidentified (protons and kaons) with pions in most of the cases. We expect that if the appropriate corrections by efficiency, acceptance, etc. were applied, they would fit the MC data better. UrQMD, PHSD and HSD models produced similar distributions in the Au+Au case, with the difference that (P)HSD distributions look rather like UrQMD distributions moved to lower p_T . MC distributions for the Bi+Bi case are both qualitatively and quantitatively similar, the major difference is observed quantitatively for the K^+ case. The reconstruction and corresponding efficiency also have similarities, except for the pions, where the reconstructed distribution surpasses that of the MC, whose main source of contamination is likely due to secondary pions.

Looking ahead, NICA-MPD's commissioning marks a promising future for exploring the QCD phase diagram. This study represents an initial step in a broader project, a modest contribution to the MPD's joint effort.

Bibliography

- [1] E. O. Lawrence and M. S. Livingston, The Production of High Speed Light Ions Without the Use of High Voltages. *Phys. Rev.* **40**, (1932) 19-37.
- [2] W. Florkowski, *Phenomenology of Ultra-Relativistic Heavy-Ion Collisions*. World Scientific, 1st ed., 2010.
- [3] R. S. Bhalerao, Relativistic heavy-ion collisions. *Proc. AEPSHEP 2012*, (2014) 219-239.
- [4] J.P. Blaizot, Ultrarelativistic heavy ion collisions: Theoretical overview. *J. Phys.: Conf. Ser.* **50** (2006) 1.
- [5] Virtual Journal on QCD Matter. <http://qgp.phy.duke.edu/>
- [6] S. Chekanov *et al.* [ZEUS Collaboration], ZEUS next-to-leading-order QCD analysis of data on deep inelastic scattering. *Phys. Rev. D* **67** (2003) 012007.
- [7] T. Lappi and L. McLeran, Some features of the glasma. *Nucl. Phys. A* **772** (2006) 200-212.
- [8] M. Gazdzicki and M. I. Gorenstein, On the early stage of nucleus-nucleus collisions. *Acta Phys. Polon. B* **30** (1999) 2705.
- [9] S. Hamieh, J. Letessier and J. Rafelski, Quark gluon plasma fireball. *Phys. Rev. C* **62** (2000) 064901.
- [10] G. Jaeger, The Ehrenfest Classification of Phase Transitions: Introduction and Evolution. *Arch Hist Exact Sc.* **53** (1998) 51-81.
- [11] M. A. Stephanov, QCD phase diagram: An Overview. *PoS LAT2006* (2006) 024.
- [12] K. Fukushima and T. Hatsuda, The phase diagram of dense QCD. *Rept. Prog. Phys.* **74** (2011) 014001.
- [13] J. M. Pawłowski, The QCD phase diagram: Results and challenges. *AIP Conf. Proc.* **1343** (2011) 75-80.
- [14] M. Gazdzicki, Phase diagram of strongly interacting matter: the last 20 years at the CERN SPS. *Eur. Phys. J. Spec. Top.* **229** (2020) 3507–3516.
- [15] O. Philipsen, Status of the QCD Phase Diagram from Lattice Calculations. *Acta Phys. Polon. Supp.* **5** (2012) 825-835.

- [16] P. de Forcrand, Simulating QCD at finite density. *PoS LAT2009* (2009) 010.
- [17] F. R. Brown *et al.*, On the existence of a phase transition for QCD with three light quarks. *Phys. Rev. Lett.* **65** (1990) 2491-2494.
- [18] New State of Matter created at CERN. <https://home.cern/news/press-release/cern/new-state-matter-created-cern>
- [19] M. Gazdzicki, M. Gorenstein and P. Seyboth, Onset of deconfinement in nucleus-nucleus collisions: Review for pedestrians and experts. *Acta Phys. Polon. B* **42** (2011) 307-351.
- [20] A. Bazavov *et al.* [HotQCD Collaboration], Chiral crossover in QCD at zero and non-zero chemical potentials. *Phys. Lett. B* **795** (2019) 15-21.
- [21] NUPECC. https://www.esf.org/fileadmin/user_upload/esf/Nupecc-LRP2017.pdf
- [22] T. Tanimoto, W. Bentz and I. C. Cloët, Massive Neutron Stars with a Color Superconducting Quark Matter Core. *Phys. Rev. C* **101** (2020) 055204.
- [23] L. McLerran and R. D. Pisarski, Phases of cold, dense quarks at large $N(c)$. *Nucl. Phys. A* **796** (2007) 83-100.
- [24] H. T. Ding *et al.* [HotQCD Collaboration], Chiral phase transition temperature in (2+1) Flavor QCD. *Phys. Rev. Lett.* **123** (2019) 062002.
- [25] S. Sharma [Bielefeld-BNL-CCNU], The QCD Equation of state and critical end-point estimates at $\mathcal{O}(\mu_B^6)$. *Nucl. Phys. A* **967** (2017) 728-731.
- [26] J. Cleymans and K. Redlich, Unified Description of Freeze-Out Parameters in Relativistic Heavy Ion Collisions. *Phys. Rev. Lett.* **81** (1998) 5284-5286.
- [27] P. Braun-Munzinger, J. Stachel and C. Wetterich, Chemical freezeout and the QCD phase transition temperature. *Phys. Lett. B* **596** (2004) 61-69.
- [28] L. Kumar, Review of recent results from the RHIC Beam Energy Scan. *Mod. Phys. Lett. A* **28** (2013) 1330033.
- [29] J. Cleymans, H. Oeschler, K. Redlich and S. Wheaton, Comparison of chemical freeze-out criteria in heavy-ion collisions. *Phys. Rev. C* **73** (2006) 034905.
- [30] J. Cleymans, H. Oeschler and K. Redlich, Influence of impact parameter on thermal description of relativistic heavy ion collisions at (1-2)A GeV. *Phys. Rev. C* **59** (1999) 1663-1673.
- [31] R. Stock, Relativistic nucleus-nucleus collisions: from the BEVALAC to RHIC. *J. Phys.* **G30** (2004) S633-S648.
- [32] J. Cleymans, H. Oeschler, K. Redlich and S. Wheaton, Transition from Baryonic to Mesonic Freeze-Out. *Phys. Lett. B* **615** (2005) 50-54.
- [33] Joint Institute for Nuclear Research. <http://www.jinr.ru/>

- [34] V. D. Kekelidze *et al.*, Three Stages of The NICA Accelerator Complex Nuclotron-based Ion Collider fAcility. *Proc. LHCP2015* (2016) 565-569.
- [35] Nuclotron-based Ion Collider fAcility. <https://nica.jinr.ru/>
- [36] A. Butenko *et al.*, The NICA Complex Injection Facility. *RuPAC2021* (2021) 7-11.
- [37] A. V. Butenko *et al.*, Commissioning of New Light Ion RFQ Linac and First Nuclotron Run with New Injector. *RuPAC2016* (2016) 153-155.
- [38] H. Höltermann *et al.*, Light Ion Linear Accelerator up to 7 AMeV for NICA. *Proc. RuPAC2018* (2018) 68-71.
- [39] V. V. Kobets *et al.*, Heavy ion injector for NICA/MPD project. *Proc. RuPAC2008* (2008) 110-112.
- [40] A. V. Butenko *et al.*, Commissioning of the New Heavy Ion Linac at the NICA Project. *RuPAC2016* (2016) 156-159.
- [41] A.V. Butenko *et al.*, Injection complex development for the NICA project. *LINAC2018* (2018) 663-665.
- [42] A.V. Butenko, N. Agapov, *et al.*, Design of the Nuclotron booster in the NICA project *Proc. RuPAC2010* (2010) 68-70.
- [43] R. Lednicky, Projects of Nuclotron modernization and Nuclotron-based ion collider facility (NICA) at JINR. *Phys. Atom. Nuclei* **71** (2008) 1514-1517.
- [44] E. Syresin *et al.*, NUCLOTRON Development for NICA Acceleration Complex. *IPAC2019* (2019) 3396-3398.
- [45] O. Kozlov *et al.*, Design of the NICA collider rings. *Proc. IPAC2011* (2011) 1807-1809.
- [46] M. Kapishin, Studies of baryonic matter at the BM@N experiment (JINR). *Nuc. Phys. A* **982** (2019) 967-970.
- [47] BM@N conceptual design report. https://nica.jinr.ru/files/BM@N/BMN_CDR.pdf
- [48] V. M. Abazov *et al.* [SPD proto], Conceptual design of the Spin Physics Detector. arXiv:2102.00442 (2021).
- [49] SPD technical design report. http://spd.jinr.ru/wp-content/uploads/2023/03/TechnicalDesignReport_SPD2023.pdf
- [50] M. Rodríguez Cahuantzi and for the MEXnICA group, MEXnICA, Mexican group in the MPD-NICA experiment at JINR. *J. Phys.: Conf. Ser.* **912** (2017) 1-7.
- [51] MPD technical design report. <http://mpd.jinr.ru/doc/mpd-tdr/>
- [52] V. Abgaryan *et al.* [MPD Collaboration], Status and initial physics performance studies of the MPD experiment at NICA. *Eur. Phys. J. A* **58** (2022) 140.

- [53] R. J. Glauber, *Lectures in Theoretical Physics*, New York: Interscience, ed. WE Brittin, 1959.
- [54] M. Miller, K. Reygers, S. Sanders and P. Steinberg, Glauber Modeling in High Energy Nuclear Collisions. *Annu. Rev. Nucl. Part. Sci.* **57** (2007) 205-243.
- [55] E. L. Bratkovskaya, W. Cassing, P. Moreau, and T. Song, Review of the theoretical heavy-ion physics. *KnE Energy & Physics* (2018) 234-246.
- [56] T. Reichert *et al.*, Comparison of heavy ion transport simulations: Ag+Ag collisions at $Elab = 1.58$ AGeV. *J. Phys. G: Nucl. Part. Phys.* **49** (2022) 055108.
- [57] M. Azarkin and M. Kirakosyan, Performance of Monte Carlo event generators of pp collisions at NICA energies. *J. of Exp. and Theor. Phys.* **137** (2024) 630-647.
- [58] S. A. Bass *et al.*, Microscopic Models for Ultrarelativistic Heavy Ion Collisions. *Prog. Part. Nucl. Phys.* **41** (1998) 255-369.
- [59] M. Bleicher *et al.*, Relativistic hadron-hadron collisions in the ultra-relativistic quantum molecular dynamics model. *J. Phys.* **G25** (1999) 1859-1896.
- [60] I. Zahed and G.E. Brown, The Skyrme model. *Physics Reports* **142** (1986) 1-102.
- [61] H. Petersen, J. Steinheimer, G. Burau, M. Bleicher and H. Stöcker, Fully integrated transport approach to heavy ion reactions with an intermediate hydrodynamic stage. *Phys. Rev. C* **78** (2008) 044901.
- [62] UrQMD user manual. <https://itp.uni-frankfurt.de/~bleicher/userguide.pdf>
- [63] W. Cassing and E. L. Bratkovskaya, Parton transport and hadronization from the dynamical quasiparticle point of view. *Phys. Rev. C* **78** (2008) 034919.
- [64] W. Cassing and E. L. Bratkovskaya, Parton-Hadron-String Dynamics: an off-shell transport approach for relativistic energies. *Nucl. Phys. A* **831** (2009) 215-242.
- [65] PHSD user manual. Upon request at <http://theory.gsi.de/~ebratkov/phsd-project/PHSD/index4.html>
- [66] R. Brun *et al.*, “GEANT: Detector Description and Simulation Tool”. ebook: 10.17181/CERN.MUHF.DMJ1 (1993).
- [67] Geant4. <http://geant4.cern.ch>
- [68] MPDroot. <http://mpdroot.jinr.ru/>
- [69] P. Parfenov, D. Idrisov, V. B. Luong and A. Taranenko, Relating Charged Particle Multiplicity to Impact Parameter in Heavy-Ion Collisions at NICA Energies. *Particles* **4** (2021) 275-287.
- [70] V. Klochkov and I. Selyuzhenkov, Centrality Determination in Heavy-ion Collisions with CBM. *Acta Phys. Polon. Supp.* **10** (2017) 919-920.

- [71] E. Zherebtsova, V. Klochkov, I. Selyuzhenkov, A. Taranenko and E. Kashirin, Procedure for event characterization in Pb-Pb collisions at 40 AGeV in the NA49 experiment at the CERN SPS. *EPJ Web Conf.* **182** (2018) 02132.
- [72] W. R. Leo, *Techniques for Nuclear and Particle Physics experiments. A how-to approach.* Springer-Verlag, 2nd ed., 1993.
- [73] W. Yu [ALICE collaboration], Particle identification of the ALICE TPC via dE/dx. *Nucl. Inst. and Met. in Phys. Res. A* **706** (2013) 55–58.
- [74] M. Allison and H. Cobb, Relativistic Charged Particle Identification by Energy Loss. *Annu. Rev. Nucl. Part. Sci.* **30** (1980) 253-298.
- [75] P. Senger and H. Ströbele, Hadronic particle production in nucleus–nucleus collisions. *J. Phys.* **G25** (1999) R59-R131.
- [76] P. Senger, Particle production in heavy-ion collisions. *Prog. in Part. and Nucl. Phys.* **53** (2004) 1–23.
- [77] R. Brockmann *et al.*, Pion and Proton “Temperatures” in Relativistic Heavy-Ion Reactions. *Phys. Rev. Lett.* **53** (1984) 2012-2015.
- [78] A. Wagner *et al.*, Emission Pattern of High-Energy Pions: A New Probe for the Early Phase of Heavy-Ion Collisions. *Phys. Rev. Lett.* **85** (2000) 18-21.
- [79] E. L. Bratkovskaya, W. Cassing and U. Mosel, Analysis of kaon production at SIS energies. *Nucl. Phys. A* **622** (1997) 593-604.
- [80] C. Fuchs *et al.*, Origin of subthreshold K^+ production in heavy ion collisions. *Phys. Rev. C* **56** (1997) R606.
- [81] W. Cassing, E. L. Bratkovskaya, U. Mosel, S. Teis, A. Sibirtsev, Kaon versus antikaon production at SIS energies. *Nucl. Phys. A* **314** (1997) 415-432.
- [82] C. B. Doover and G. E. Walker, The interaction of kaons with nucleons and nuclei. *Physics Reports* **89** (1982) 1-177.
- [83] V. Steinberg *et al.*, Strangeness production via resonances in heavy-ion collisions at energies available at the GSI Schwerionensynchrotron. *Phys. Rev. C* **99** (2019) 064908.
- [84] A. Ayala, W. Bietenholz, E. Cuautle, R. García Formentí and R. Guzmán, Searching for the baryon-to-meson transition region with the MPD at NICA. *Phys. At. Nucl.* **86** (2023) 901-907.
- [85] J. L. Klay *et al.* [E895 Collaboration], Charged pion production in 2A to 8A GeV central Au+Au Collisions. *Phys. Rev. C* **68** (2003) 054905.
- [86] B. I. Abelev *et al.* [STAR Collaboration], Identified particle production, azimuthal anisotropy, and interferometry measurements in Au+Au collisions at $\sqrt{s_{NN}}=9.2$ GeV. *Phys. Rev. C* **81** (2010) 024911.

-
- [87] L. Adamczyk *et al.* [STAR Collaboration], Bulk Properties of the Medium Produced in Relativistic Heavy-Ion Collisions from the Beam Energy Scan Program. *Phys. Rev. C* **96** (2017) 044904.
- [88] S. Albergo *et al.*, Λ Spectra in 11.6A GeV/ c Au-Au Collisions. *Phys. Rev. Lett.* **88** (2002) 062301.
- [89] C. Alt *et al.* [NA49 Collaboration], Energy dependence of Λ and ξ production in central Pb+Pb collisions at 20A, 30A, 40A, 80A, and 158A GeV measured at the CERN Super Proton Synchrotron. *Phys. Rev. C* **78** (2008) 034918.
- [90] P. Moreau, W. Cassing, A. Palmese, E. L. Bratkovskaya, Hadron Production within PHSD. *Acta Phys. Polon. Supp.* **9** (2016) 279.
- [91] E. L. Bratkovskaya *et al.*, Chiral symmetry restoration versus deconfinement in heavy-ion collisions at high baryon density. *J. Phys.: Conf. Ser.* **878** (2017) 012018.
- [92] B. I. Abelev *et al.* [STAR Collaboration], Systematic measurements of identified particle spectra in pp, d+Au, and Au+Au collisions at the STAR detector. *Phys. Rev. C* **79** (2009) 034909.